Funded by the European Union

Horizon Europe programme, grant agreement No. 101096068

RETROFIT SOLUTIONS TO ACHIEVE 55% GHG REDUCTION BY 2030

Report on hydrodynamic optimization at realistic operational conditions

WP 2 – Hydrodynamic design optimization	
Task 2.1 – Hydrodynamic optimization at realistic operational conditions	
D2.1 – Report on hydrodynamic optimization at realistic operational conditions	
Partners involved: SFD, NTUA, CNR, FSYS	
Authors: D. Ntouras, K. Kostalas, R. D’Souza, V. Zagkas, G. Papadakis, N. Themelis, A. Kanelopoulou, G. Zaraphonitis, D. Anevlavi, S. Zafeiris, K. Belibassakis, A. Serani, A. Del Buono, M. Diez, R. Broglia, H. Renzsch, A. Arapakopoulos	

Project details

Project Title	RETROFIT SOLUTIONS TO ACHIEVE 55% GHG REDUCTION BY 2030
Project Type	Innovation Action
Project Acronym	RETROFIT55
Grant Agreement No.	101096068
Duration	36M
Project Start Date	01/01/2023

Deliverable information

Status (F: final; D: draft; RD: revised draft)	D 24/02/2025
Planned delivery date	31/12/2024
Actual delivery date	01/04/2025
Dissemination level: PU – Public, fully open, e.g. web (Deliverables flagged as public will be automatically published in CORDIS project's page) SEN – Sensitive, limited under the conditions of the Grant Agreement Classified R-UE/EU-R – EU RESTRICTED under the Commission Decision No2015/444 Classified C-UE/EU-C – EU CONFIDENTIAL under the Commission Decision No2015/444 Classified S-UE/EU-S – EU SECRET under the Commission Decision No2015/444	PU
Type: Report, Website, Other, Ethics	Report

Document history

Version	Date	Created/Amended by	Changes
01	24/02/2025	Dimitris Ntouras, Reuben D'Souza, Vassilios Zagkas, (SFD)	First Draft
02	01/04/2025	Dimitris Ntouras, Reuben D'Souza, Vassilios Zagkas, (SFD)	Final version

Quality check review

Reviewer	Main changes / Actions
Cecilia Leotardi (CNR)	Technical and editorial review.
Cecilia Leotardi and Alessandro Iafrati(CNR)	Final review of contents and submission to EC.

Table of Contents

List of Figures

List of Tables

List of acronyms

AoA	Angle of Attack
CAD	Computer Aided Design
CFD	Computational Fluid Dynamics
DoE	Design of Experiments
DSS	Decision Support System
ESD	Energy-Saving Devices
FFD	Free Form Deformation
GHG	GreenHouse Gas
ITTC	International Towing Tank Committee
LPP	Length between Perpendiculars
LOA	Length Over All
LCB	Longitudinal Center of Buoyancy
MCR	Maximum Continuous Rating
NCR	Nominal Continuous Rating
RANSE	Reynolds Average Navier Stokes Equations
SST model	Shear Stress Transport model
VoF	Volume of Fluid

Executive Summary

This report is part of the EU-funded **RETROFIT55**[1] project and summarizes the work conducted in Task T2.1 on hydrodynamic optimization at realistic operational conditions. **RETROFIT55** project will deliver a Decision Support System (DSS) that will allow combination of various retrofitting solutions in order to achieve a GHG emission reduction of 35% compared to the original design. Specifically, the retrofit solutions developed within the project will combine mature technologies (ship electrification, hydrodynamic design optimization and operational optimization) with two new technologies (wind-assisted ship propulsion and innovative air lubrication system).

The objective of this report is to explore retrofitting solutions to improve the hydrodynamic design of existing vessels. To this end, two ships have been selected, a bulk carrier vessel and a Ro-Ro vessel as test case studies for the optimization procedure. The different types of ships ensure that results will be applicable to a wide range of ship types. Emphasis is placed on the actual operating speed and conditions of the vessels.

Different tools of varying fidelity have been utilized to calculate the hydrodynamic performance of the existing vessels and assess the effect of the proposed solutions. They range from high-fidelity CFD tools to potential flow solvers. Both in-house and commercial software were used for the studies The multi-fidelity framework allows for fast exploration of the potential solutions while at the same time ensures the detailed assessment of the final design.

The solutions considered for the hydrodynamic optimization of the two vessels and reported in detail in the present document are (a) bow retrofitting, (b) propeller optimization, (c) trim optimization and (d) wake optimization through Energy Saving Devices (ESDs). The results of these studies revealed that bow retrofitting can provide gains up to 2%, minor gains were achieved from propeller retrofitting, the trim sensitivity study showed large deviations in resistance and lastly ESD retrofitting can improve powering efficiency up to 2%.

[1] https://cordis.europa.eu/project/id/101096068

1 Introduction

Maritime transportation is responsible for 3% of global GHG emissions[2]. Several initiatives have been taken at a European and global level to deliver transition to net zero emissions. The revised 2023 IMO strategy sets a goal for net zero emissions from ships by 2050, with intermediate checkpoints, while EU's package "Fit for 55" aims to reduce emissions by at least 55% by 2030, compared to 1990 levels[3]. RETROFIT55 is an EU funded project that aims to create a DSS, featuring a catalogue of retrofitting solutions that are up-to-date and ready to be deployed. The DSS will allow combining retrofitting solutions to achieve a GHG emissions reduction of 35% compared to the original design. The technologies addressed in the project include mature technologies such as hydrodynamic optimization, operational optimization and ship electrification and two novel technologies - Wind Assisted Ship Propulsion (WASP) and Air Lubrication System (ALS).

Hydrodynamic design optimization examines various solutions to improve the performance of a given ship in its prevailing profile. Operators examine solutions such as propeller replacement, different bulbous bows, pre- and post-swirl Energy Saving Devices (ESD). Each hydrodynamic solution may bring gains of up to a few percent of resistance reduction when optimized for the prevailing trim-draft and speed combinations. The percentage of reduction can be even greater in cases where the operation profile differs from the designed conditions.

A significant reduction of GHG could only be attained by an efficient combination of retrofitting solutions, since this target cannot be achieved by a single retrofit solution. Any single percent reduction is necessary and counts towards the total reduction. Hydrodynamic design optimization contribution is typically of a single percent, which is small but crucial for the overall objectives.

[2] https://climate.ec.europa.eu/eu-action/transport/reducing-emissions-shipping-sector_en

[3] https://commission.europa.eu/strategy-and-policy/priorities-2019-2024/european-green-deal/delivering-european-green-deal_en

2 Scope, objective, and structure of the report

The purpose of this deliverable is to provide a comprehensive account for the solutions that have been explored to improve the hydrodynamic design of vessels under the scope of RETROFIT55 project.

The present report assesses the performance of hydrodynamic solutions for two case study vessels to improve their performance. A bulk carrier and Ro-Ro vessel are selected, which represent two categories with distinct characteristics: low-speed cargo ships with high block coefficient and slender, faster vessels. The scope of the report is to provide an insight into the hydrodynamic optimization procedure of existing vessels, the various tools that have been employed and the methodologies adopted. It needs to be noticed that the studies are targeted at the operational profile of each vessel.

The report is a result of collaborative work between four partners of the RETROFIT55's consortium. Four retrofitting options have been examined for the bulk carrier vessel and one for the Ro-Ro vessel. The report details the methodologies that have been followed for each optimization case, while any simplification and assumptions are presented and explained. Furthermore, the computational tools used are described and finally results and the working principles of each retrofitting solution have been discussed.

Finally, the results of this study will be exported to WP1 which concerns the development of the DSS. The effect of each retrofitting technology and the possible gains that will be used by the DSS can be found in the present deliverable.

The report is structured to provide a clear and detailed account of the consortium's efforts to provide retrofitting solutions to improve the ship's hydrodynamic design and their alignment with the overall objectives of the RETROFIT55 project as outlined in the Grant Agreement.

Summary: Report executive summary

Introduction: A brief overview of the RETROFIT55 project and the goals of hydrodynamic optimization.

Scope, objective, and structure of the report: An explanation on how hydrodynamic optimization aligns with the RETROFIT55 objectives, the framework, and the goals of the studies presented here., along with a description of the overall structure of the present report.

Geometry Description: This section presents the principal characteristics of each case study vessel along with a description of the operational data used as input in the hydrodynamic optimization process. Furthermore, it provides a comparison of the generated 3D-CAD models with actual hydrostatic data.

Hydrodynamic Optimization of bulk carrier vessel: This section summarizes the work that has been carried out by the participants to improve the hydrodynamic performance of the bulk carrier vessel. Each subsection describes a different retrofitting technology. Methods, tools and results are presented and thoroughly explained. The following studies are included in the present report.

Propeller Optimization

Bulbous Bow Optimization

Trim Optimization

ESD retrofitting

Hydrodynamic Optimization of RoRo carrier vessel: The bow optimization carried out for the Ro-Ro vessel is presented. Similarly to the previous section, the approach that has been followed along with all the computational tools used are described in detail.

3 Geometry Description

3.1 Bulk Carrier vessel

SFD created the 3D model of the bulk carrier vessel M/V Kastor.Table 1, Table 2 and Table 3 present the main particulars of the vessel, engine and propeller.

Table 1: Vessel's main particulars

Ship Name:	M/V Kastor
Ship Type:	BULK CARRIER
Year of Build:	2020
LPP (m):	225.5
Breadth (MLD) [m]:	32.20
Depth (MLD) [m]:	20.05
Scantling Draft [m]:	14.45
Extreme Draft Displ. [t]:	94796.2
Block Coefficient (CB):	0.8772
Lightweight [t]:	13800.1
IMO No.	9843405
Scantling Draft [m]:	14.45
Extreme Draft Displ. [t]:	94796.2

Table 2: Bulk Carriers Engine main particulars

MCR	9930 kW	90.4 RPM
NCR	7110 kW	80.9 RPM

Table 3: Propeller's main particulars

Type:	FPP
Diameter [m]:	6.95
Number of Blades:	5
P/D at 0.7R:	0.7719
Mean Pitch [mm]:	5258.39
Expanded Area Ratio	0.52
Chord Length at 0.6R [mm]	2085.0

Figure 1 shows a comparison of the 3D model created and two views from the General Arrangement drawing.

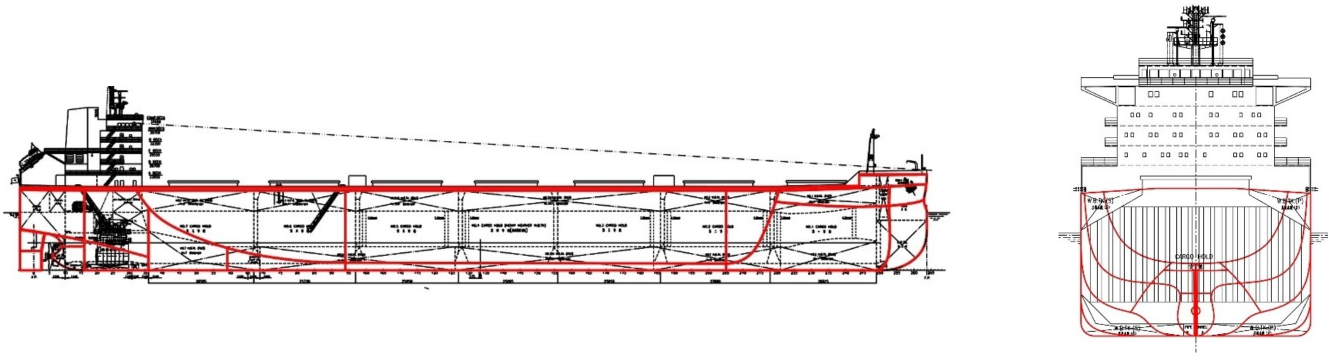

Figure 1: Comparison of 3D model with drawings for M/V Kastor. At the left, comparison at the side view, comparison at the midship section.

The 3D model follows accurately the actual geometry. This can be also validated by performing a hydrostatic comparison. Table 4 compares the displacement and the lateral center of buoyancy as computed from the 3D model with the data from ship’s trim and stability booklet. In all conditions, errors are below 1%.

Table 4: Hydrostatic data comparison between the modelled *M/V Kastor* and as-built hull

	3D-CAD hull particulars		**Ship particulars (from stability booklet)**		**Comparison**	
Draught [m]	Dsplt. [t]	LCB [m]	Dsplt. [t]	LCB [m]	Dsplt. [%]	LCB [%]
3	17,326	120.058	17,464	120.148	-0.79%	-0.07%
5	29,807	119.414	29,962	119.531	-0.52%	-0.10%
7	42,667	118.679	42,870	118.795	-0.47%	-0.10%
9	56,065	117.473	56,258	117.711	-0.34%	-0.20%
10	62,941	116.849	63,162	117.021	-0.35%	-0.15%
12	77,011	115.368	77,289	115.589	-0.36%	-0.19%
14.45	94,516	113.967	94,796	114.225	-0.30%	-0.23%

3.2 RoRO vessel

3.2.1 Ship Characteristics

The RoRo cargo ship EUROCARGO ROMA serves as the baseline geometry for this study. It is a Hyundai-class vessel with a length between perpendiculars (L_{pp}) of 190 meters and an overall length (LOA) of 200 meters. The ship's breadth measures 26.5 meters, and it features a scantling draft of 7.5 meters, with an extreme displacement of 23,071.3 tons.

The ship's geometric configuration plays a significant role in determining hydrodynamic resistance. The longitudinal center of gravity (XCG) is positioned at 81.51 meters from the aft perpendicular, while the vertical center of gravity (ZCG) is 12.92 meters from the keel. These parameters are critical in ensuring that modifications made to the bow do not adversely impact the vessel's trim and stability.

The Grimaldi Group provided these fundamental geometrical specifications, along with detailed operational data, ensuring that the optimization remained grounded in real-world vessel conditions. SFD generated and provided CAD (.stp files), see Figure 2.

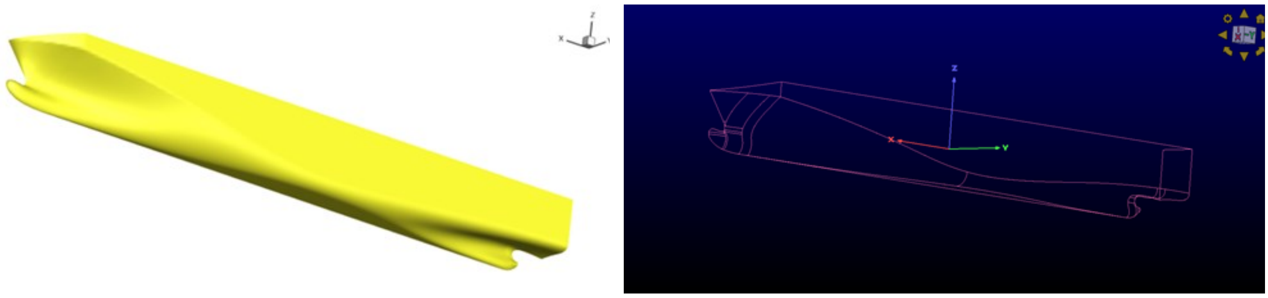

Figure 2: Geometry, CAD representation.

__Vessel's key parameters:__

- Length Between Perpendiculars (L_{pp}): 190 m
- Length Overall (LOA): 200 m
- Beam (B): 26.5 m
- Scantling Draft: 7.5 m
- Displacement: 23,071.3 tonnes

3.2.2 Operational Data

To ensure realistic optimization constraints, the study incorporated one week of real operational data from the vessel, see Figure 3. The nominal cruise speed was recorded at 18.2 knots, with observed variations ranging between 17.26 and 18.97 knots. Data also showed port operations, as revealed by the histogram analysis and kernel density estimation presented in Figure 4. This data provided insights into the ship's typical performance, allowing for accurate modelling of hydrodynamic resistance and fuel consumption.

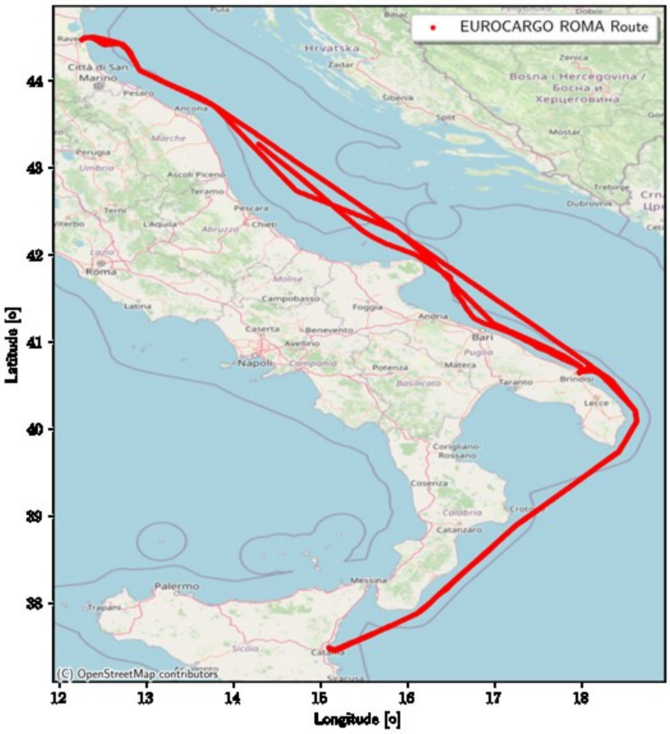

Figure 3: Route of the EUROCARGO ROMA during the observed period (one week).

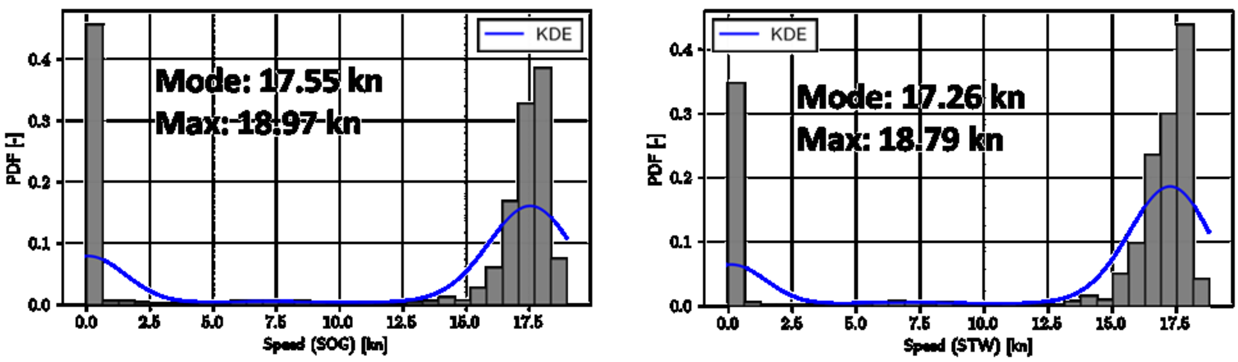

Figure 4: Probability densities of speed over ground (SOG) and speed through water (STW).

Operational data also included variations in draft and displacement across different loading conditions. These factors were integrated into the modelling process to assess the effectiveness of the optimized bow across multiple operating scenarios. By considering real-world operational variations, this study ensures that the proposed retrofitting modifications are practical and applicable under standard voyage conditions.

Operational data summary

- Nominal cruise speed: 18.2 knots
- Speed distribution: Mode at 17.26 knots, max at 18.79 knots
- Fuel consumption correlation with speed distribution (Figure 5).

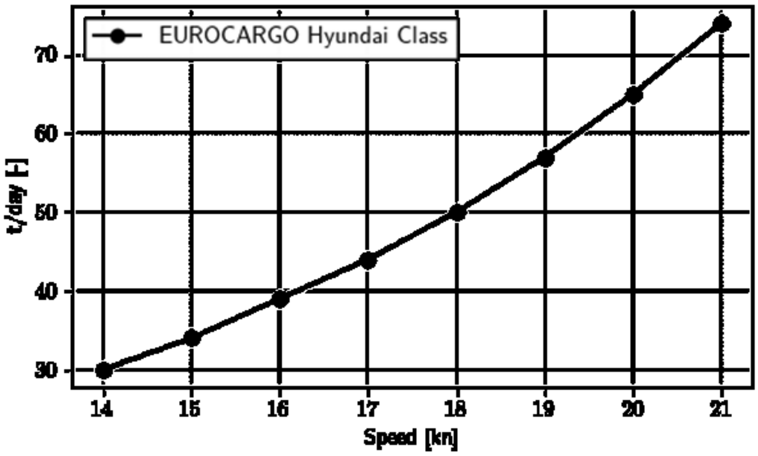

Figure 5: Fuel consumption vs. speed.

4 Hydrodynamic design optimization of *bulk carrier* vessel

4.1 Propeller Optimization

The open water performance of a propeller can be evaluated using various numerical tools including lifting-surface theory models and Reynolds-averaged Navier-Stokes equations (RANSE) solvers. Here, two numerical tools will be used. One for low-fidelity prediction and one for higher-fidelity evaluation of results. The first is a code applying the Vortex-Lattice Method (VLM), whereas the second is MaPFlow, a CFD solver.

The Vortex-Lattice Model

The Vortex-lattice model is based on the assumption that a hydrodynamic slender body can be accurately modelled as a surface carrying a distribution of vorticity. This is achieved under the assumption of an incompressible, irrotational and inviscid fluid.

Following these assumptions, a discretization is defined. The surface is discretized as a mesh of rectangular vortex-rings, whose edges are called vortex filaments. We also define a set of control points positioned inside the cells, which are the degrees of freedom of the problem, i.e., where the boundary condition is imposed. This discretization is made on the mean camber surface of the body and can be seen in Figure 6b. The filaments have a constant vortex strength Γ_i per element and they provide a velocity contribution to every control point calculated by an expression of the Biot-Savart law.

$$\boldsymbol{V}(r) = \frac{\Gamma_i}{2\pi h}(\cos\theta_1 - \cos\theta_2)\boldsymbol{e} \tag{4.1}$$

In this expression, the direction of the induced velocity can be obtained from the right-hand screw rule, and for each vortex-ring in the configuration, the above rule is applied four times.

The surface for our problem is the mean camber surface of each propeller blade; thus, the thickness effects are neglected. The geometry of the mean camber surface together with the wake is visualized in Figure 6 (a), where the start of the wake is marked by the trailing edge (solid black line). Also, within the context of the proposed VLM, the wake mesh is generated in the sense of cylindrical surfaces, based on the propeller's pitch distribution.

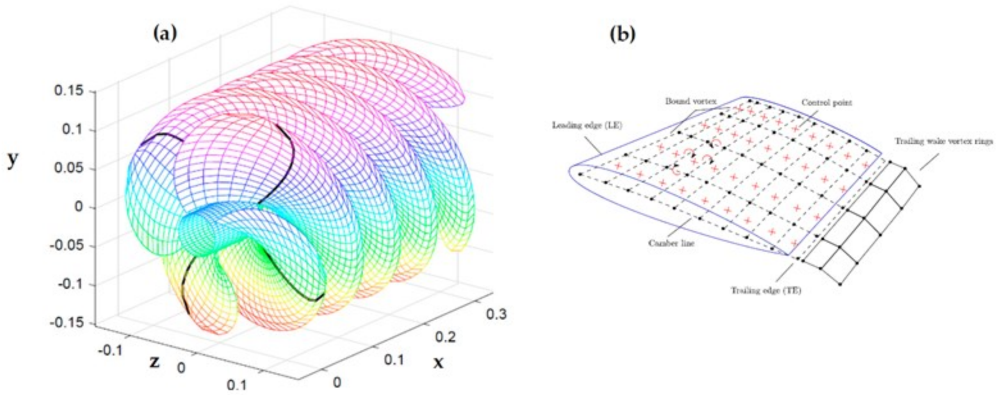

Figure 6: (a) Vortex element mesh on propeller blades with positive tip−rake (towards suction side) and corresponding trailing vortex wake mesh. (b) Schematic representation of the mesh and control points.

Regarding the boundary conditions, a flow-tangency condition is imposed on each control point on the propeller blade mesh, as follows

$$\left(\mathbf{V}_{\infty}+\mathbf{V}_{Bi}+\mathbf{V}_{Wi}\right)\cdot\mathbf{n}_{i}=0\,, \tag{4.2}$$

where $\boldsymbol{V}_{\infty}$ denotes the freestream velocity, $\boldsymbol{V}_{Bi}$ is the disturbance velocity generated by the bound vortex rings, $\boldsymbol{V}_{Wi}$ is the velocity induced by the trailing vortex wake, and $\boldsymbol{n}_i$ is the unit normal vector at the control point of the i^{th}-element $M_{ci}=(x_{ci},y_{ci},z_{ci})$. The freestream velocity contains both the axial part V_a and the tangential velocity ωr.

For the steady-flow problem treated here, an additional boundary condition, namely the Kutta condition, needs to be satisfied at the blade's trailing edge (TE). The no-through wall condition together with the Kutta condition are expressed as linear equations with the vortex strength Γ as the unknown. The resulting linear system of equations is

$$\sum_{j=1}^{Nel} A_{ij}\,\Gamma_j=-\boldsymbol{V}_{\infty}\cdot\boldsymbol{n}_i, \tag{4.3}$$

After the solution of the system, the velocities can be retrieved. From the definition of vorticity as a velocity jump via the lifting surface and the steady Bernoulli theorem [1], the following discrete expression for the pressure difference on each control point is used,

$$\Delta C_{pi}=C_{LE}\left(\frac{2V_m}{V_{\infty}^2}G_i\right), \tag{4.4}$$

where C_{LE} denotes a leading-edge suction force correction coefficient with typical values within the interval $0.85-0.95$.

Taking into account the symmetry between the blades in steady flow, the open water propeller characteristics [2], namely the thrust coefficient K_T, torque coefficient K_Q, and efficiency η at the selected advance coefficient, are obtained via the summation of contributions on the key blade:

$$K_T=n_{bl}\sum_{j=1}^{Nb}\frac{T_j}{n_{rps}^2D^4},\ \text{ with } T_j=A_j\left(0.5V_{\infty}^2\Delta C_{pj}n_{xj}-C_{Drag}V_{tx,j}|V_{t,i}|\right). \tag{4.5}$$

$$K_Q=n_{bl}\sum_{j=1}^{Nb}\frac{\left|Q_j+2Q_j^{Drag}\right|}{n_{rps}^2D^5},\ \text{where}$$
$$Q_j=A_j0.5V_{\infty}^2\Delta C_{pj}\left(n_{yj}z_{cj}+n_{zj}y_{cj}\right),\quad Q_j^{Drag}=A_jC_{Drag}0.5|V_{t,j}|\left(-V_{ty,j}z_{cj}+V_{tz,j}y_{cj}\right) \tag{4.6}$$

Expressions (5.6) represent the calculation of the reduced thrust K_T and torque K_Q for the whole propeller of n_{bl} blades. T_j, Q_j are the thrust force and torque developed by each vortex-ring element on the key blade respectively, A_j is the vortex ring surface area, n_{xj} is the unit normal vector projected on the *x*-axis, and the same holds for the tangent velocity component $V_{tx,j}$.

The calculation of thrust contains a friction-drag coefficient, which we express with C_{Drag}. This is a consideration of friction-drag effects, and its values are obtained using the empirical formula, $C_{Drag}=C_F+C_a(Re)\,a_{eff}^2$. The formula comprises of a skin-friction resistance coefficient $C_F=0.0858/[log_{10}Re+1.22]^2$ involving the local Reynolds number, the roughness of the blade's surface and a coefficient dependent on the effective angle of attack denoted by a_{eff} (see [3]).

Finally, we present the open water propeller efficiency grade:

$$\eta=\frac{J}{2\pi}\frac{K_T}{K_Q} \tag{4.7}$$

The numerical implementation of the VLM comes from a NTUA in-house code, whereas Matlab© is used for the pre- and post-processing of results. At the first stage, the surface blade mesher creates the vortex ring network to approximate the camber surface of one blade and then the solver, using rotation symmetry, takes into account the full geometry of the propeller.

4.1.1 CFD Solver

The CFD tool which was used in the present study is MaPFlow (see [4]), an in-house software developed at the National Technical University of Athens. MaPFlow can admit general polyhedral multi-block meshes and accounts for turbulent phenomena with the use of eddy-viscosity models. In our case, the unsteady Reynolds-Averaged Navier–Stokes Equations are solved (URANSE).

MaPFlow

MaPFlow solves the NS equations for compressible flows as well as at their incompressible limit. More specifically for the incompressible NS, which will be used for the current study, they are integrated in time using the artificial compressibility method [5],[6]. In all cases, the convective fluxes are discretized using the approximate Riemann solver of Roe [7] and the flow field reconstruction is performed with a second-order piecewise linear interpolation scheme. On the other hand, viscous fluxes are discretized using a central second-order scheme, along with the use of a directional derivative to account for the skewness of cells.

For the time integration, an implicit second-order backwards differentiation formula (BDF) is used together with local time-stepping in the pseudo-time iterations. Also, the implicit scheme demands that the non-linear advection terms are linearized in time using the Jacobian matrix.

The governing system of equations written in differential form consists of the continuity equation and momentum vector equations,

$$\begin{gathered}\frac{1}{\beta}\frac{\partial p}{\partial \tau} + \nabla \mathbf{u} = 0 \\ \frac{\partial \rho \mathbf{u}}{\partial \tau} + \frac{\partial \rho \mathbf{u}}{\partial t} + \nabla(\rho \mathbf{u}\mathbf{u}) + \nabla p + \nabla \cdot \bar{\bar{\tau}} = 0\end{gathered} \tag{4.8}$$

In the above equations, p and $\mathbf{u}$ denote the four unknown fields, which are the pressure, and the three-dimensional velocity field, with ρ denoting the constant density field, $\bar{\bar{\tau}}$ the tensor of the viscous stresses, and finally, τ and t the fictitious and real time, respectively. As already mentioned, the equations are augmented by the pseudo-time derivatives of the variables. The aim of the numerical procedure is to drive these derivatives to zero, therefore making the velocity field divergent-free and retrieving the original unsteady system of equations. The coupling of the equations is performed during the pseudo-time, where a relation between the density and the pressure field is assumed and controlled via the relation $\frac{\partial \rho}{\partial p}|_{\tau} = \frac{1}{\beta}$, where β is a free numerical parameter.

The present study examines the flow around a propeller. Therefore, the problem demands that the governing equations are solved in the relative frame of reference, in which the entire domain is rotating with an angular velocity $\boldsymbol{\omega}$. Let $\boldsymbol{r} = (x, y, z)$ be the position vector. By re-writing equation (5.8) with respect to the relative velocity vector $\mathbf{u}_r = \mathbf{u} - \boldsymbol{\omega} \times \mathbf{r}$ and performing some algebraic calculations we obtain the following expressions:

$$\begin{gathered}\frac{1}{\beta}\frac{\partial p}{\partial \tau} + \nabla \mathbf{u} = 0, \\ \frac{\partial \rho \mathbf{u}}{\partial \tau} + \frac{\partial \rho \mathbf{u}}{\partial t} + \nabla(\rho \mathbf{u}\mathbf{u}) + \nabla p + \nabla \cdot \bar{\bar{\tau}} - \rho(\boldsymbol{\omega} \times \mathbf{r}) = 0.\end{gathered} \tag{4.9}$$

We note that the mass equation (augmented continuity equation) remains unaffected by the variable transformation, since the mass balance is invariant to a system's rotation.

Meanwhile, we have a source term $-\rho(\boldsymbol{\omega} \times \mathbf{r})$ which expresses the Coriolis force due to rotation. The integration of the system over a control volume Ω with a corresponding boundary interface $\partial\Omega$, results in the following expression:

$$\boldsymbol{\Gamma} \int_{\Omega} \frac{\partial \mathbf{Q}}{\partial \tau} d\Omega + \boldsymbol{\Gamma}_{\mathrm{e}} \int_{\Omega} \frac{\partial \mathbf{Q}}{\partial t} d\Omega + \int_{\partial\Omega} (\mathbf{F}_c - \mathbf{F}_v) dS = \int_{\Omega} \mathbf{S}_q d\Omega \,. \tag{4.10}$$

In the above, $\mathbf{Q}$ is the vector of the unknown variables (pressure p and velocity $\mathbf{u}$). Also, the vector $\mathbf{S}_q$ contains various source terms, such as the Coriolis forces and $\mathbf{F}_c$, $\mathbf{F}_v$ are the vectors of convective and diffusive fluxes respectively, projected on a face. These two flux vectors are given by equation (5.11).

For the description of $\mathbf{F}_c$, $\mathbf{F}_v$ we need the normal vector $\mathbf{n} = (n_x, n_y, n_z)$ and ΔV which is the velocity difference between the contravariant velocity $V_n = \mathbf{u} \cdot \mathbf{n}$ and the grid face velocity due to the mesh motion $V_g = (\boldsymbol{\omega} \times \mathbf{r}) \cdot \mathbf{n}$. The convective and viscous fluxes are

$$\mathbf{F}_c = \begin{bmatrix} V_n \\ u\Delta V + p n_x \\ \rho v \Delta V + p n_y \\ \rho w \Delta V + p n_z \end{bmatrix}, \quad \mathbf{F}_v = \begin{bmatrix} 0 \\ \tau_{xx} n_x + \tau_{xy} n_y + \tau_{xz} n_z \\ \tau_{yx} n_x + \tau_{yy} n_y + \tau_{yz} n_z \\ \tau_{zx} n_x + \tau_{zy} n_y + \tau_{zz} n_z \end{bmatrix}. \tag{4.11}$$

The matrices $\boldsymbol{\Gamma}$ and $\boldsymbol{\Gamma}_e$ denote the artificial compressibility matrix and the transformation matrix from primitive to conservative variables, respectively,

$$\boldsymbol{\Gamma} = \begin{bmatrix} \frac{1}{\rho\beta} & 0 \\ 0 & \rho \bar{\bar{I}}_{3\times3} \end{bmatrix}, \quad \boldsymbol{\Gamma}_e = \begin{bmatrix} 0 & 0 \\ 0 & \rho \bar{\bar{I}}_{3\times3} \end{bmatrix}, \tag{4.12}$$

where $\bar{\bar{I}}_{3\times3}$ is the 3 by 3 identity matrix.

We are left with the calculation of viscous flux. For this, we use the Boussinesq approximation for turbulence modelling, as follows

$$\bar{\bar{\tau}} = \tau_{ij} = (\mu_t + \mu) \left(\frac{\partial u_i}{\partial x_j} + \frac{\partial u_j}{\partial x_i} \right) - \frac{2}{3} \rho k \delta_{ij}. \tag{4.13}$$

In equation (5.13), μ is the dynamic viscosity of the fluid, μ_t is the turbulent viscosity, k the turbulent kinetic energy, and δ_{ij} is the Kronecker's symbol. The turbulence viscosity is computed using the two-equation k-ω SST model of Menter [8]. The k-ω SST model is one of the most widely used RANS models and has a verified performance in simulating near-wall external hydrodynamic flows in the turbulent regime. Its use guarantees an adequate representation of the blade surface distribution of pressure and shear stresses as well as the wake structures (followed by the appropriate mesh refinement).

Simulation setup

Usually, in open-water propeller simulations the flow in the relative frame is considered steady. In order to reduce the number of cells used for meshing, we simulate only one blade. This means that the entire domain becomes prismatic (see Figure 7) while both left and right faces of the domain have periodic boundary conditions. The far-field boundary is an adequately large cylinder spanning 5 propeller diameters radially and 10 diameters after the propeller. These dimensions are chosen as a standard ITTC practice for open water propeller simulations.

Additionally, the hub of the blades is a cylinder of the diameter equal to $1/5$ of the propeller's diameter with a semi-spherical ending ahead of the blade. In the hub boundary, no-through conditions are applied, i.e. $\frac{\partial u}{\partial \boldsymbol{n}} = 0$, in order to exclude the hub from the force calculation.

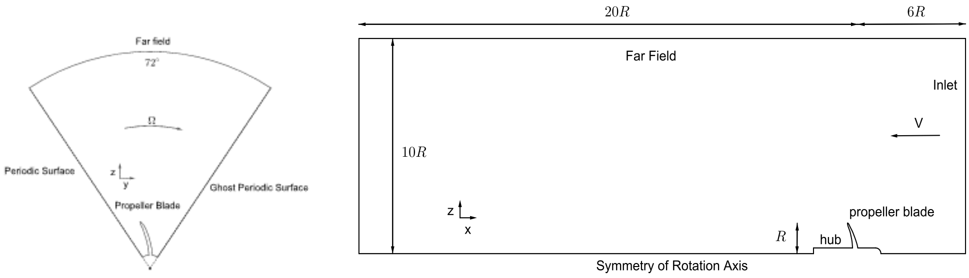

Figure 7: The basic computational setup used for the CFD simulation.

4.1.2 Tip Rake Optimization

The optimization study is based on the reformation of the blade's rake, which is the longitudinal deviation from the root's position. First, we explain which way is followed in order to parameterize this geometric quantity and following, the optimization procedure is presented.

Parametric Model for the Tip-Rake Reformed Geometry

The geometrical model used to represent the rake distribution consists of a combination of linear and quadratic terms. Starting from the blade root up to a selected transition point, the rake is linear, i.e., typical generator line rake, whereas after the transition point, the rake distribution is quadratic. The two degrees-of-freedom (dofs) for the rake, after we demand slope continuity between the linear and the quadratic segment, are: 1) the radial position of the transition point and 2) the maximum non-dimensional rake at the tip. In Figure 8, a schematic representation of the 2-dof rake parametric model is provided which explains the rationale.

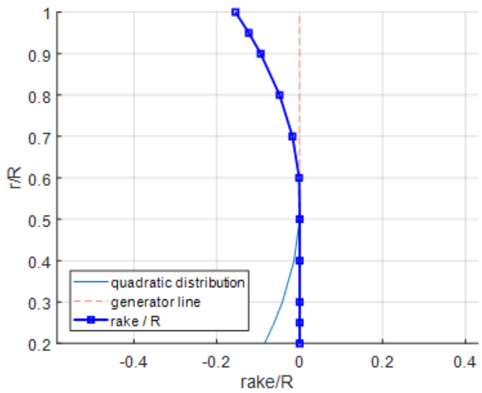

Figure 8: Tip-rake 2-dof parametric model, based on a linear and quadratic distribution.

The pitch and maximum camber distributions are also quantities under modification. Firstly, the reference distributions are approximated using B-Spline interpolation (4^{th}order). Then we set a specified value of radius, which we use to make out which control points of the B-Spline will be modified. In our case the active control points are these that reside in a radius greater than half of the blade's ($r/R > 0.5$). This model is shown in Figure 9, where the red squares denote the activated control points of the pitch representation that are multiplied with the coefficient.

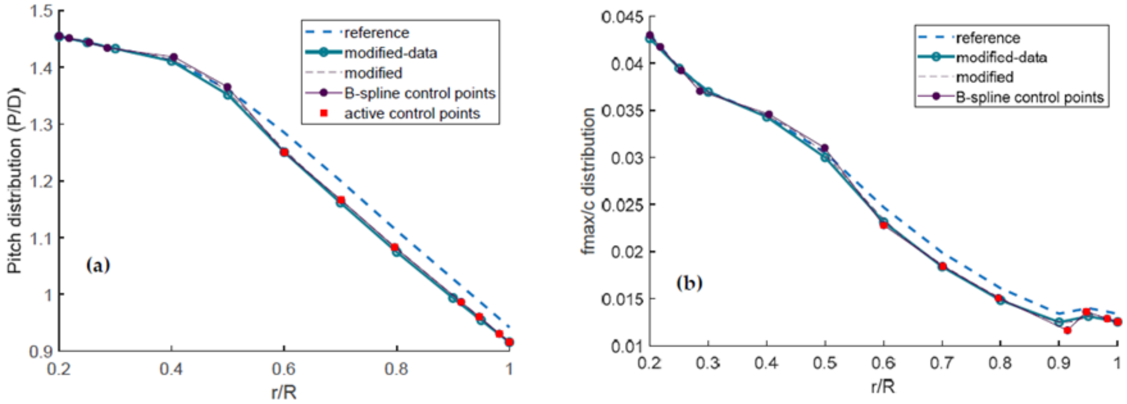

Figure 9: Pitch (left) and maximum camber distributions (right).

This approach ensures that the distributions remain unaltered in the vicinity of the root section to avoid flow separation near the hub.

In summary, we use a 4-dof parametric model controlling the tip-rake, pitch, and maximum camber distributions to construct an optimization strategy.

Optimization Problem

The present study is focused on enhancing the propulsive performance of the reference propeller at the design advance coefficient. This will be achieved by optimally tuning the 4 dofs to generate a modified geometry with a distinct tip-rake reformation without significant thrust reduction at the design advance ratio. The examined optimization problem is formulated as follows,

$$\min_{x} f(x) = 10K_Q(J_d)$$
$$such\ that \begin{cases} (1-p)K_{Treq}(J_d) \leq K_T(J_d) \leq (1+p)K_{Treq}(J_d) \\ lb \leq b_n \leq ub \end{cases} . \tag{4.14}$$

In the Equation 4.14, $f(x)$ is the objective function, J_d is the propeller's advance coefficient at the design point and $b_n = \{x_1, x_2, x_3, x_4\}$ denotes the design variable vector that contains the geometric dofs and with lb, ub and K_{Treq} being the lower, upper bound for control point values and the required thrust coefficient respectively. Also, p is a tolerance measure for the thrust constraint and is set to 3.5%.

Regarding the design variables, x_1 denotes the radial position of the transition point in tip-rake distribution, x_2 is the maximum non-dimensional rake at the tip, x_3 the pitch proportional coefficient and x_4 the maximum camber proportional coefficient, as discussed in the previous section.

It is also important to note that the propeller sections are kept the same, similarly to the experiments from [10], where a NACA $a = 0.8$ mean line and a NACA 66-modified thickness distribution is considered. In this regard, a similar approach from Kinnas et al. [11] is implemented for the problem of optimal blade design using constraints targeting torque minimization under a fixed thrust. In their work, VLM is used for the optimization studies, whereas RANS-CFD simulations were also performed for further analysis, indicating that the methodology presented here can also be extended for the design of propeller sections.

It is important to stand out that the gain in efficiency is a result of the modification of the resulting pressure distribution on the modified propeller blade. However, the effects on tip-rake reformation, as well as the modification in the pitch or maximum camber distribution, on the cavitation performance of the blade are non-trivial and future work will be focused on investigating these effects. Nonetheless, some unconventional propeller geometries, such as the CLT propellers or KAPPEL propellers, yield efficiency enhancement but may be prone to other types of cavitation [3].

For the solution of this optimization problem, we use the nonlinear programming Matlab© solver "*fmincon*". The results presented in this work are produced using the sequential quadratic programming algorithm via the "*sqp*" option that is suitable for handling nonlinear constraints. This methodology requires the definitions of the upper and lower bounds of our dofs (Table 5).

In more detail, the Hessian matrix must be calculated, which is achieved with central finite differences. All VLM numerical simulations were performed on a typical workstation in which, a typical evaluation of a candidate solution requires a few seconds for a spatial discretization per blade of $(NEC, NEA) = (8,15)$, where NEC, NEA refer to the number of elements per chord and number of elements per span respectively.

Table 5: Design variable bounds.

ID	Description	Lower Bound	Upper Bound
x1	Rake transition point	0.30	0.90
x2	Maximum rake (Xr/R)	$-0.12D/R$	$0.12D/R$
x3	Pitch proportional coefficient	0.95	1.05
x4	Maximum Camber proportional coefficient	0.85	1.25

where D is the diameter and X_r is the absolute rake length at the tip of the blade.

4.1.3 Results for the Optimization of NSRDC 4381 & 4382 Propellers

This section is organized in the following way. First, we conduct a sensitivity analysis of results both for VLM and CFD. Then, the open water curves are presented for the initial design of 4381 and 4382 blades. At this point, the VLM will be used for the optimization process and the resulting optimal design will be simulated by MaPFlow in order to validate the trend.

Sensitivity Study of NSRDC 4381

This preliminary study involves the first design which has zero skew angle (NSRDC 4381) and the simulations are run for the design advance coefficient, which is $J = 0.889$. In order to retrieve comparative results, we gradually increase the dofs of the discrete problem and compare the differences from coarser to denser discretizations.

For the VLM, results are presented in Table 6. On this basis, a mesh of 15×8 vortex rings on each blade is selected. For the analysis, the leading edge suction force coefficient C_{LE} and the viscous drag C_{drag} are tuned based on the experimental data from [10]. The reference quantities are the open water curve metrics; namely, the thrust coefficient (K_T), the torque coefficient $(10K_Q)$, and the efficiency (η). The calculated differences with respect to the denser mesh show that the error has a decreasing rate up to the (30×15) mesh. This indicates that results for this mesh are insensitive.

Table 6: Vortex-lattice model mesh sensitivity for 4381 at design J = 0.889.

		Grid Mesh Sizes. Diff% Compared to Finer Grid Results					
	Exp. data	(11 × 6)	(13 × 7)	(15 × 8)	(20 × 10)	(30 × 15)	(40 × 20)
K_T	0.208	4.39	3.90	1.95	0.970	0.00	-
$10K_Q$	0.445	4.35	3.89	2.28	0.91	−0.22	-
η	0.661	−0.301	−0.301	−0.301	−0.151	−0.151	-

For MaPFlow (CFD), we increase the cell density on all boundaries and for controlled-cell regions of the mesh. This way we create three discretizations. The results from these simulations can be found in **Errore. L'autoriferimento non è valido per un segnalibro.** with respect to the denser mesh, and in Table 8 with respect to experimental data. Similar to the VLM, we first show that errors have a decreasing rate. This is also true for the comparison with experimental data from [10] (shown in Table 8). In conclusion, it suffices to use the middle mesh for the following simulations.

Table 7: MaPFlow 4381 mesh sensitivity at design advance ratio with respect to dense mesh.

	Cells (Million)	**Err K_T(%)**	**Err K_Q(%)**
Coarse	2.3	4.7	3.42
Mid	7.5	0.72	1.127
Dense	12.7	-	-

Table 8: MaPFlow 4381 mesh sensitivity at design advance ratio with respect to experiments.

	Cells (Million)	**Err K_T (%)**	**Err K_Q (%)**
Coarse	2.3	7.01	10.08
Mid	7.5	5.00	7.19
Dense	12.7	3.90	6.40

Open Water Curves for NSRDC 4381/4382

The next step is to validate the initial designs of the two blades (4381 and 4382) with experimental data. These results are shown in Figure 10 and Figure 11.

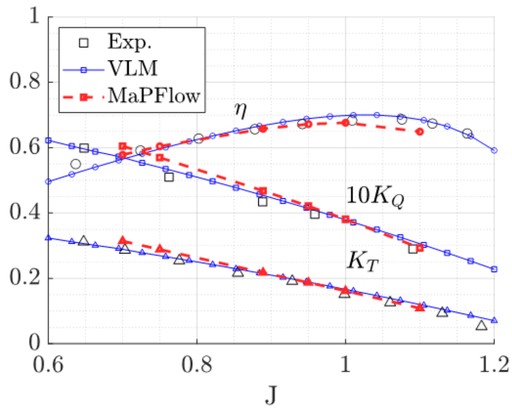

Figure 10: Open water curves comparison for 4381.

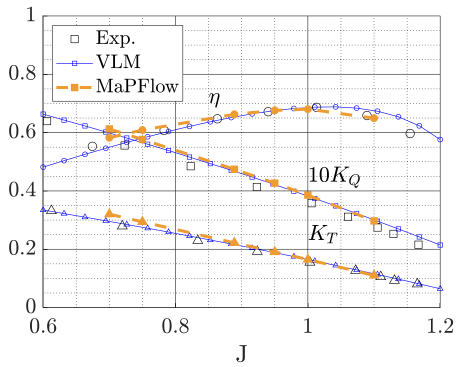

Figure 11: Open water curves comparison for 4382.

For both graphs, the comparison is made among experimental data [9], vortex-lattice and MaPFlow. There, the thrust coefficient results are depicted with triangles, the moment coefficient with squares and the efficiency with circles. For Figure 10 the results for vortex-lattice are obtained using $C_{Drag} =$

0.0045 and $C_{LE} = 0.93$, whereas the vortex-lattice results of Figure 11 are obtained using $C_{Drag} = 0.0050$ and $C_{LE} = 0.90$. In both graphs, numerical and experimental results are in good agreement.

Optimization results

For the optimization, a starting radius of $r/R = 0.5$ was chosen for the lower radius where the rake becomes quadratic. The resulting optimal design is presented in Table 9. We notice the following: 1) the optimal maximum rake (x_2) in both cases (4381 and 4382) corresponds to a suction-side rake (positive rake) and, 2) the optimal pitch and maximum camber proportional coefficients are smaller than the corresponding value of the reference geometry.

Table 9: Optimization results.

ID	Description	4381	4382
x_1	Rake transition point	0.7136	0.6430
x_2	Maximum rake (Xr/R)	0.2397	0.2414
x_3	Pitch proportional coefficient	0.9845	0.9862
x_4	Max. camber proportional coefficient	0.9689	1.0635
-	Active control points	all	r/R > 0.5

The validation with CFD is presented in Table 10. The simulations for the modified geometries reveal that the thrust and torque have decreased compared to the initial geometries. However, this results in an approximately 1% increase in efficiency for the NSDRC 4381 blade, according to CFD. The increase in efficiency is also present for the NSDRC 4382 blade, but at a smaller percentage (0.5%). Lastly, it has to be mentioned that, while for the 4381 design, VLM and CFD agree on the reduction of thrust and torque, CFD shows an increase in both these metrics when examining the modified design of the 4382 propeller.

Table 10: Modified propeller performance at J = 0.889.

	4381		4382	
	VLM	MaPFlow	VLM	MaPFlow
dK_T (%)	−3.228	−4.265	−3.478	2.787
dK_Q (%)	−3.989	−5.326	−4.637	2.308
dη (%)	1.857	1.122	1.216	0.468

4.1.4 M/V Kastor Propeller

Propeller Geometry

Not all the geometric characteristics were available for M/V Kastor Propeller. Additionally, the towing tank propeller model was different than the one used in the full-scale ship. To this end, the geometry of the propeller was reconstructed using vortex lattice potential method and verified by CFD simulation. Comparison of the reconstructed propeller open water characteristics with the ones provided can be seen in Figure 12.

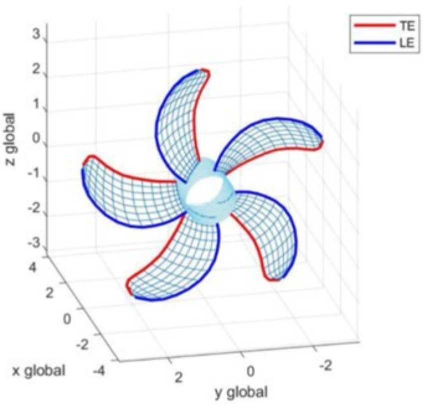

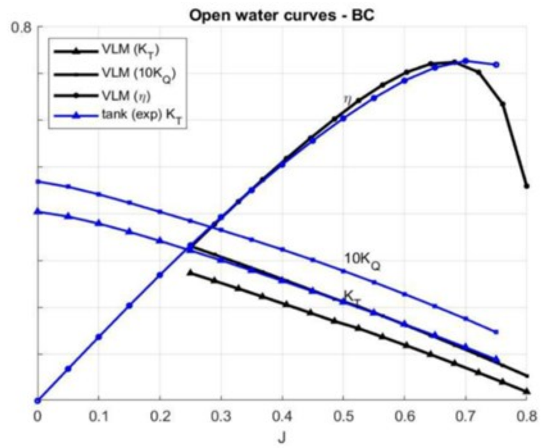

Figure 12: Reconstructed propeller geometry (left). Comparison of reconstructed propeller open water curves with the open water tests provided for M/V Kastor (right).

Domain discretization & Simulation setup

The propeller at hand is the R55 model which has a nominal diameter of D=6.95 m and consists of 5 blades. Because the propeller has rotational symmetry, we can divide the domain of simulation by the number of blades and simulate only one blade inside a cylindrical slice. The boundary conditions on the radial slices are periodic, which means that boundary values in halo cells of the first periodic surface are taken from inner boundary cells of the second. Concerning the far field surfaces, the radial distance far field is located at 33m from the shaft axis, the upwind face is 40m and the downwind face is 100m distant from the propeller blade.

Grid Independence Study

Three different grids were generated of increasing size namely, the coarse, the medium and the dense mesh. For all the meshes used the $y^+ \leq 1$ since now wall functions were employed. Regarding the refinements regions the three grids differ in terms of the number of layers grown outwards of the blade, blade surface discretization and size of the cells of the wake refinement zone downstream of the blade (see Figure 13). The study was conducted for the design advance coefficient, which is J = 0. 707. Details can be found in Table 11:

Table 11: MaPFlow: Mesh sensitivity at design advance ratio with respect to dense mesh.

	Cells (Million)	**Err K_T(%)**	**Err K_Q(%)**
Coarse	2.7	5.7	3.1
Mid	7.5	0.3	0.5
Dense	12.5	-	-

Following the grid independence study, it is evident that the medium mesh consisting of 7.5 million cells can be employed for the rest of the study.

Computational Grid

Since the medium mesh will be used for the rest of the work it's useful to provide some additional information about the main characteristics. In terms of blade discretization, its spanwise cell density is $1\,mm$ at the leading edge and $10\,mm$ at the trailing edge. Also, its chordwise density is (at max) approximately $7\,mm$ at the root of the blade $(0.2R)$ and $4.5\,mm$ at the blunt tip $(1.0R)$. Finally, its maximum cell dimension due to unstructured mesh creation, where the curvature is small, is close to $60\,mm$, and at the (highly curved) region of the leading-edge strip, the chordwise dimension starts from $0.1\,mm$ before its gradual increase. Due to presence of the (artificial) hub at the fore of the blade, we prefer to subtract its contribution to drag and therefore we set the boundary condition to be "slip & no-through".

The specification of the volume mesh near the blade wall follows the y^+ criterion, used for RANSE simulations, in which, for $y^+ = 1$ we obtain a first cell height $h_1 = 0.0025\,mm$. A wake refinement region is defined downstream of the blade spanning 1.5 diameters with a maximum cell length of 50 mm. The above resulted in a volume mesh consisting of around 7.5 million cells while the blade surface mesh consisting of around 150 thousand cells. The representation of the computational mesh, both volume and surface mesh can be seen in Figure 13.

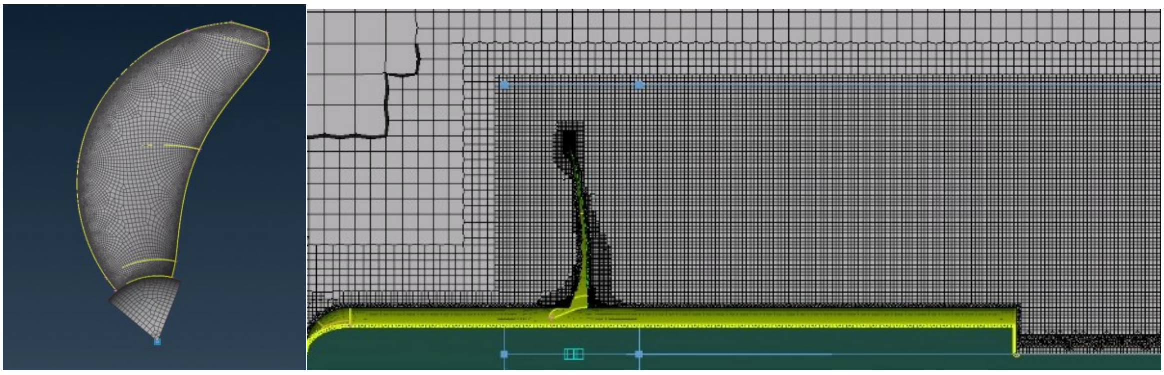

Figure 13: Near view of the blade mesh (1 blade is modelled with periodic boundary conditions (left). Wake refinement downstream of the blade (right).

Tip Rake Optimization

Regarding the tip rake modifications, we conducted an optimization procedure described previously for the M/V Kastor propeller (R55 propeller). The resulting geometry can be seen in Figure 14.

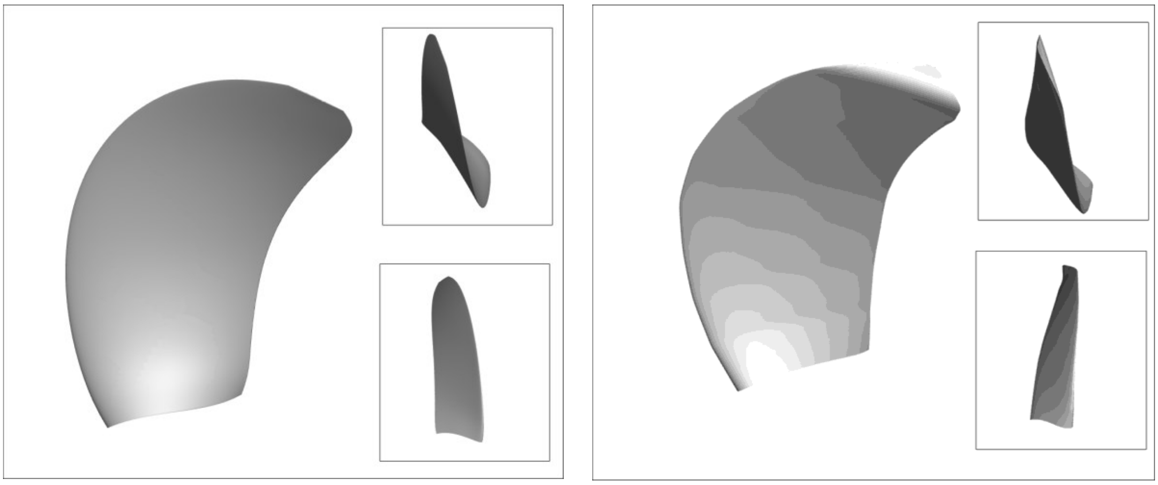

Figure 14: Original geometry (left). Modified tip-rake geometry (right).

The performance of the propeller is assessed using the advance coefficient $J = \frac{V_\infty}{nD}$, the thrust coefficient $k_T = \frac{T}{\rho_m n^2 D^4}$, the torque coefficient $k_Q = \frac{T}{\rho_m n^2 D^5}$ and the efficiency, defined as : $\eta = \frac{J}{2\pi}\frac{k_T}{k_Q}$.

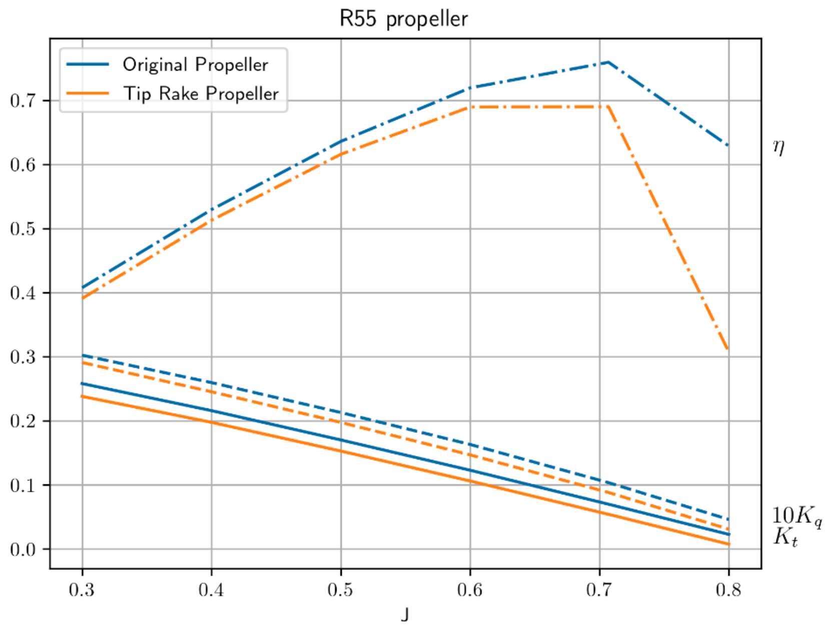

Figure 15: Open Water Characteristics comparison for original and modified tip-rake propeller.

By comparing the open water characteristics of the two variants in Figure 15, it is clear that in this case altering the tip rake of the propeller results in a degradation of the propeller performance at higher advance coefficients, while in the lower regime there are no significant differences noted.

4.1.5 Cavitation Investigation

In this section the M/V Kastor (R55 propeller) cavitation performance is investigated. A parametric study is conducted for four cavitation numbers defined as $\sigma = \frac{T}{\rho_m n^2 D^5}$ for several advance coefficients. The computational grid used is the same as defined in the previous consisting of 7.6 million cells. The Kunz cavitation model is employed as described in [12]. The simulations that follow consider 6 cavitation numbers namely $\sigma =$ 0.85, 1.05, 1.25, 1.5, 1.85 and 2.05. Four advance coefficients were investigated from *J*=0.3-0.6 since at J=0.6 no cavitation is predicted even for the lowest cavitation number.

Initially qualitative results are presented illustrating the predicted cavitation (Figure 16 - Figure 19).

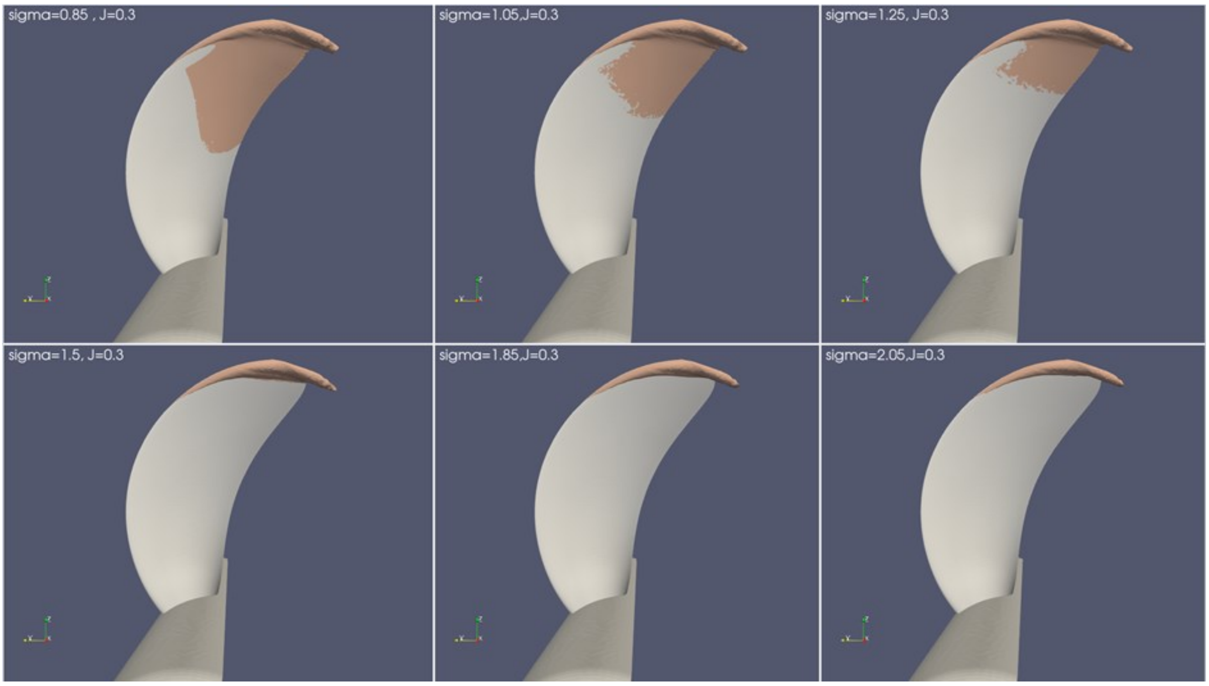

Figure 16: Cavitation sheet for the various caviation numbers at advance coefficient J=0.3.

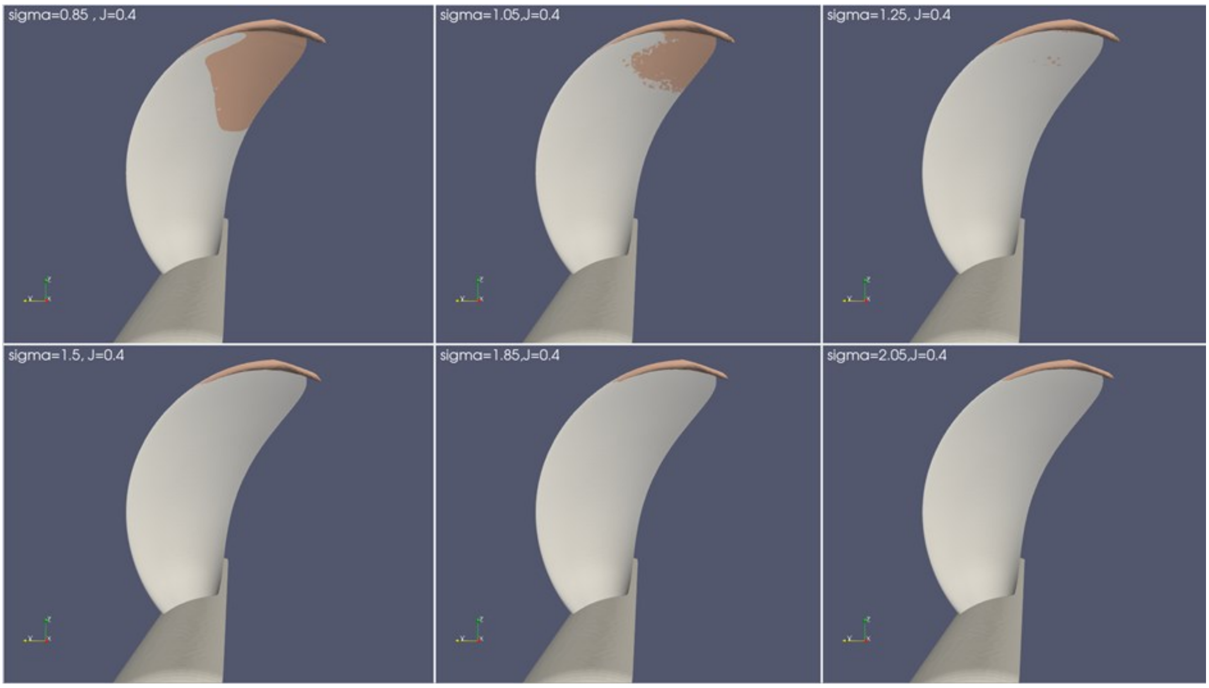

Figure 17: Cavitation sheet for the various cavitation numbers at advance coefficient J=0.4.

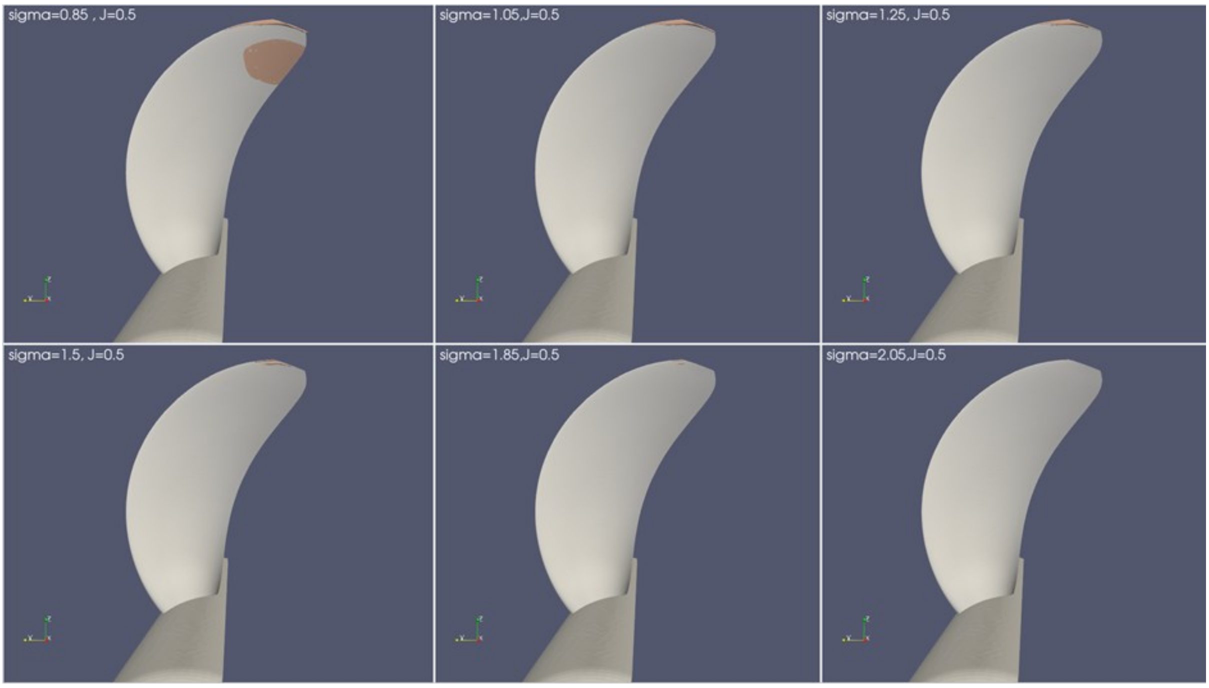

Figure 18: Cavitation sheet for the various cavitation numbers at advance coefficient J=0.5.

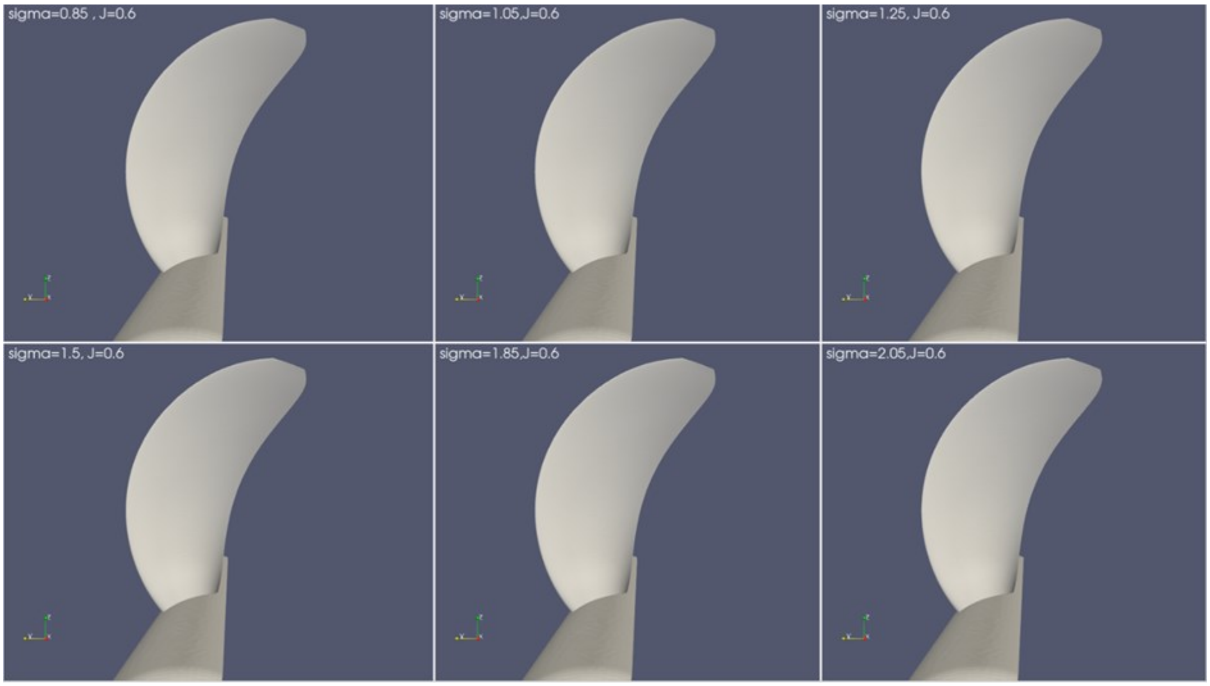

Figure 19: Cavitation sheet for the various cavitation numbers at advance coefficient J=0.6.

Based on the cavitation behavior across different operating conditions, it can be seen that the lowest advance coefficient of J=0.3, representing heavily loaded propeller conditions, significant cavitation is observed up to σ=1.25, indicating extensive vapor formation across the blade. Beyond this cavitation number, the phenomenon becomes confined to the tip region only.

As the advance coefficient increases to J=0.4 and J=0.5, there's a notable reduction in cavitation intensity and extent. At J=0.4, cavitation becomes primarily a tip phenomenon for σ≥1.05, while at J=0.5, cavitation only occurs at the lowest cavitation numbers (σ=0.85 and 1.05). This progressive reduction in cavitation with increasing advance coefficient aligns with the expected behavior, as higher advance coefficients generally correspond to lighter propeller loading and consequently higher local pressures that inhibit cavitation formation.

Finally, the open water of characteristics of the propeller considering cavitation can be found in Figure 20. The above remarks are evident in the open water characteristics of the propeller, where it is noted that that cavitation affects the thrust of the propeller for advance coefficients J<=0.5.

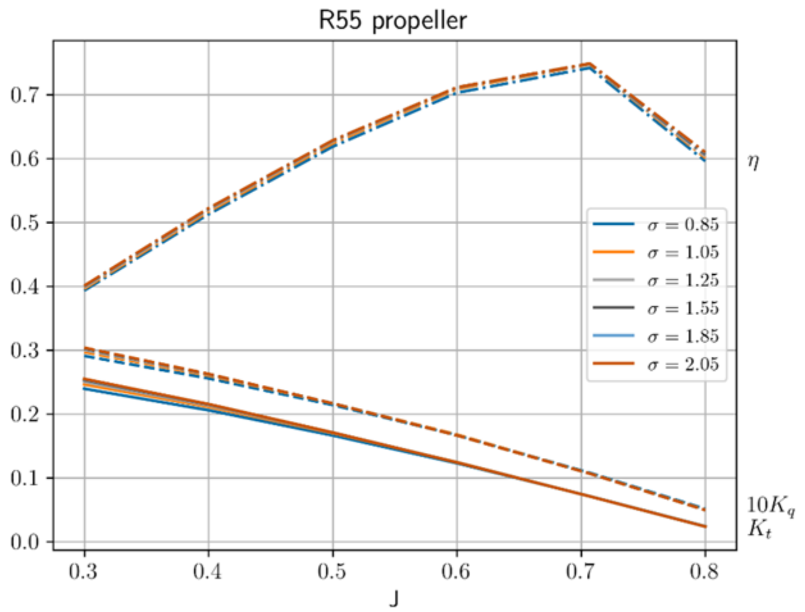

Figure 20: Open Water Characteristics for R55 propeller for different cavitation numbers (σ).

4.1.6 Blade Roughness

In this section the effect of roughness will be investigated for the R55 propeller with and without considering cavitation. Roughness is introduced with the use of wall functions by altering the wall function equation with an added parameter that accounts for amount of roughness. As in the previous the two-equation k-ω SST model of Menter [8] is employed. Regarding the near wall treatment, MaPFlow utilizes an “automatic” wall functions approach [12] that depending on the y^+ it switches between the low Reynolds and wall functions approach. In case roughness is considered by altering the log-law of the wall as proposed in [13]. To that end, the log-law of the wall is modified by introducing an additional term, namely ΔU^+:

$$u^+ = \frac{1}{\kappa}\ln(y^+) + B - \Delta U^+ \tag{4.15}$$

In the above $\kappa = 0.41$ is the von Karman constant and $B = 5.1$. Using the above equation one can represent the change in the velocity profile due to roughness using the additional term ΔU^+. Of course, by setting this term to zero the original “smooth” wall functions are recovered. The roughness functions are defined as $\Delta U^+ = \frac{1}{\kappa}\ln(1 + k^+)$, where k^+ is the non dimensional roughness defined, as $k^+ = \frac{k\, u_\tau}{\nu}$. In the previous k is the roughness in μm, u_τ is the friction velocity and ν the kinematic viscosity of the fluid. Typical values of k for the propeller fouling conditions can be found in [14]. The roughness conditions considered in this work can be found in

Table 12:

Table 12: Typical roughness values depending on the propeller blade condition considered in this work.

Roughness in μm (k)	Blade condition
0	Clean blade
50	Very Light Fouling
100	Deteriorated coating or light slime
300	Heavy slime

The open water characteristics for three values of roughness namely $k = 50{,}100{,}300\ \mu m$ can be found in Figure 21. As expected, the propeller performance degrades as the amount of fouling is increased.

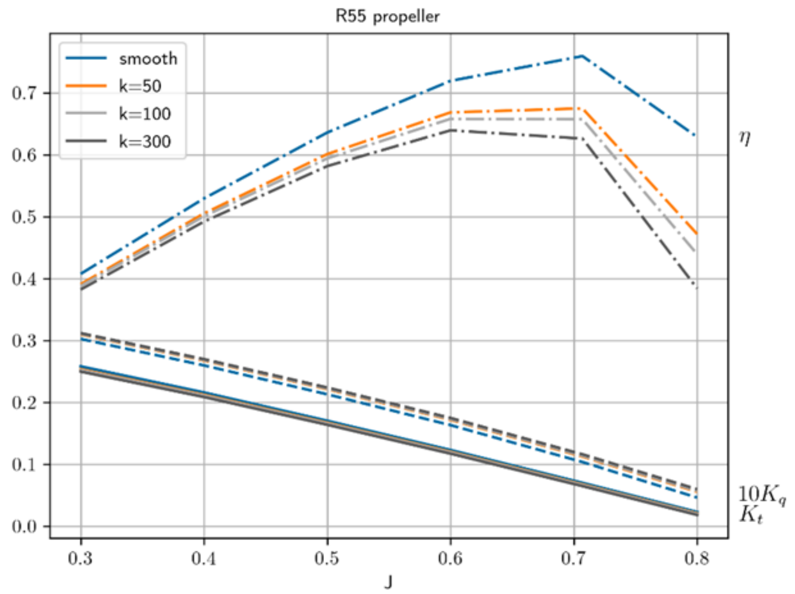

Figure 21: Open water characteristics for the R55 propeller considering fouling conditions.

Propeller performance gets even worse when both roughness and cavitation are considered ($\sigma = 0.85$). In fact, propeller fouling induces cavitation on most of the blade as it can see in Figure 22. Compared to the smooth propeller (Figure 16) it is evident that cavitation covers the most part of the blade up to $J = 0.5$.

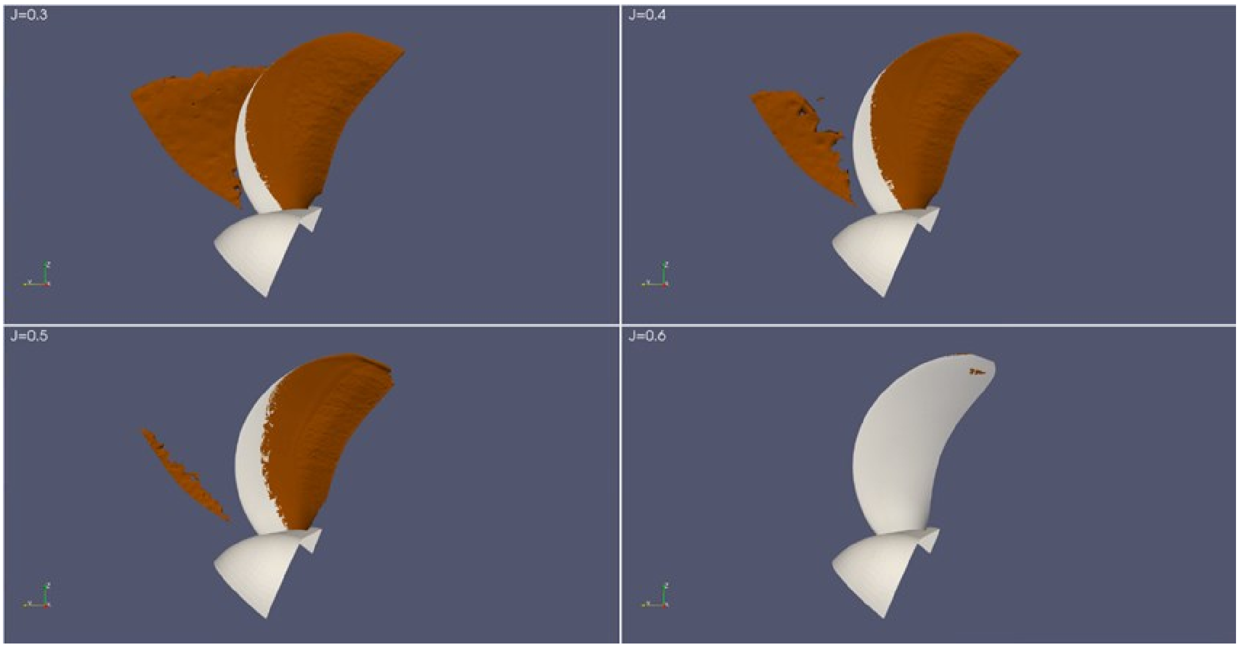

Figure 22: Cavitating propeller blade-fouling conditions.

The roughened surface appears to promote more extensive cavitation formation, with the sheet covering a larger portion of the blade area compared to the smooth propeller case. This increased cavitation is particularly impactful at lower advance coefficients, where the propeller is already operating under higher loading conditions. The data presented in Figure 23 specifically illustrates how this combined effect most severely impacts performance in the low advance coefficient regime, indicating that the fouled propeller is particularly susceptible to performance degradation through the dual mechanisms of increased friction and enhanced cavitation formation.

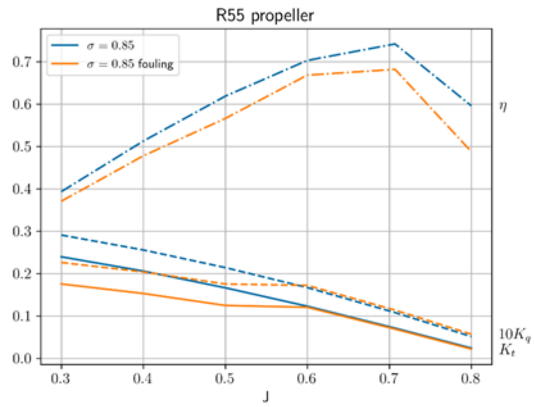

Figure 23: Open water characteristics of fouled R55 propeller considering cavitation at $\sigma = 0.85, k = 100\mu m$.

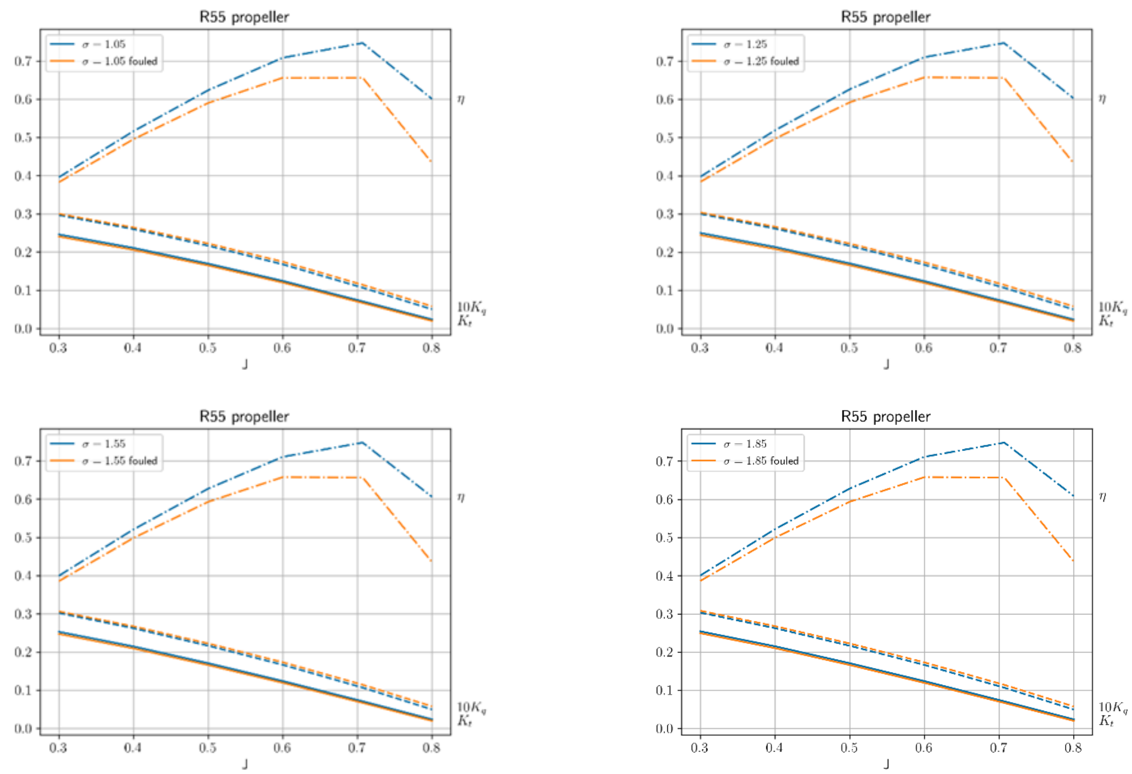

Figure 24: Open water characteristics of fouled R55 propeller considering cavitation at $\sigma = 0.85 - 1.85, k = 100\mu m$.

In Figure 24 the open water characteristics for the higher cavitation numbers can be found. Firstly, for the given cavitation numbers σ, the cavitation formation appears to be minimal on the fouled propeller with surface roughness k=100μm. This despite the roughened surface there is almost no cavitation. Secondly, it can be noted that, there's minimal difference between the propeller's open water characteristics whether cavitation is included in the analysis or not. This indicates that for this specific combination of operating conditions (the given cavitation number) and fouling level (k=100μm), cavitation does not appear to be critical for the propeller performance.

4.2 Bulbous Bow Optimization

Ship design is considered as a particularly complex procedure, requiring successful combination of many disciplines. During this process, designers are relying extensively on the use of specialized software tools, while at the same time they are benefiting from past experience gained from similar designs. Nowadays, CASD systems are widely used as part of the ship design process, allowing multiple solutions to be simultaneously examined. The introduction of parameterization allows the elaboration of optimization studies in ship design, enabling the identification of preferable solutions in the design space, based on specific requirements. The parametric modelling method may also be considered at later stages, even when the initial ship design process has been completed, in order to evaluate the performance of the vessel, or even to explore possible alternative retrofit solutions for existing ships improving the operational performance. In the framework of WP2 Task 2.1 of RETROFIT55 research project, a retrofit solution for bulbous bow addition in a bulk carrier vessel was examined on the basis of a developed parametric model for the transformation of the bow and the evaluation of the ships' performance based on specific operational scenarios. The parametric model was developed in CAESES software, offering the possibility to control/specify the main dimensions of the bulbous bow of the vessel. CAESES is a powerful software platform, providing simulation-ready parametric CAD for complex free form surfaces and targets CFD-driven design processes, automated design explorations and shape optimization solutions. The developed parametric model in CAESES has been integrated with Shipflow software by Flowtech, performing calm water resistance calculations based on potential flow theory and was applied for the optimization of the selected bulk carrier with the bulb addition based on specific operational scenarios. The Shipflow results have been validated also using the CFD viscous flow software tool FINE Marine by NUMECA.

4.2.1 Geometric model

The first stage of the study included the hull generation of the reference vessel. To this end, a 3D geometric model of the hullform was developed, as depicted in Figure 25. The model for the hull surface was primarily constructed using a set of curves, forming the so-called hullform definition grid. The selection of grid curves and the definition order were the two main steps for the surface generation. Particular attention was given during the hullfom generation to ensure adequate quality and fairness, in order to be suitable for CFD calculations. A bulb was then added to the model on the basis of the retrofit concept, as shown in Figure 26.

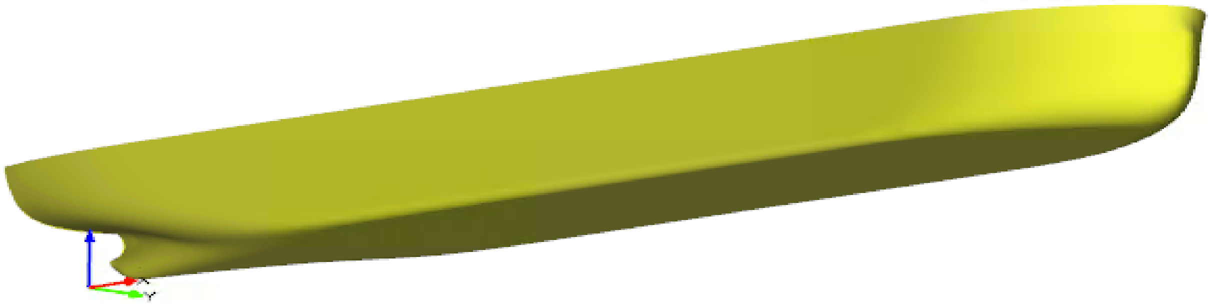

Figure 25: Generated hullform based on reference bulk carrier vessel.

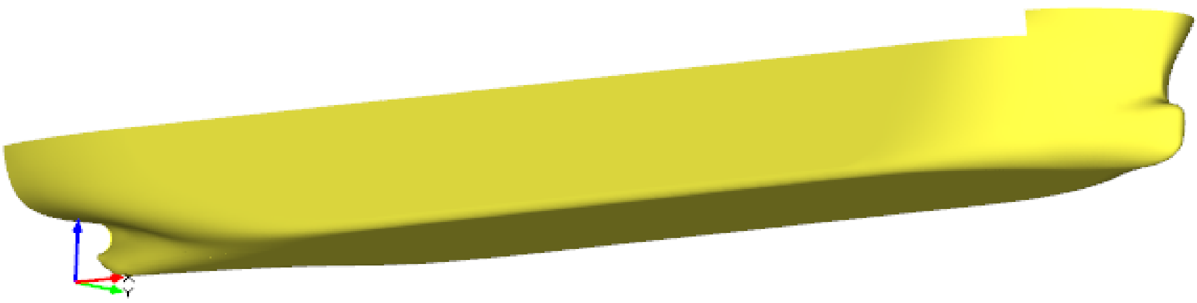

Figure 26: Generated hullform based on reference bulk carrier vessel after the bulbous bow addition.

The new hullform with the bulbous bow addition was then imported in CAESES software to perform geometry parameterization and transformation based on the Free Form Deformation (FFD) approach. The purpose of the transformation was to produce modified hullforms of a given parent hull. The Free Form Deformation (FFD) approach first sets a domain surrounding the part of the geometry to be morphed. A regular grid based on a set of control points is then defined and the deformation of the geometry is performed in a continuous and smooth way by moving the selected control points from their latticial positions. To this end, a surrounding domain box for the bulbous bow area forward of the collision bulkhead was defined based on a set of design variables (form parameters) concerning local hull details regarding the bulb dimensions. The region of interest and the domain that was defined based on the control points are shown in Figure 27. A set of design variables was defined to control the bow dimensions and more specifically the length, the vertical extension and the width of the bulb, as presented in Figure 28. If a positive value is given to the bulb length variable, the defined control points will move extending the domain box and the length of the bulb will increase. A negative value will reduce the size, making the bulb shorter. Bulb vertical extension variable was actually divided into two sub-variables which work in a similar way to bulb length. These sub-variables control the upper and lower vertical limit of the bulb. A positive value will increase the height of the upper/lower bulb point, modifying the rest of the bulb shape smoothly to fit with the new position. A negative value, on the other hand, will decrease the z-coordinate of the upper/lower bulb point. Bulb width influences, as the name suggests, the width of the bulb. This variable is controlled also using a grid of control points inside the domain box. A positive value will make the bulb more rounded transversally, while a negative value will make it more flat in this plane. The range of values that is acceptable for each variable varies from one to another. The selected ranges for the bulb variables to produce feasible and realistic design alternatives are presented in Table 13.

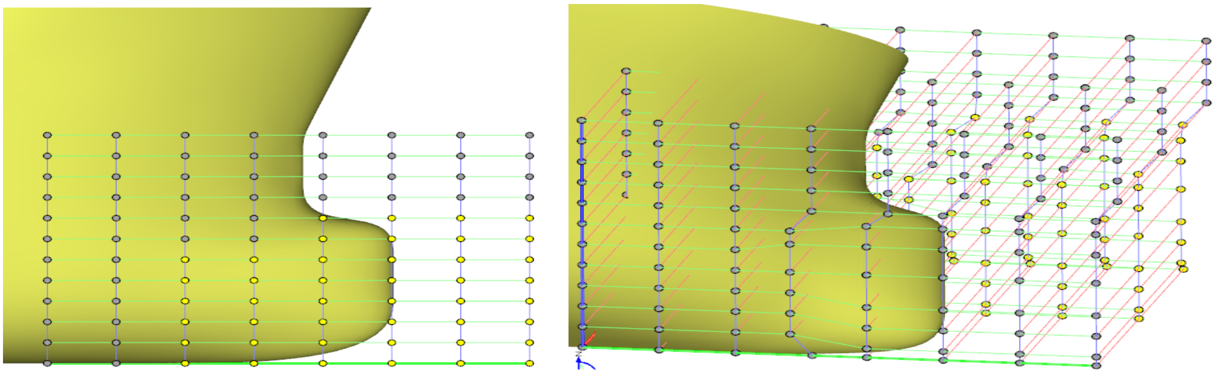

Figure 27: Domain box surrounding bulb area forward of collision bulkhead a) profile view and b) 3D view.

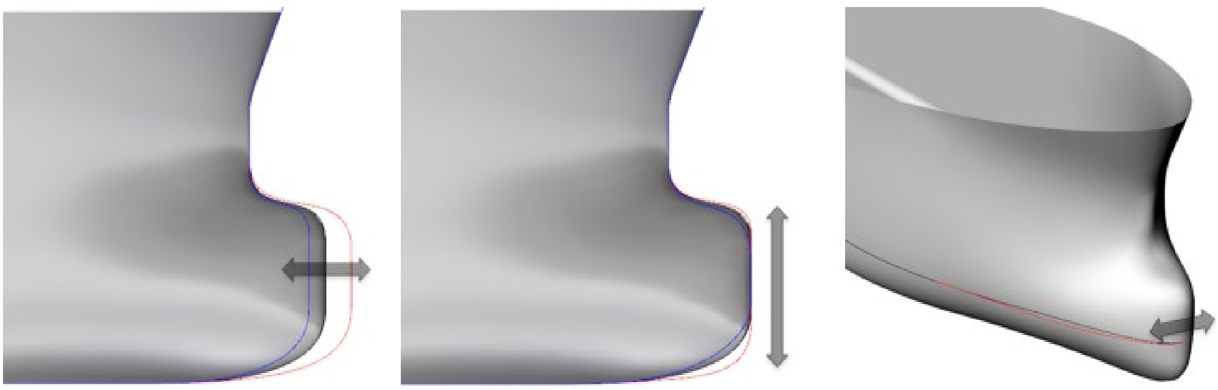

Figure 28: Bulbous bow design variables controlling bulb length (left), vertical extension (centre), and bulb width (right).

Table 13: Range of bulb design variables.

Bulb design variable	Min value	Max value
Bulb Length	-1.0	1.5
Bulb vertical extension (Up)	-1.2	0.5
Bulb vertical extension (Down)	-0.8	0.6
Bulb width	-0.5	1.2

4.2.2 Hydrodynamic assessment

After the 3D geometric model generation, the next stage of the study was the elaboration of hydrodynamic assessment and more specifically the calculation of calm water resistance. The evaluation was performed using the commercial software tool Shipflow by Flowtech.

The potential flow solver of Shipflow software was used for the calm water resistance evaluation. Potential flow methods are considered as a very powerful tool especially during optimization studies. The main advantage lies in the usually acceptable levels of accuracy in ranking design modifications in combination with the short computation time. The short computation time makes it possible to try many different variants or to set up parametric optimization studies that will be completed within reasonable time. Shipflow can either compute wave resistance with linear or non-linear calculations. The linear method is quite fast and usually provides results of acceptable accuracy, while the non-linear method will use many iterations and provides results of higher accuracy, but the main disadvantage here is that there is the possibility to find a divergent solution. In this study, it was decided to perform calm water resistance calculations using the linear method of potential flow solver. The suitability of the mesh was analyzed by a grid dependency study, where three different grid resolutions were used by varying the initial mesh size in order to examine; a coarse mesh, a medium mesh and a fine mesh. The computations using medium and fine mesh size required considerable high amount of time, while the computations with the coarse mesh size were significantly faster and provided results of acceptable accuracy. Thus, a coarse mesh density was selected to speed up the evaluation during the optimization studies. The Shipflow environment for the configuration of the computations regarding the ship geometry and dimensions, mesh density and the solver parameters is illustrated in Figure 29.

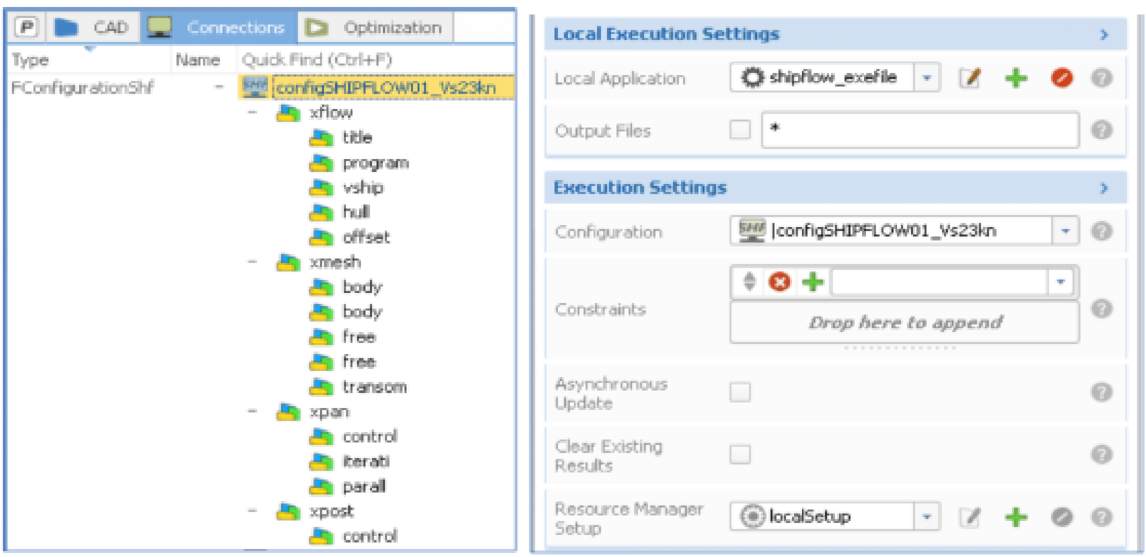

Figure 29: Shipflow configuration in CAESES software.

The wave elevation of a design alternative at scantling draft and operational speed as generated by Shipflow computation is presented in Figure 30.

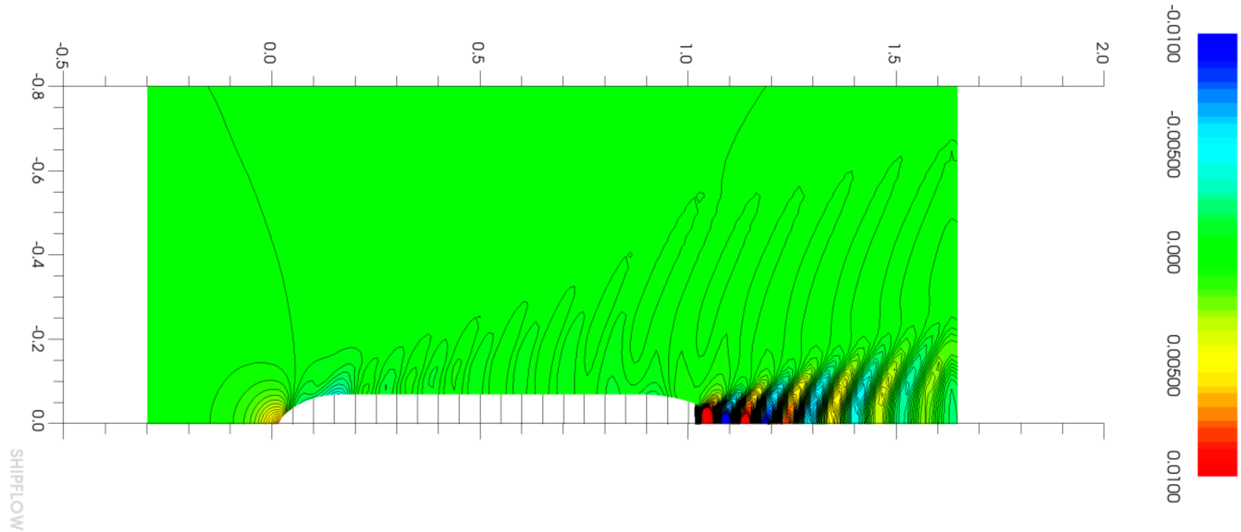

Figure 30: Bulk Carrier vessel wave elevation at scantling draft and operational speed.

The specific configuration using a coarse mesh density and the linear method for the computations was also evaluated for the reference vessel. A validation study was performed using the reference bulk carrier without bulbous bow, which was also imported in CAESES software and was evaluated using Shipflow for specific loading conditions and speed ranges. The results of Shipflow were compared with the data derived by the model tests of the reference vessel. The validation study results for the reference bulk carrier design computed at scantling draft and at a range of speeds are presented in Figure 31.

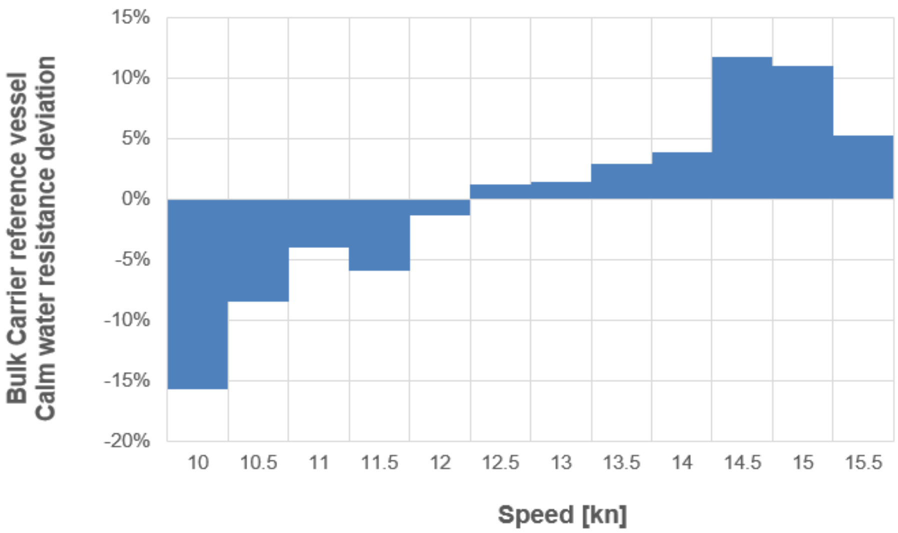

Figure 31: Bulk carrier reference vessel without bulbous bow – Deviation of model tests calm water resistance results in comparison with Shipflow computations at scanting draft.

4.2.3 Optimization studies

The objective of the global optimization study that was formulated and carried out by NTUA was to identify the optimum combination of bulb dimensions for the bulk carrier vessel. A Sobol initialization run considering 300 design alternatives was first performed. The optimization study was carried out by employing the NSGAII algorithm, already integrated in the CAESES environment. The NSGAII parameters are shown in Table 14. The design variables and their range during the optimization study are shown in Table 13. The objective of the study was to minimize the calm water resistance of the bare hull. The partners were interested in obtaining a hull form with superior characteristics in a range of displacements and speeds corresponding to the operational profile. Therefore it was decided to evaluate the calm water resistance of each design alternative at various loading conditions and speeds, considering a weighted average of the calm water resistance using agreed weighting factors, as presented in Table 15.

Table 14: NSGAII genetic algorithm parameters during optimization study.

Parameter	Value
Generations	25
Population size	30
Crossover probability	0.9
Mutation probability	0.01

Table 15: Operational Scenarios for calm water resistance minimization.

Load.Cond	T_M (m)	Trim (m)	Speed (kn)	Weight Coef.
Homog. Light Cargo (0.804t/m^3) departure	14.45	0.0	[11.5, 13.5]	[0.25, 0.35]
Normal ballast at departure	6.35	-3.0	[12.5, 14.75]	[0.2, 0.2]

In the following figures, the results of the optimization study are illustrated. In Figure 32, the objective function for calm water resistance is shown in comparison with bulb length, bulb width and vertical extension of upper and lower part of the bulb. Only the feasible designs are presented in the scatter diagrams. Based on the results, it can be observed that the overall optimum design with the minimum weighted average calm water resistance was obtained via smaller bulb dimensions. A strong dependency between the objective function and the bulb length variable is illustrated. The designs with lower bulb length proved to be more efficient. The same conclusion can be derived from Figure 32, where the impact of the design variable controlling the vertical extension of the lower part of the bulb is also presented. This can be considered as a very interesting result which may indicate that the reference design without bulbous bow could be the best solution based on the selected operational scenarios.

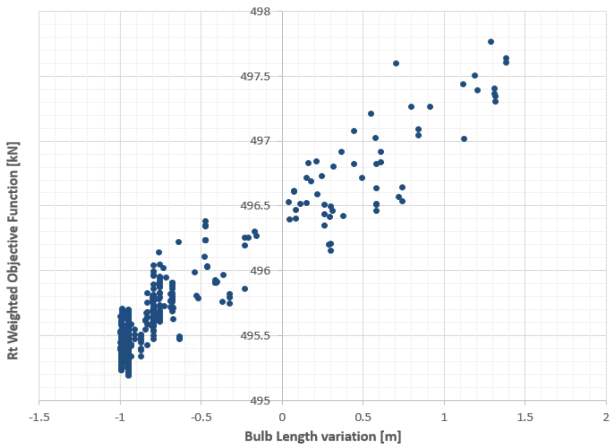

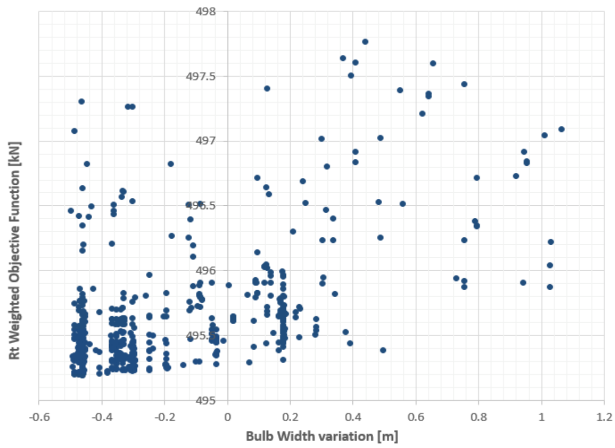

a) Bulb length b) Bulb width

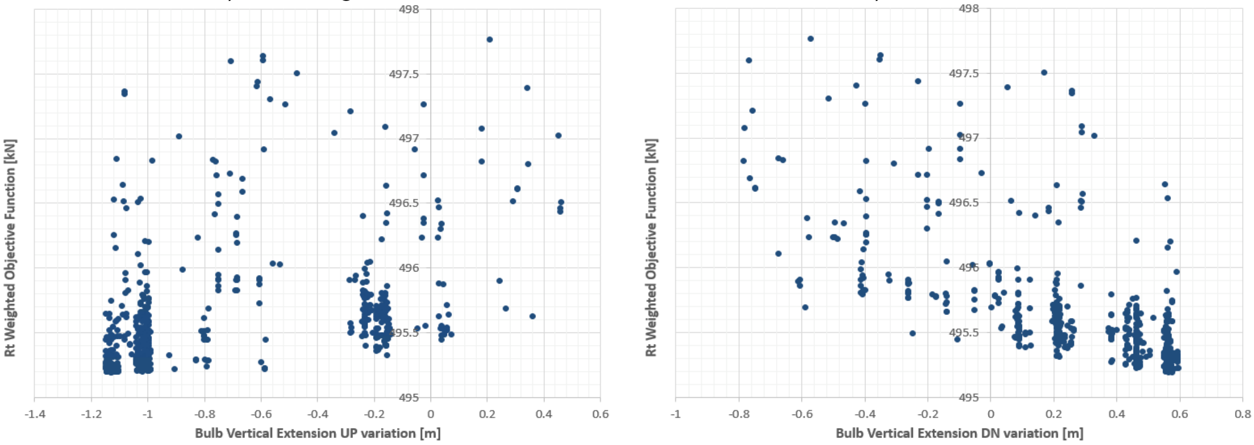

c) Bulb vertical extension of up position d) Bulb vertical extension of down position

Figure 32: Calm water resistance weighted objective function vs variation of design variable.

A validation study was performed for the best designs derived from the optimization using the CFD viscous flow software tool FINE Marine by NUMECA, in order to evaluate the accuracy of the results during the optimization study. In FINE Marine the free-surface viscous flow solver ISIS-CFD (Incompressible Solver for the Interaction of Structures) developed by the EMN (Equipe Modélisation Numérique) is integrated, using the incompressible unsteady Reynolds-averaged Navier Stokes equations (RANSE). The solver is based on the finite volume method to build the spatial discretization of the transport equations. The validation studies were conducted for a set of selected design alternatives using NUMECA FINE Marine CFD tool. The generated mesh as well as the wave elevation for a design alternative at a selected condition are illustrated in Figure 33 and Figure 34.

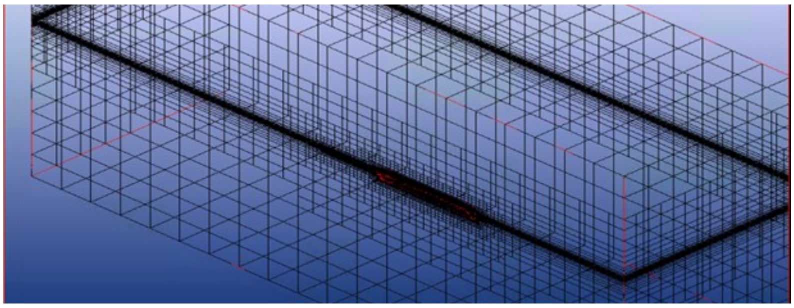

Figure 33: Mesh generation in NUMECA FINE Marine software for a design alternative.

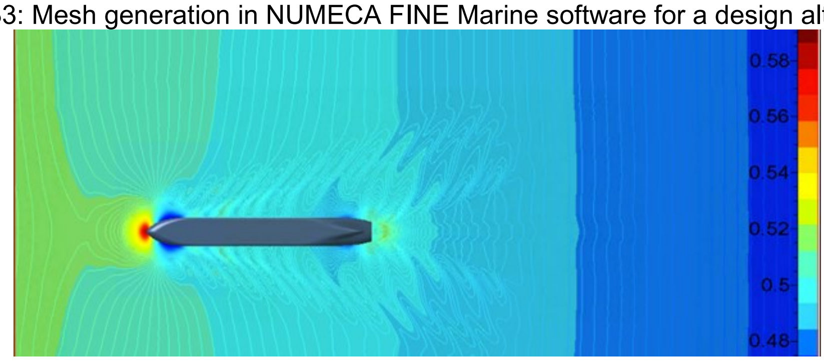

Figure 34: Wave elevation in NUMECA FINE Marine software for a design alternative.

However, the results of the validation study using the CFD tool indicated an inconsistency regarding the ranking of the designs in comparison with the potential flow linear method results. The design alternatives that were examined during the optimization study differ only by small changes in the bow area. Based on the validation study using the CFD FINE Marine software, it was concluded that this kind of hull differences could not be properly computed with significant accuracy using the linear method of potential flow solver. Therefore, it was deemed necessary to repeat the optimization studies and re-evaluate the designs using more refined methods to ensure the accuracy of results. To this end, additional optimization studies were conducted using the non-linear method of potential flow code of Shipflow software. A Sobol initialization run considering 200 design alternatives was initiated. The optimization study was carried out by employing the NSGAII algorithm, using the parameters shown in Table 16. The design variables and their range during the optimization study are shown in Table 13. The objective of the study was to minimize the calm water resistance of the bare hull at the Full Load Departure condition. It was decided to use only one operational scenario, without combinations using various cases and weighted coefficients, due to the higher amount of time required for the calculations using the non-linear method. Therefore, two separate optimization studies were performed using two selected speeds at the Full Load Departure condition, as presented in Table 17.

Table 16: NSGAII genetic algorithm parameters during second part of optimization studies.

Parameter	Value
Generations	20
Population size	20
Crossover probability	0.9
Mutation probability	0.01

Table 17: Operational Scenario considered during second part of optimization studies.

Load Cond.	T_M (m)	Trim (m)	Speed (kn)
Homog. Light Cargo (0.804t/m^3) departure	14.45	0.0	[11.5, 13.5]

In the following figures, the results of the second optimization study are illustrated. In Figure 35 and Figure 36, the calm water resistance is shown in comparison with bulb length, bulb width and vertical extension of upper and lower part of the bulb at the full load departure condition with 11.5kn and 13.5kn speed, respectively. Only the feasible designs are presented in the figures. The trend depicted in the graphs indicated that the best designs with minimum calm water resistance obtain bulb length, width and height values close to the lower limit of the design space. The best designs that were derived from the optimization studies were compared with the reference vessel without the bulbous bow. The resistance values using the potential flow solver were higher than the reference vessel of approximately 1% for 11.5kn and 2.5% for 13.5kn speed. In Figure 37 the calm water resistance in comparison with the immersed volume for the two selected speeds of the optimization studies is illustrated, while with a red mark the reference vessel results are depicted. The corresponding immersed volume presented an increase of approximately 1% in comparison with reference vessel for the same draught. Additional validation studies using NUMECA FINE MARINE CFD software tool were also conducted in order to evaluate the accuracy of the optimization studies results. The validation study also resulted in higher resistance values for the designs with the bulbous bow addition, confirming the final optimization studies using non-linear method of potential flow code of Shipflow software, indicating that the initial design without bulbous bow could provide the best possible solution for the selected operational scenarios.

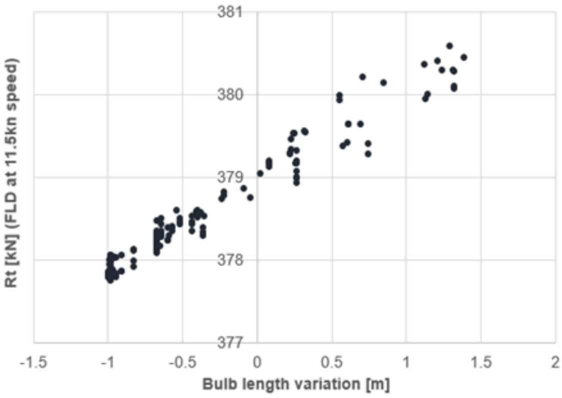

a) Design variable: bulb length

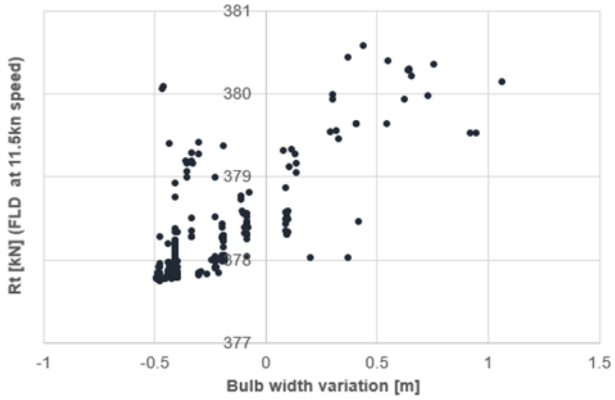

b) Design variable: bulb width

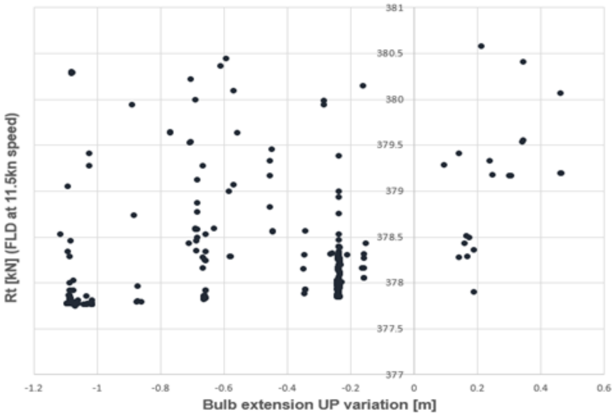

c) Design variable: bulb vertical extension of up position

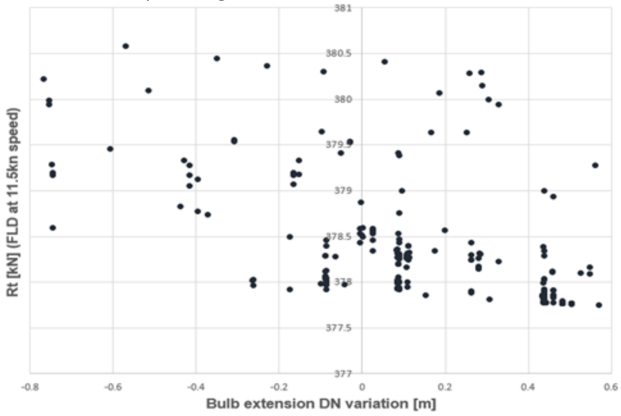

d) Design variable: bulb vertical extension of down position

Figure 35: Calm water resistance objective function results of second optimization study for Full Load Departure (FLD) condition and 11.5kn speed vs variation of design variable.

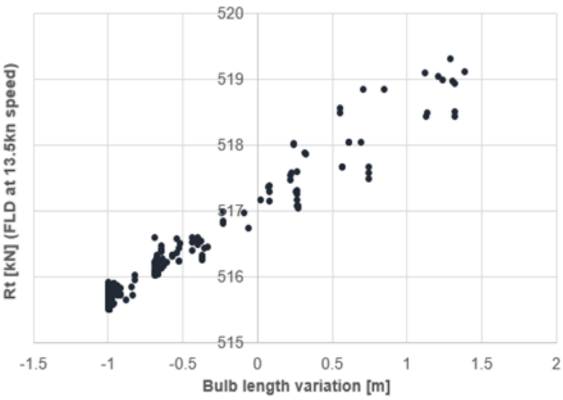

a) Design variable: bulb length

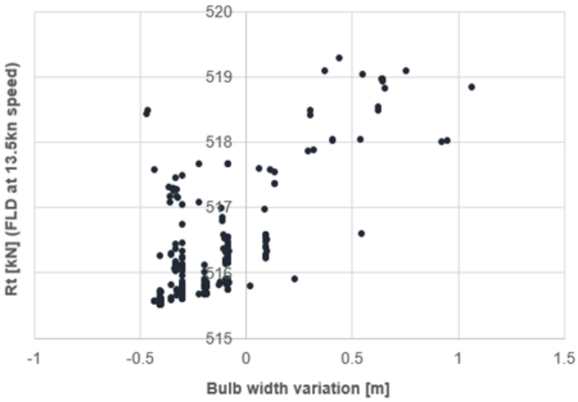

b) Design variable: bulb width

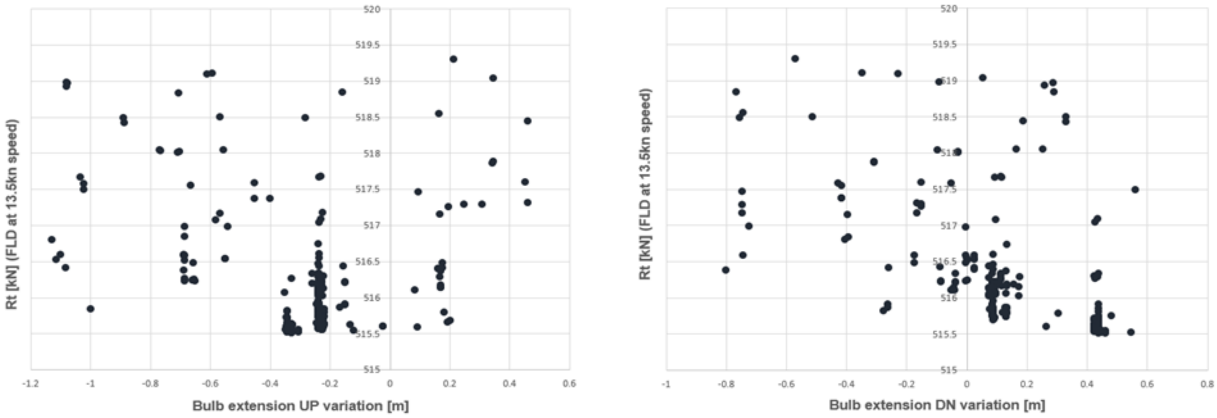

c) Design variable: bulb vertical extension of up position

d) Design variable: bulb vertical extension of down position

Figure 36: Calm water resistance objective function results of second optimization study for Full Load Departure (FLD) condition and 13.5kn speed vs variation of design variable.

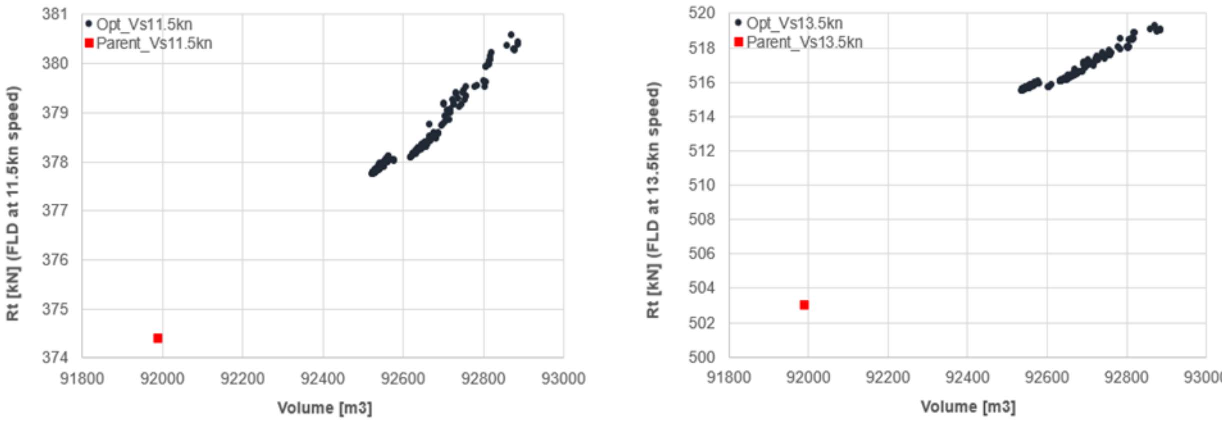

a) Operational condition v=11.5kn

b) Operational condition v=13.5kn

Figure 37: Calm water resistance objective function vs Immersed Volume for Second Optimization study design alternatives and reference Bulk Carrier without bulbous bow.

4.3 Trim Optimization

For the range of operating conditions derived from reported in-service data the influence of draught, trim, and speed have been evaluated and response surface models for use in WP1 been generated. This study has been carried out both for the original hull shape as well as for a reconstruction based on a simplified parametric model to demonstrate a quick workflow to generate reliable input data for the decision support system (see WP1).

4.3.1 Range of operating conditions

From the analysis of reported in service data in WP3 a range of four loading and associated operating conditions covering the majority of service have been derived (see Table 18).

Table 18: Operating conditions as derived from operational data in WP3.

Loading cond.	TM (m) (mean)	TM (m) range	Trim (m) (mean)	Trim (m) range	STW (kn) (mean)	STW Range (Q1 - Q3)	STW, suggested range
1	14.24	[13.5,14.5]	-0.17	[-0.5, 0]	12.24	[11.21,13.41]	[9,15]
2	13.13	[12,13.5]	-0.17	[-0.5, 0]	12.51	[11.81,13.25]	[11,15]
3	6.31	[6, 7]	-2.81	[-3.5, -2]	12.92	[12.04,14.62]	[9,16]
4	8.10	[7.75,8.5]	-2.03	[-3, -1.5]	12.65	[11.55,14.6]	[9,16]

From this table two factors are evident:

1. Mean trim and trim range largely depend on mean draft.
2. The speed through water only shows some very minor variations depending on the load case.

To avoid having separate DoEs and later response surface models a single design space covering all relevant loading and operating conditions has been decided upon for this study:

- TM: [6.3m, 14.45m]
- Trim: [-3.0m, 0.0m]
- STW: [10kts, 15kts]

4.3.2 CFD setup - OpenFOAM

For this study the simulations have been run using a bespoke version of OpenFOAM® with extensions developed to facilitate efficient simulations of large-scale free surface flows [15]. To accelerate the solution all simulations have been run in model scale (l = 0.1) with fixed trim and sinkage.

A split-cartesian hexahedral mesh with a domain size of

- 1 x LPP in front
- 2 x LPP behind
- 2 x LPP aside
- 1.5 x LPP below
- 0.5 x LPP above

Has been used, with dedicated free surface refinement and a typical y^+-value of 90, resulting in mesh sizes of 2.8mio for the bare hull employing a symmetry condition on the centreplane. Turbulence has been modelled using the k-w-SST model with an incident turbulence level of 0.05% and a turbulent viscosity ratio of 0.1. Model to full-scale transformation of the resistance has been computed according to the procedure described in the ITTC ’78 Performance Prediction Method [17]. Examples of mesh and results visualisation are given in Figure 38 and Figure 39.

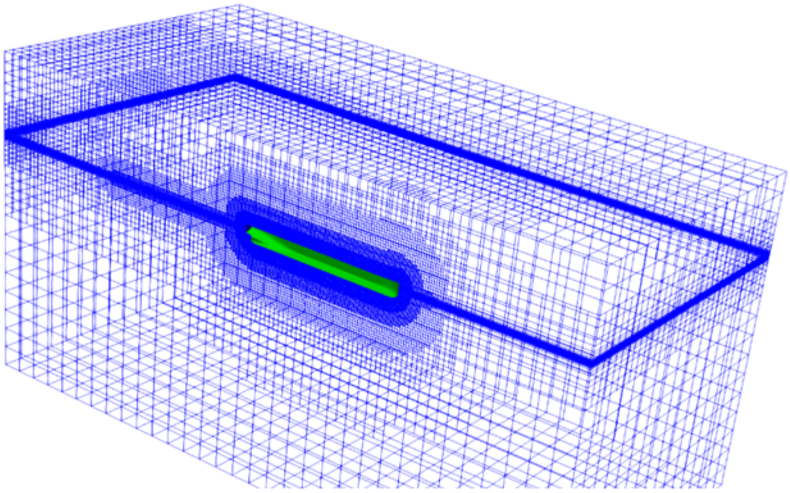

Figure 38: Example of computational mesh used for speed/trim/draught study.

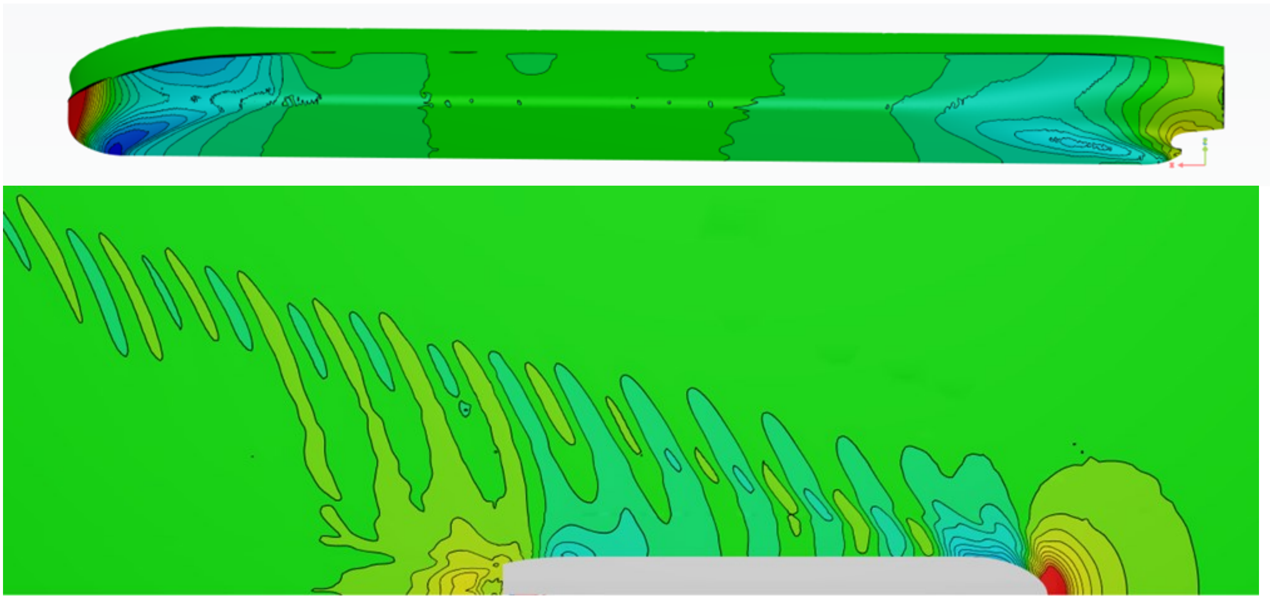

Figure 39: Exemplary visualization of pressure distribution and wave pattern as computed in speed/trim/draught study.

4.3.3 Analysis by Design of Experiment

To evaluate the design space in an efficient manner allowing to create high quality surrogate models a Design of Experiment based on a Sobol distribution with a total of 20 permutations has been set up based on the design space given in Section 4.3.1, see Figure 40. Results of the cases simulated in the DoE for both geometries are given in Figure 41. As can clearly be seen the resistance of the non-optimised rebuilt geometry is always higher by some percentage points.

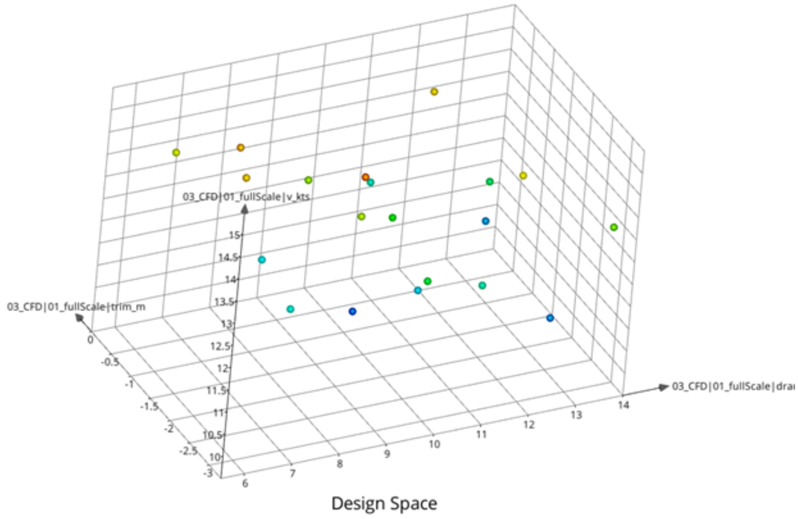

Figure 40: Distribution of permutations in design space.

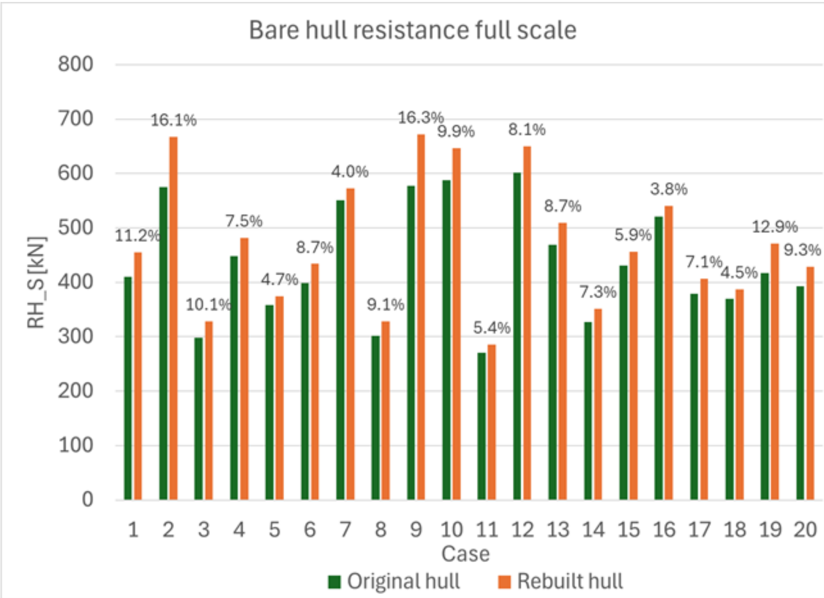

Figure 41: Bare hull resistance for DoE cases, original and rebuilt hull.

4.3.4 CFD setup – Fine/Marine

Supplementary to the work presented previously, SFD created a closed evaluation loop between CAESES and Fine/Marine to evaluate the effect of trim, draught and speed for the studied vessel, M/V Kastor. The study focused on loading conditions LC1 and LC3 of Table 18, which correspond to one laden and one ballast condition. A uniform sampling of the test matrix has been considered for the given ranges of draught and trim, and for three different ship speeds. In total, 30 full scale resistance simulations were performed.

The study considered only half of the domain with symmetry boundary conditions on the symmetry plane to reduce computational cost. The boundary layer is resolved using wall functions and furthermore the ship is able to move heave and pitch directions. The computational setup is based on a sensitivity study which is presented in detail in Section 4.4.1. The Fine grid of the study has been used. The first layer height is set to 0.0075m which results in a mean y+ plus value less than 60. The results of the study are presented in Figure 42.

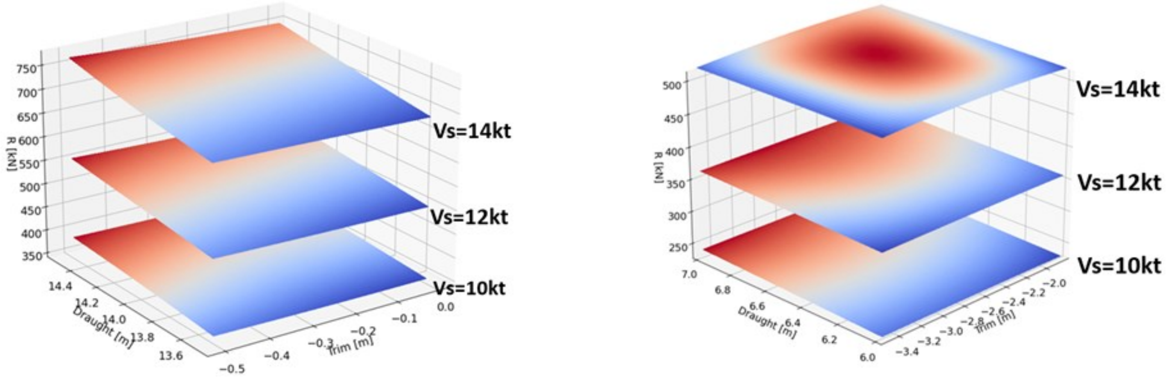

Figure 42: Results of draught, trim and speed sensitivity study for loading conditions LC1-laden (left) and LC3- ballast (right). Results were obtained using Fine/Marine.

Finally, snapshots of the flow which corresponds to laden loading are presented in Figure 43, for T_m=6m, τ=-3.5m, V_s=14kt.

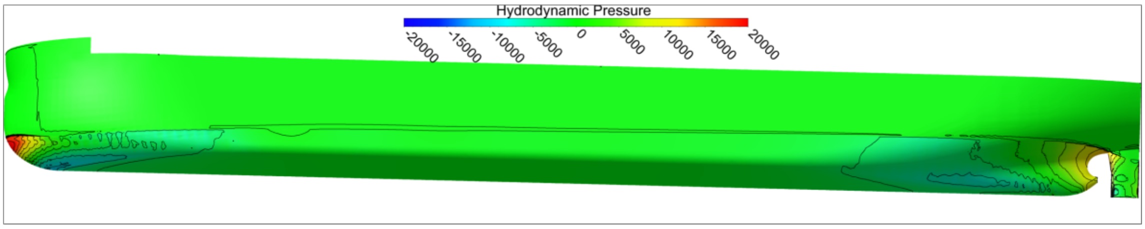

Distribution of hydrodynamic pressure on the surface of the hull.

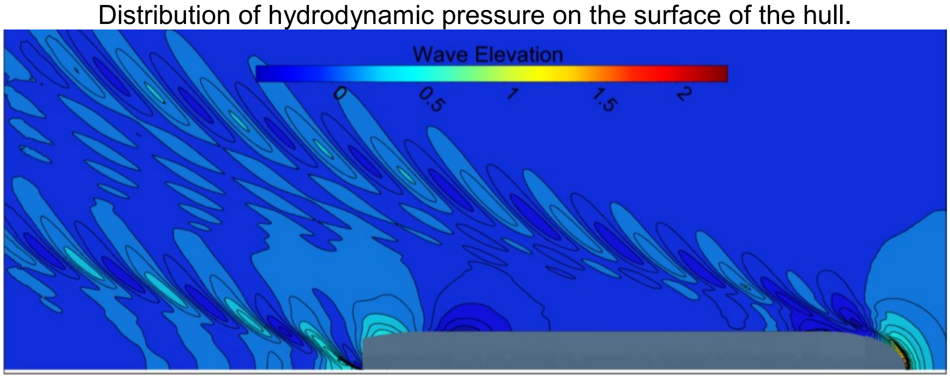

Free surface elevation.

Figure 43: Flow visualization for draught, trim and speed sensitivity study using Fin/Marine.

4.3.5 Response surface modelling

From the results of the DoE as described in Section 4.3.2 response surface models to compute resistance, effective displacement and LCB as function of speed, trim and draught have been generated by a Kriging approach. These models have been resampled to provide structured interpolation tables and provided to WP1.

4.4 Hydrodynamic optimization using Energy Saving Devices

Energy Saving Devices (ESDs) are a cost-effective solution for improving the propulsion efficiency of existing vessels. Various designs have emerged and already have found their way into industrial application. According to their manufacturers, ESDs can significantly optimize fuel efficiency by yielding gains up to 15%, especially in vessels of high block coefficient. They can be classified based on their operating position relative to the propeller [18], as seen in Figure 44Figure 1. Pre-swirl devices operating upstream of the propeller, aim to reduce viscous effects at the stern of the hull and in some cases generate a swirling effect opposite to the propeller rotation. Devices in Zones II and III operate in the wake of the hull and the slipstream of the propeller, respectively, attempting to recover energy that would otherwise be lost. A more detailed overview of the different types of ESDs can be found in [18], [19]. The present study aims to examine and compare four different ESD designs, three positioned upstream of the propeller and one downstream, at the hub of the propeller.

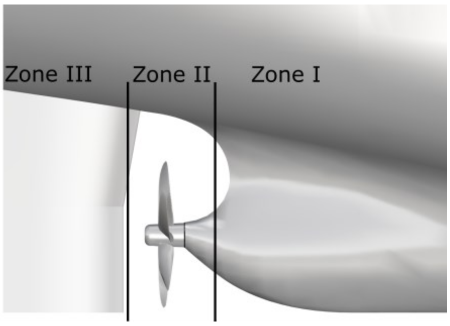

Figure 44: Zones for classification of energy-saving devices [18].

Computational Fluid Dynamics (CFD) play a key role in the design process of an ESD, as it permits full scale assessments. Due to differences in Reynolds numbers, results obtained from experimental model test cannot be easily scaled to full scale. At full scale, the hull boundary layer is thinner, making flow separation more difficult and thereby reducing the potential gains achieved by using an ESD. For this reason, full scale simulations are necessary.

The purpose of this study is not to determine the optimal ESD selection but rather to conduct a preliminary evaluation aimed at:

(a) constructing parametric models that allow easy modification of geometry to examine a range of candidate devices;
(b) utilizing CFD to perform an exploratory study on the working principles of each device;
(c) providing recommendations regarding their suitability with respect to the subject test case vessel.

To this end, SFD and FSYS have developed two parametric models to describe pre-swirl and post-swirl ESDs, respectively. Their performance has been assessed on the M/V Kastor bulk carrier vessel, using self-propulsion simulations with a detailed description of the propeller geometry.

The study is structured as follows: first, the parametric models of the pre- and post-swirl ESDs are presented, as developed within the CAESES software. Next, the CFD setup is described, including a mesh sensitivity study. Finally, the last section discusses the effect of each ESD design based on CFD simulation results and the corresponding flow visualization figures.

Geometry Setup

Parametric models for both pre-swirl and post-swirl ESDs have been developed using the CAESES software [20]. CAESES offers flexible parametric modelling, enabling faster design studies. The following two paragraphs provide a detailed description of the two parametric models developed to optimize the hydrodynamic performance of the bulk carrier M/V Kastor vessel.

Parametric model of pre-swirl ESDs

A single parametric model has been developed within CAESES that can generate designs widely explored by the scientific community and shown to improve the hydrodynamic performance of this type of vessel.

In general, the pre-swirl devices consist of a duct and an additional set of stator fins. An overview of the parameters used to derive the pre-swirl ESD is given in Table 19, with a schematic representation shown in Figure 45.

Table 19: Design parameters for the pre-swirl Energy Saving Devices (ESDs).

Duct		Pre-Swirl Stator	
Parameter	Symbol	Parameter	Symbol
Duct diameter	D	Number of fins	N
Mid-chord length	C	Length	L
Angle of Attack	AoA	Mid-chord length	c
Rake angle in xz-plane	δ_y	Azimuth position	θ
Rake angle in xy-plane	δ_z	Angle of Attack	AoA
Tilt angle	ψ	Rake angle of wing	δ_{wing}

The duct is represented by six parameters, along with a section profile, typically a 4-digit NACA series. The main parameters are the diameter D, the chord of the foil profile C, the angle of attack AoA and a rake angle δ_y defined in the xz-plane. An example of a circular duct is presented in Figure 45a. Additionally, an alternative design can be obtained by adjusting the tilt angle ψ and adding a rake angle δ_z defined in the xy-plane, as shown in see Figure 45b.

The stator fins use also a 4-digit NACA profile section. The rest of the parameters defined are the number of stator fins, the azimuth position θ of each fin, the length L, the chord length C and a sweep angle δ_{wing}.

All parameters are scaled based on the diameter of the propeller D_{prop}, which is an advantage of creating a parametric model. A single design can be adopted and then scaled to match the characteristics of the vessel being examined.

It should be noted that although a detailed optimization study was not conducted, various ducts with different parameters have been examined. In the present report, only the final designs that have a positive effect on ship powering are presented.

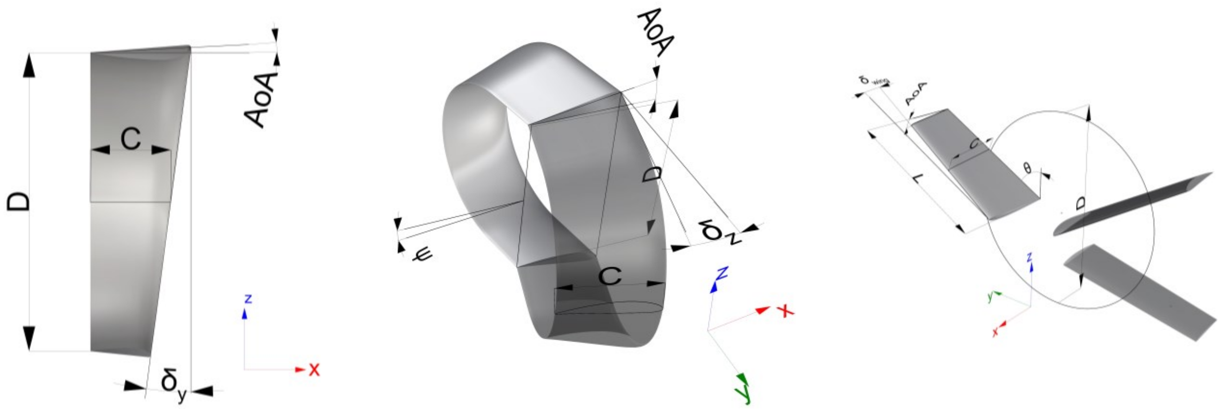

(a) Circular duct (b) Duct with two half rings (c) Pre-swirl stator fins

Figure 45: Parametric model developed to produce a range of pre-swirl ESDs for case (a), (b), and (c).

Three pre-swirl devices have been derived based on this parametric model. The first ESD is a simple circular duct placed along the propeller axis. Its characteristics are given in Table 20. This design is based on the one adopted by the Tokyo 2015 CFD workshop. CFD simulations and experimental tests in *model* scale showed a propulsive gain greater than 6% [21]. The duct functions like a nozzle, accelerating the flow towards the propeller plane and increasing propeller efficiency.

Table 20: Geometry parameters for *circular* duct.

Parameter	Value
Profile	NACA 4420
AoA	20°
C	$0.25D_{prop}$
D	$0.55D_{prop}$

Figure 46 presents the geometry of the circular duct used for computations, as well as its position on the M/V Kastor. Typically, a vertical foiled-shaped supporting strut is placed on the upper plane of the duct. To evaluate the ideal gain achieved by this type of duct, the strut is neglected in this study.

Figure 46: Circular duct fitted on the bulk carrier M/V Kastor.

The second model is a circular duct combined equipped with a pre-swirl stator. The working principle of the pre-swirl stator is similar to counter-rotating propellers, but without the high costs and complexities associated with their driving mechanisms (concentric axes, azipods, etc) [22]. The duct, along with the stator, resembles the case of the Mewis duct [23]. The model used in this study is based on the pre-swirl duct employed in the Ship-scale CFD benchmark study, a workshop organized by the Chalmers University [24]. Both negative and positive effects on power were predicted by the participants, with an average gain of 0.4%.

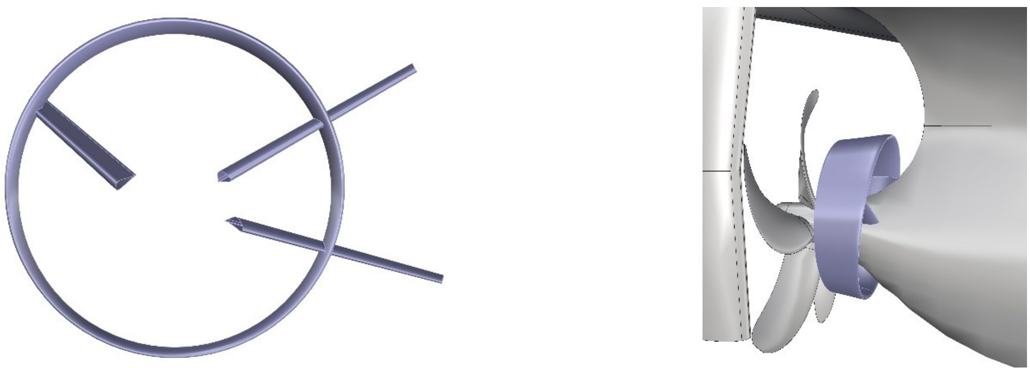

Figure 47: Circular duct equipped with stator fins fitted on the bulk carrier M/V Kastor.

The final design consists of two half rings placed 25% of D_{prop} above the propeller axis. Illustrations of the three studied models and their positions on the M/V Kastor is presented in Figure 46, Figure

47, and Figure 48, while the parameters used for each geometry can be found in Table 20, Table 21 and Table 22.

Table 21: Geometry parameters for *circular* duct with *stator fins.*

Duct		Stator Fin no. 1		Stator Fin no. 2		Stator Fin no.3	
Parameter	Value	Parameter	Value	Parameter	Value	Parameter	Value
Profile	NACA 4412	Profile	NACA 4412	Profile	NACA 4412	Profile	NACA 4412
AoA	5^o	θ*	50^o	θ*	-60^o	θ*	-105^o
C	$0.15D_{prop}$	AoA	12^o	AoA	2^o	AoA	3^o
D	$0.55D_{prop}$	L	$0.95D_{prop}$	L	$0.95D_{prop}$	L	$0.95D_{prop}$
δ_y	6.5	δ_{wing}	5^o	δ_{wing}	5^o	δ_{wing}	5^o

*The azimuth angle is positive at the starboard side and negative at the portside

The last pre-swirl device consists of two half rings, located in front of the upper region of the propeller. This design, along with a set of reacting fins, is similar to the Schneekluth wake equalizing duct [25]. The duct accelerates the flow in the region where the flow is most affected by the presence of the hull and is slower compared to the lower region [26], further reducing flow separation. Table 22 presents the main particulars of the duct and Figure 48 shows its location on the M/V Kastor.

Table 22: Geometry parameters for a duct with two half rings.

Parameter	Value
Profile	NACA 4412
AoA	10^o
C	$0.2D_{prop}$
D	$0.5D_{prop}$
δ_z	12^o
ψ	6^o

Figure 48: Duct with two half-rings fitted on the bulk carrier M/V Kastor.

Parametric model of post-swirl ESDs

The post-swirl ESD in this case is a PBCF (Propeller Boss Cap Fins), an energy-saving device attached to the propeller of a vessel. It breaks up the hub vortex generated behind the rotating propeller and enhances propeller efficiency [27]. The PBCF rotates together with the propeller. The number of PBCF blades is always equal to the number of blades on the attached propeller, as shown in Figure 49 and Figure 50. A NACA 66 profile with a camber line of a = 0.8 mod is used, which is typical in propeller design. The diameter of the PBCF is 1870 mm, and the arc length distance between the trailing edge (TE) of the propeller and the leading edge (LE) of the PBCF should be 246 mm, based on the blueprint design, as shown in Figure 49.

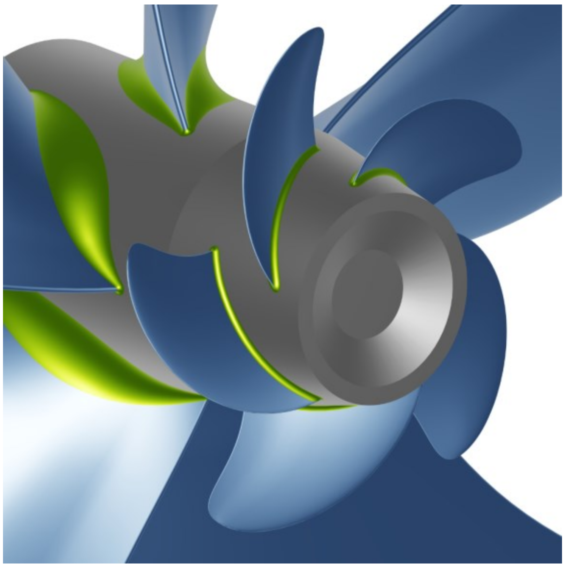

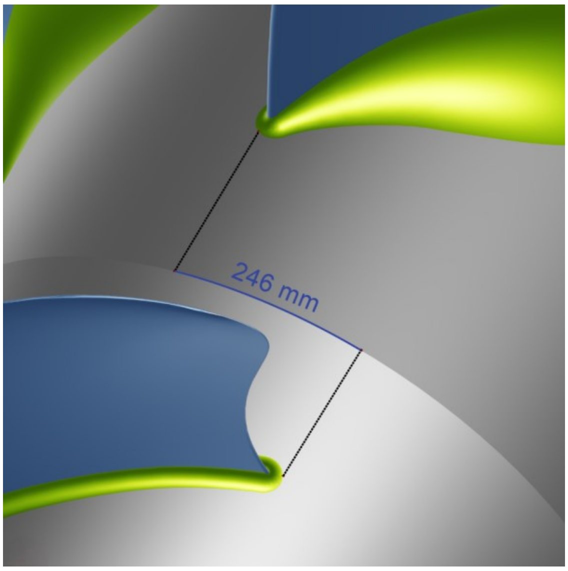

Figure 49: PBCF model of the bulk carrier M/V Kastor.

The parametric model of the PBCF has been developed within CAESES 5.3, incorporating a new propeller workflow. This simplifies the process of developing a parametric propeller model by providing a straightforward, step-by-step approach (see Figure 50). The modeling of the PBCF is similar to that of a propeller.

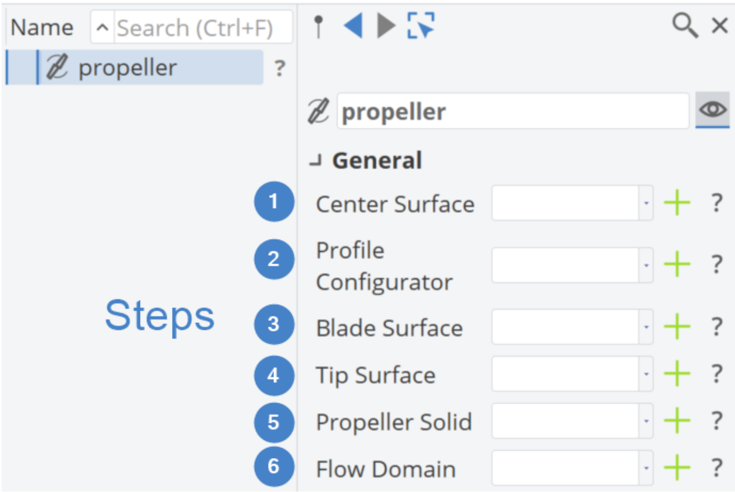

Figure 50: Propeller workflow GUI in CAESES 5.3.

In Figure 51, six parameters of the PBCF parametric model are shown, along with their corresponding radial distributions, including chord, rake, skew, pitch, camber and thickness of the profile. Each of these parameters corresponds to a different radial distribution.

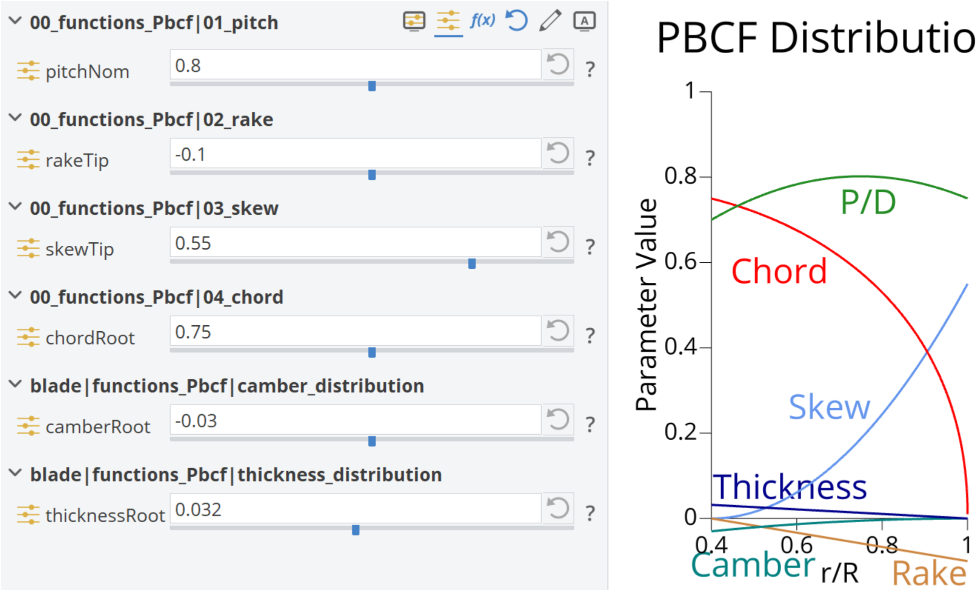

Figure 51: PBCF radial distributions of the bulk carrier M/V Kastor.

Parametric model of Propeller

Similarly to PBCF, a parametric model for the propeller of the bulk carrier M/V *Kastor* was developed. Below are the radial distributions of the parametric model. Figure 52 shows the propeller attached to the PBCF.

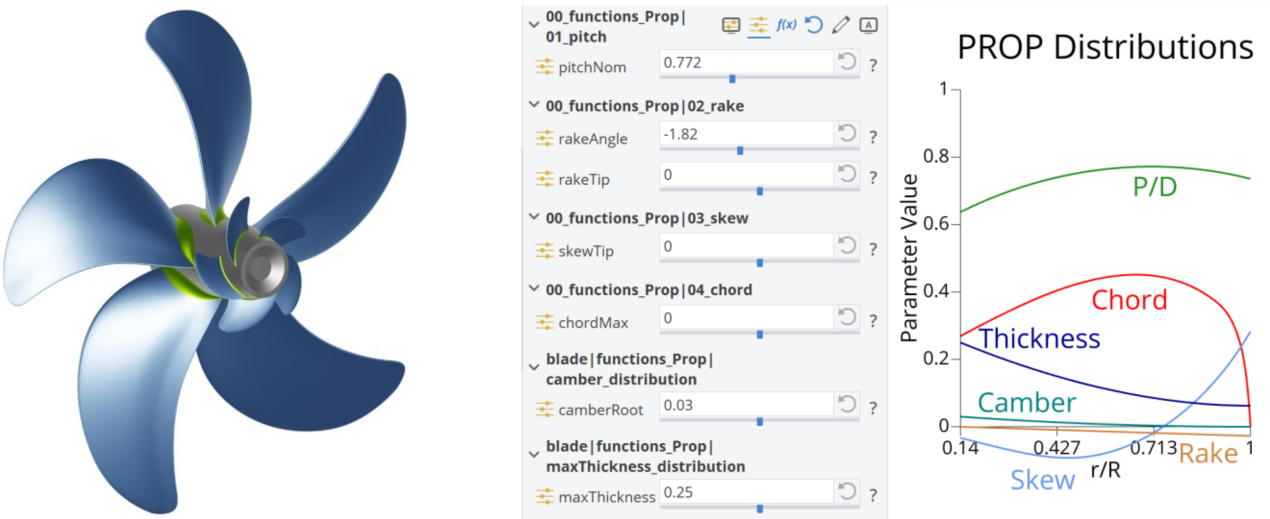

Figure 52: Propeller & PBCF model of the bulk carrier M/V Kastor.

Open Water Characteristics

Open water tests were conducted using the panel code panMARE from TUHH [28], with cavitation effects included for the preliminary study. The advance coefficient (J) ranged from 0.35 to 0.75, with tests performed at a constant speed while varying RPM. Under baseline conditions, the vessel operated at a speed of 13.5 knots, a revolution rate of 84 RPM and an advance coefficient of J = 0.714, as illustrated in Figure 53.

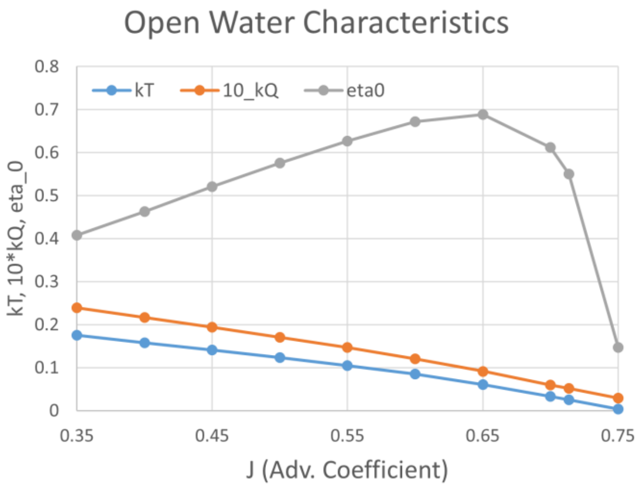

Figure 53: Open water diagram.

4.4.1 Computational Setup

SFD conducted propulsion performance predictions entirely based on Computational Fluid Dynamics (CFD), which allows for the inclusion of all relevant flow characteristics. For all self-propulsion simulations, the commercial software package Numeca FINE/Marine v.11.2 is used. Numeca's FINE/Marine employs steady and unsteady RANS equations to calculate the turbulent flow around the ship. Turbulence is modelled using Boussinesq hypothesis with Menter's two-equation k-ω SST model [26]. Simulations follow a multiphase simulation approach, where the free surface between air and water is modeled using the Volume-of-Fluid (VOF) method [29] method. The flow is solved in the relative frame with absolute velocity formulation. Convective fluxes are obtained using blending schemes, namely AVLSMART [30] for momentum and turbulence equations, and the BRICS [31] scheme for the VOF equation.

Domain Size and Boundary Conditions

The size of the domain is large enough to ensure that no reflection occurs at the farfield boundaries. In Figure 54 the dimensions of the computational domain used can be seen. The size of the domain in the x-direction is 6.5 times L_{pp}, in the y-direction is 4.5 times L_{pp} and in the z-direction is 3.5 times L_{pp}.

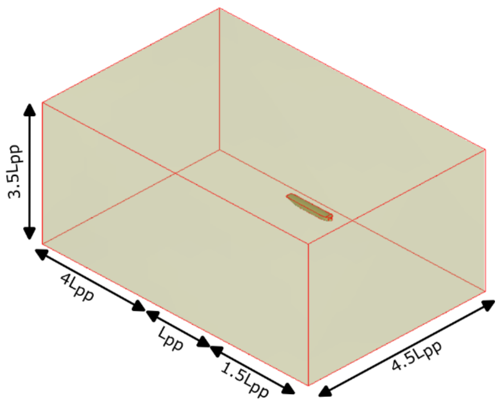

Figure 54: Dimensions of the domain used for self-propulsion simulations

All external boundaries are set as far field, except for the top and bottom boundaries of the fluid domain which are set to prescribed pressure boundary condition to account for the hydrostatic component of the pressure field. Solid boundaries such as the ship, appendages and the propeller patches are defined as no slip conditions with wall functions to solve the viscous sublayer. Solid patches which have no hydrodynamic interaction (e.g. the deck of the ship) are treated as slip walls so that they contribute less to the forces analysis.

Overall, the boundary conditions for the simulation are defined as follows:

- Inlet: Farfield
- Outlet: Farfield
- Portside: Farfield
- Starboard: Farfield
- Hull, Rudder, Propeller: Wall Functions
- Deck: Slip Boundary Conditions
- Top: Prescribed Pressure
- Bottom: Prescribed Pressure

The imposed variables at the farfield boundaries depend on the local flow direction relative to the boundary patch: the flow either enters or leaves the domain. Consequently, Dirichlet or Neumann conditions are applied. The code used by the software automatically adapts the condition to the correct situation depending on the sign of the local velocity field.

Domain Discretization

For all RANS simulations, unstructured, hexa-dominant meshes are used, generated with the Numeca HEXPRESS software. The ship domain mesh is especially refined in the following areas:

- Ship Appendages
- Regions with High Pressure Gradients (bow, stern, and free surface)
- Wake of the Ship (inflow to the propeller domain)

Some of these refinements are applied only on the surface, while others, such as those for the free surface and wake, involve volumetric refinements of cells. To accurately capture the viscous forces correctly, boundary layers are applied to all underwater wall surfaces.

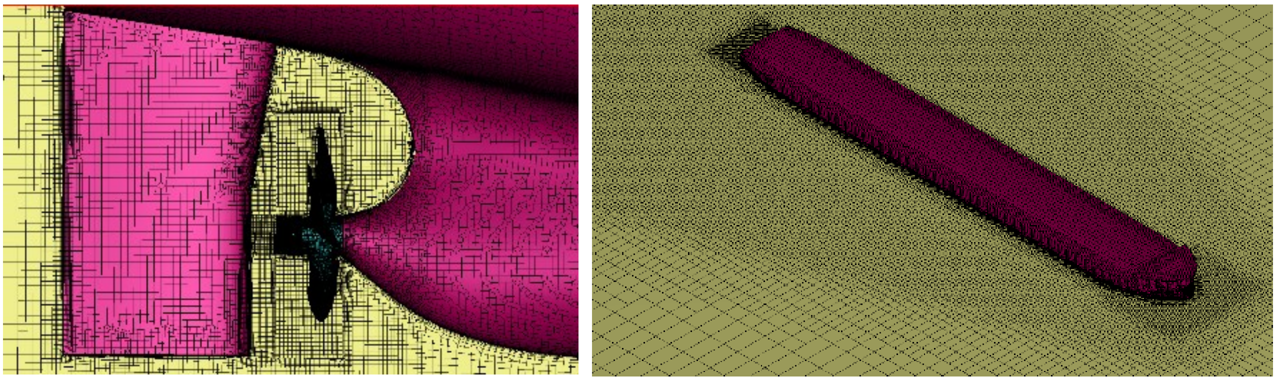

Figure 55: Computational grid used for the evaluation of ESDs.

Due to the use of wall functions, a dimensionless wall distance of y^+ averaging between 30 and 100 is applied to the surfaces. The prismatic boundary layer cells smoothly merge into the volume mesh. All geometric representations of bodies in the fluid domain are checked for consistency, manifoldness, and knuckles. Further checks are made for known edges (e.g transoms, shaft brackets, rudder edges). The overall mesh size and refinement are continuously monitored with respect to the convergence of the results and grid dependent errors. The mesh setup for the current project is shown in Figure 55, specifically at the left the mesh on the mirror plane is shown, along with the surface mesh on the propeller and on the hull, while at the right the mesh at free surface can be seen.

Simulation Description

A constant ship speed self-propulsion simulation is performed. The vessel moves at a prescribed velocity, and a PI controller is used to calculate the rotation rate (rpm) of the propeller to match the ship's resistance with the thrust generated by the propeller. It is important to note that, in order to avoid undesirable transient phenomena caused by inertia forces, a half-sinus ramping function is applied to smoothly accelerate the vessel to its final velocity. Regarding the ship's motion in the other degrees of freedom, the vessel is free to move in the z-direction (heave) and rotate around the y-axis (pitch), while motion in other directions is fixed.

Self-propulsion calculations simulations are completed in two steps. First, a simulation is performed using the Multiple Reference Frame (MRF) approximation to account for the rotation of the propeller. This simulation uses a large timestep to estimate the hydrodynamic characteristics of the field, including forces acting on the propeller and hull, as well as trim and sinkage of the vessel. The timestep is calculated using the following formula:

$$dt_1 = \left(\frac{RPM_{prop}}{60}\right)^{-1} \Big/ 20 \tag{4.16}$$

Afterwards, a second, restarted simulation is performed where the propeller rotation is resolved by applying the sliding grid method. The timestep is defined in such a way that the propeller rotates at most 2 degrees, as recommended by the ITTC guidelines [33]). It is calculated using the following formula:

$$dt_2 = \left(\frac{RPM_{prop}}{60}\right)^{-1} \Big/ 200 \tag{4.17}$$

Since the rpm of the propeller is unknown, trial simulations are conducted to estimate the propeller's rpm. The final values of the time steps are small enough to ensure that the previous time step definitions are valid.

Grid Convergence Study

A verification study was conducted to assess the uncertainty of the numerical calculations using the Grid Convergence Index (GCI) [34], based on the Richardson extrapolation method and recommended by ITTC [33]. Numerical results were obtained using three sets of grid resolution (i.e., fine, medium and coarse) to determine the uncertainty level of the numerical calculations. In this technique, the refinement factor was selected to be greater than 1.3. The delivered power was used to evaluate the uncertainty of the numerical solution. The assessment was done at the Scantling draft and 13.5 knots condition. The difference between the solution scalars (ε_{ij}) was computed using the following equation:

$$\varepsilon_{21} = \varphi_2 - \varphi_1 \qquad \varepsilon_{32} = \varphi_3 - \varphi_2 \tag{4.18}$$

where φ_1, φ_2, φ_3 represent the numerical results for fine, medium and coarse grid resolutions, respectively. The convergence condition of the numerical solution can be determined using the following formulation:

$$R = {}^{\varepsilon_{21}}/_{\varepsilon_{32}} \tag{4.19}$$

The determination of the solution can be assessed based on the range of R values:

- -1< R <0, oscillatory convergence
- 0< R <1, monotonic convergence
- R <-1, oscillatory divergence
- R >1, monotonic divergence

The extrapolated value can be calculated using the following equation:

$$\varphi_{ext}^{21} = \frac{r_{21}^{p}\varphi_1 - \varphi_2}{r_{21}^{p} - 1} \tag{4.20}$$

Similarly, the extrapolated relative error was given by:

$$e_{ext}^{21} = \left|\frac{\varphi_{ext}^{21} - \varphi_1}{\varphi_{ext}^{21}}\right| \tag{4.21}$$

While the approximate relative error was computed as follows:

$$e_a^{21} = \left|\frac{\varphi_1 - \varphi_2}{\varphi_1}\right| \tag{4.22}$$

As a result, the uncertainty of the numerical solution can be calculated as:

$$GCI_{fine}^{21} = \left|\frac{1.25 e_a^{21}}{r_{21}^{p} - 1}\right| \tag{4.23}$$

The results of the grid sensitivity study are given in Table 23. Due to limited computational resources and the large number of candidates ESDs, the medium mesh was selected to evaluate the performance of ESDs.

Table 23: Grid Convergence Study. N_i the total number of cells in the i[th] grid, φ_ι is the propeller power predicted by the i[th] grid.

Grid Type	Element Count
Coarse - N3	2,779,584
Medium - N2	6,389,568
Fine - N1	14,629,145

φ_3 [kW]	8453.7
φ_2 [kW]	7401.8
φ_1 [kW]	7080.5
R	0.31
GCI_{fine}^{21} [%]	3.30

r_{32}	1.32
r_{21}	1.32
p	4.04
ε_{21}	321.30
ε_{32}	1051.9
e_a^{21}	0.045
φ_{ext}^{21}	6893.6
e_{ext}^{21}	0.074

In Figure 56 the convergence of propeller power is presented for the three studied grids. Similar characteristics are observed for all three grids.

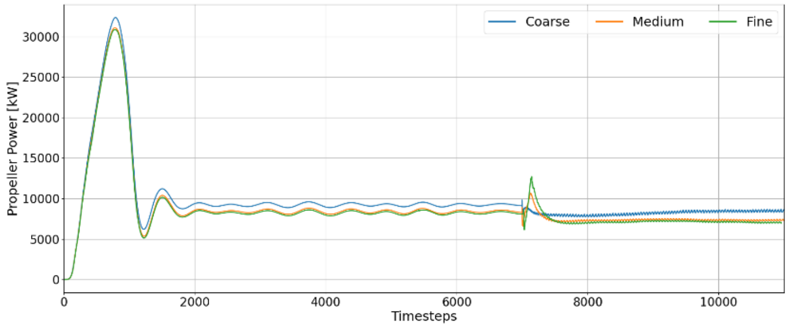

Figure 56: Results of grid convergence study. Propeller power for the three studied grids at scantling draft T_{sc}=14.45m for vessel speed V_s=13.5kt.

Furthermore, the wave elevation is presented in Figure 57 for the three grids. The coarse grid shows excessive smearing of the free surface waves while similar wave fields are observed for the two finer grids. The simulation conditions were scantling draft T_{sc}=14.45m, vessel speed V_s=13.5kt..

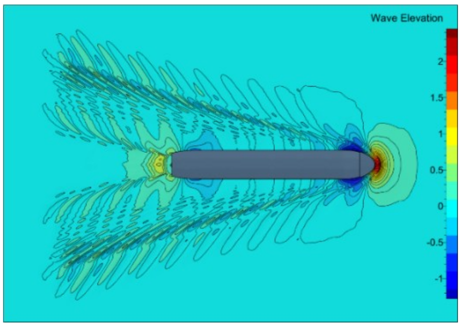

Fine

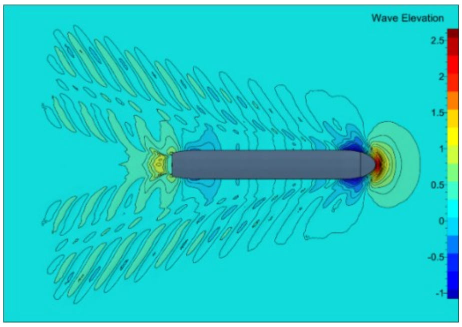

Medium

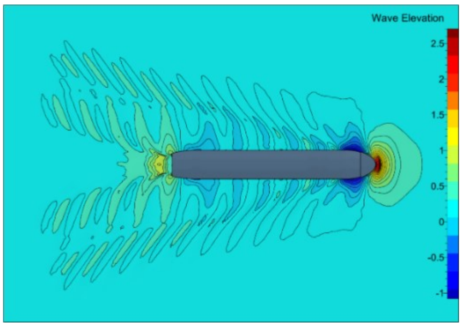

Coarse

Figure 57: Results of grid convergence study. Free surface elevation for the three studied grids.

Lastly, to provide a better insight into the hydrodynamic characteristics of the field, three additional contour plots are presented for the *Medium* mesh for the same simulation conditions.

First, in Figure 58 the wave elevation on the surface of the hull is shown.

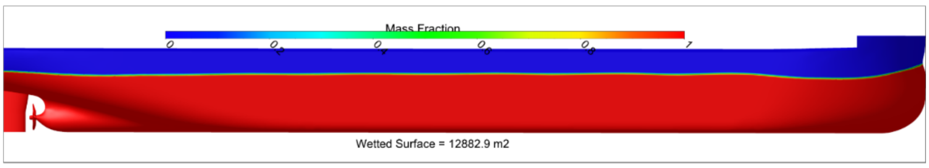

Figure 58: Wave elevation on the surface of the hull and wetted surface.

As seen, the VoF reconstruction scheme, along with the mesh refinement near the free surface, captures the density discontinuity quite well.

Additionally, Figure 59 presents the distribution of y^+ on the surface of the hull. The first cell of the viscous layer is placed 1mm away from the hull, leading to y^+ values below 300. This ensures that the first layer is inside the logarithmic area of the turbulent boundary layer, allowing for accurate resolution of the viscous phenomena.

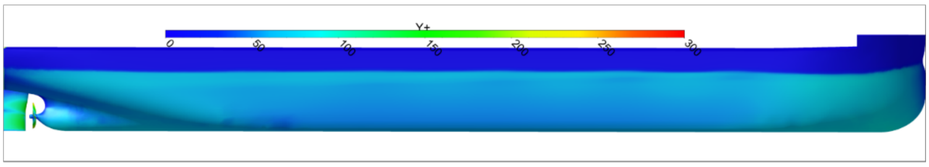

Figure 59: Y+ distribution on the surface of the hull.

Lastly, the hydrodynamic component of pressure is presented in Figure 60. The mesh resolves the large pressure gradients on the bow and in the aft of the ship.

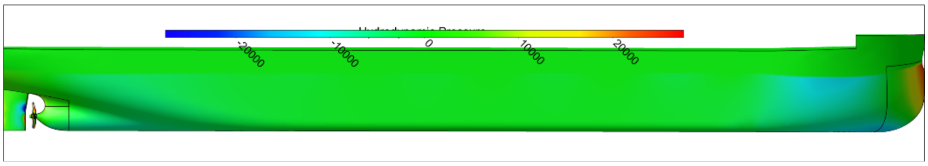

Figure 60: Hydrodynamic pressure on the surface of the hull.

4.4.2 Results

Prior to presenting the results obtained for the various ESD candidates it is useful to assess the hydrodynamic behaviour of the vessel without ESDs. To this end, three self-propulsion simulations were carried out for different vessel speeds. The results of the simulations can be found in Table 24. All simulations and comparisons were carried out in the scantling condition of the vessel (T_{sc}=14.45m) and vessel speed V_s=13.5kt.

Table 24: Results of self-propulsion simulations for the bulk carrier type vessel, for three different speeds.

Vessel Ship [kt]	Ship Res. [kN]	Prop. Torque [kNm]	Prop. RPM	Prop. Power (mean) [kW]
12.0	802.06	659.09	74.3	5129.72
13.5	996.52	842.41	83.9	7397.17
14.5	1151.39	992.97	90.8	9437.93

Furthermore, towing resistance simulations are particularly useful for assessing the benefit of installing pre-swirl ESD. In Figure 61, three contours used to visualize the flow at the aft part of the ship are presented for vessel speed V_s=13.5kt. Starting from Figure 61a, a high pressure region is noted, as expected, at the aft part of the ship. In addition, in Figure 61b, the friction coefficient and streamlines on the surface of the hull are depicted. The figure indicates that no separation bubbles are formed upstream of the propeller, and the flow remains attached to the ship's hull. This is further confirmed in Figure 61c. The velocity deficit on the disk upstream of the propeller can be used to calculate the wake fraction coefficient. The wake fraction is given by:

$$w = \frac{V_s - \check{V}}{V_s} \tag{4.24}$$

where $\check{V}$ is the average water entering the disk. For this case, the wake fraction is calculated to be 0.274. According to IMO [35], the recommended value for wake fraction-w for vessels with block coefficient c_b higher than 0.8 is 0.35. The low value of w, in addition to the aligned streamlines at the aft part of the ship, suggests that small gains can be achieved by retrofitting the vessel with pre-swirl ESDs.

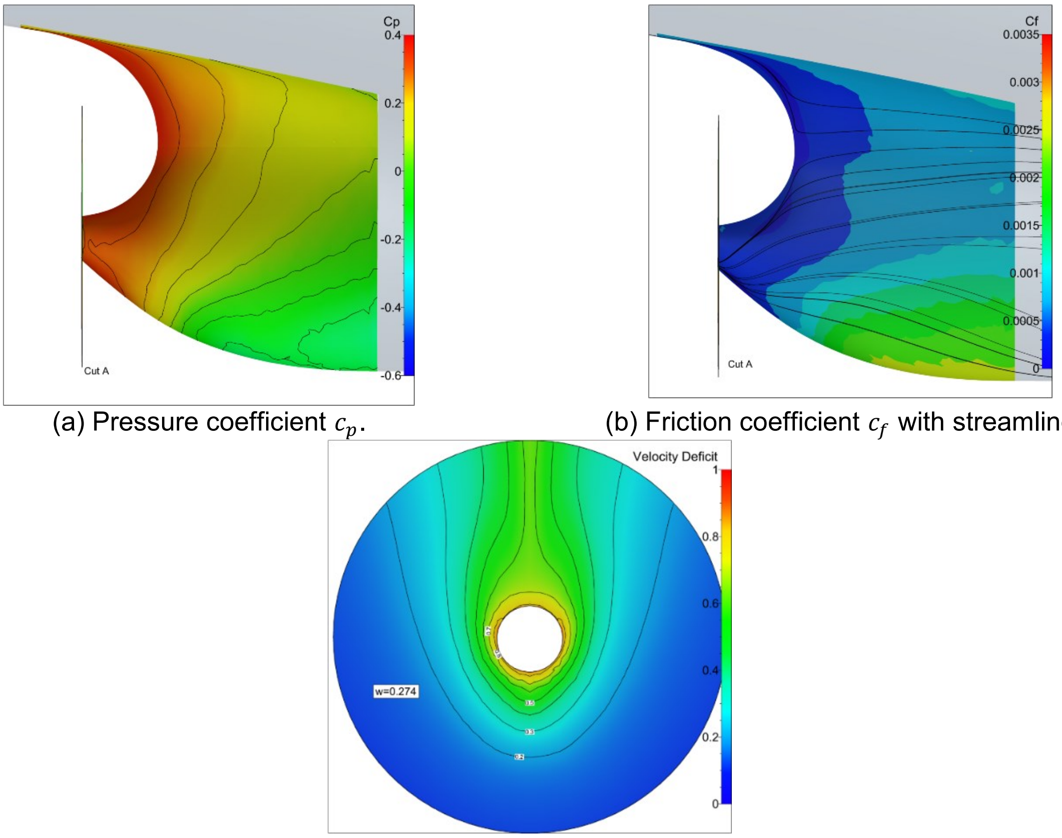

(a) Pressure coefficient c_p.
(b) Friction coefficient c_f with streamlines.
(c) Velocity deficit at Cut A (see figures (a) and (b)) while the wake fraction (w) is also noted.
Figure 61: Flow visualization of resistance calculations for the bulk carrier type vessel without ESDs.

The next paragraphs focus on the effect of the candidate ESDs on ship powering. Table 26 summarizes the results for the five cases examined here: the reference case without ESDs, three cases with the corresponding pre-swirl devices and the case with the Hub Vortex Fin. A small improvement of approximately 2% is achieved by all pre-swirl devices, while the post-swirl device produces negligible benefits.

Table 25: Comparison of results between the reference case and the four candidate ESDs

	Ship Res. [kN]	Prop. Torque [kNm]	Prop. RPM	Prop. Power (mean) [kW]	ESD Gain/Loss [%]
Ref.	995.97	842.03	83.9	7397.17	-
Circular	994.74	841.65	82.5	7275.30	+1.65%
Duct with fins	1000.66	842.37	82.2	7248.64	+2.01%
Duct with half-rings	980.31	830.81	83.3	7255.40	+2.08%
Hub Vortex Fins	992.22	836.74	84.3	7390.78	0.10%

Pre-Swirl ESDs

Starting the discussion of the results from the pre-swirl devices. The following figures aim to provide a better insight about the effect of each pre-swirl ESD.

Firstly, Figure 62 presents the pressure coefficient C_p for the reference case and the three candidate pre-swirl ESDs. In the reference case, without ESDs, a high-pressure region, and thus low fluid velocity is observed at the upper aft part of the ship. The purpose of the ESDs is to redirect energy to this region by reorienting the flow towards the propeller disk.

All candidate ESDs successfully reduce the pressure in this region through suction, while the ESDs equipped with circular duct (see Figure 62b and Figure 62c) further reduce the pressure at the lower aft part. As will be discussed further, this effect has a negative impact on the performance of the propeller. Lastly, the duct with the half-rings reduces pressure only at the upper aft part of the ship without affecting the flow anywhere else.

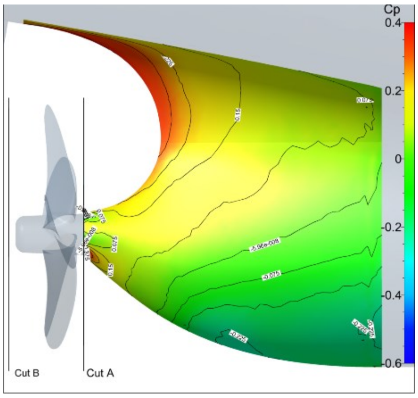

(a) Reference case without ESDs.

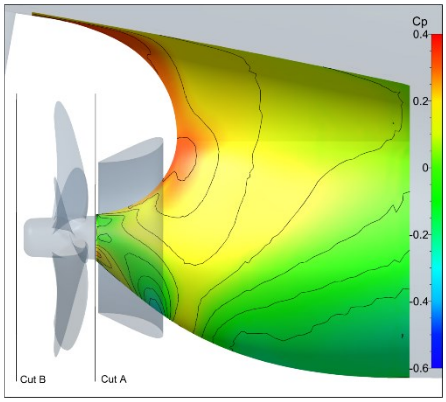

(b) Circular duct.

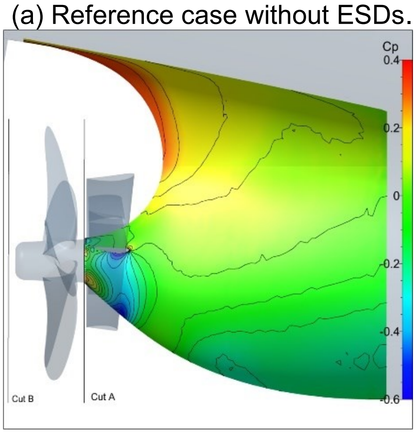

(c) Duct equipped with fins.

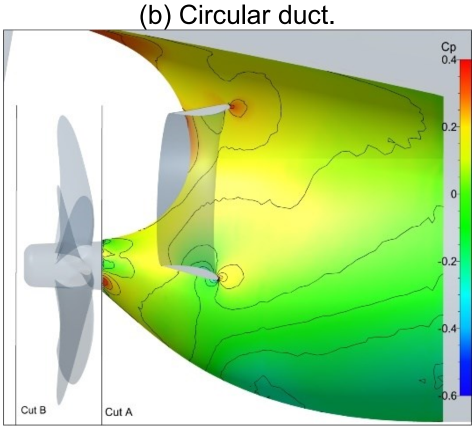

(d) Duct with half-rings.

Figure 62: Pressure coefficient c_p contour for (a), (b), (c), and (d) configurations.

Figure 63 presents the friction coefficient along with the streamlines on the surface of the hull. In all cases with pre-swirl ESDs, increased friction is observed at the aft part due to flow acceleration. Regions of high friction are noted at the lower aft part in case of circular ducts (Figure 62b and Figure 62c).The streamlines in the reference case, without ESD (see Figure 63a) indicate that flow is directed to the lower part of the propeller disk leading to an unequal distribution. This effect is further pronounced in the case of the circular duct (Figure 63a). The other two devices seem to mitigate it, leading to a more uniform flow distribution on the propeller disk. This is especially noticed in case of the pre-swirl device with fins. The pre-swirl effect of the stator fins causes the flow to move directly into the propeller plane.

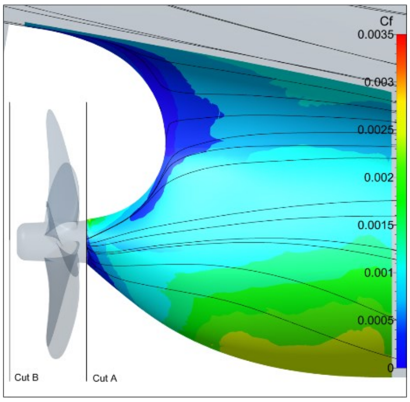

(a) Reference case without ESDs.

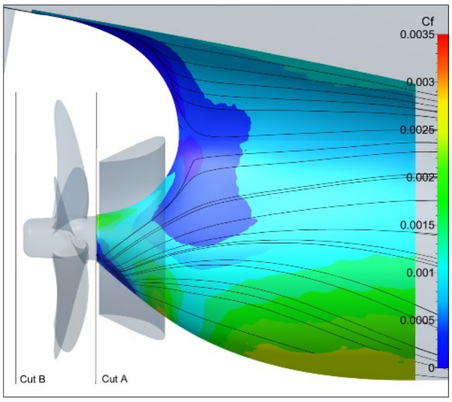

(b) Circular duct.

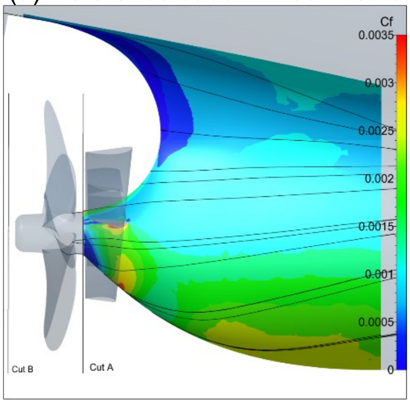

(c) Duct equipped with fins.

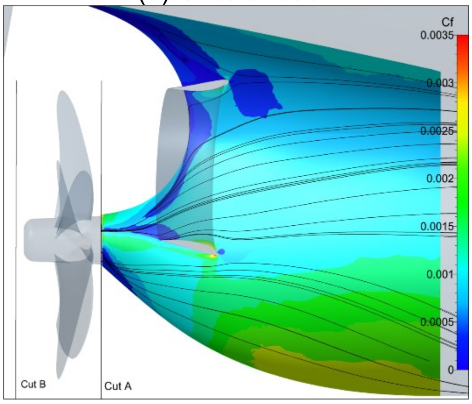

(d) Duct with half-rings.

Figure 63: Friction coefficient c_f contour along with streamlines for (a), (b), (c), and (d) configurations.

It is important to examine the effect of each ESD on the propeller inflow. Figure 64 presents the axial velocity component in the form of the velocity deficit. Values greater than one indicate that the flow is opposite to the freestream velocity, values between zero and one indicate that the velocity is lower than the freestream velocity and values lower than zero is an indication that the flow is accelerated in the direction of the freestream velocity.

In case of the circular duct (Figure 64b) regions of low velocity are observed due to the viscous boundary layer of the duct. This is also seen in the second candidate ESD, equipped with stator fins (Figure 64c). Although, the stator accelerates the flow in the upper the part of the disk, significant regions of flow recirculation are observed, particularly at the intersection points of the duct with the portside fins and at the lower part of the duct. Although the separation bubbles at the corners of the ESD appear to be an inherent effect of the device, lower separation could be avoided with an ellipsoid design, similar to a Mewis duct. This would retain the advantages of the duct and stator fins, while reducing the negative effects of increased skin friction and flow separation. Lastly, the duct with half-rings (Figure 64d) seems to have the most beneficial effect to the propeller inflow, accelerating the flow at the upper part of the disk without causing separation bubbles or significant shadowing effects due to its wake.

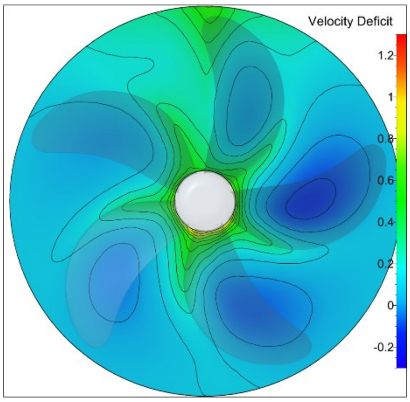

(a) Reference case without ESDs.

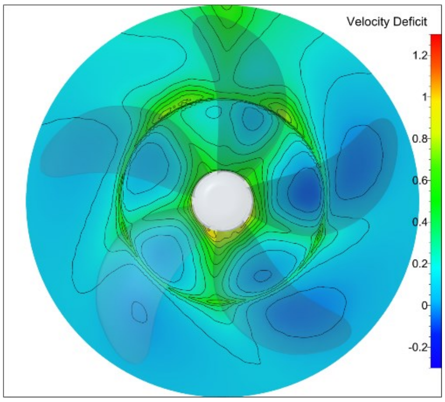

(b) Circular duct.

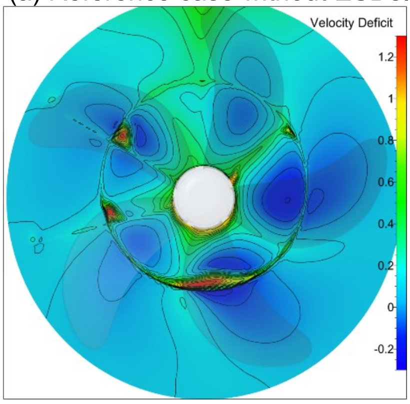

(c) Duct equipped with fins.

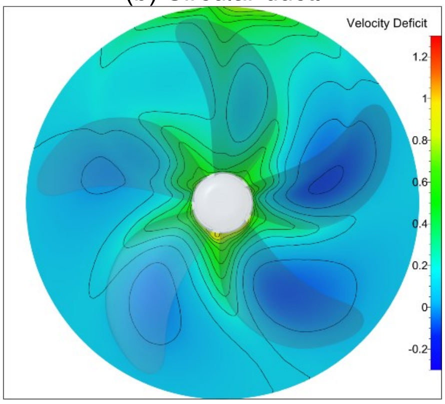

(d) Duct with half-rings.

Figure 64: Velocity deficit contour at Cut A for (a), (b), (c), and (d) configurations.

Table 26 presents the contribution of ship's hull and ESD to the total resistance. The circular duct has opposite effect compared to the other two. In this case, the hull resistance is reduced, while additional drag is created by the duct. In the other two cases, the duct has a beneficial effect on resistance (i.e. thrust). Overall, the difference between the reference case and the other two is negligible, with a reduction of over 1% observed in the case of the duct with half-rings.

Table 26: Effect of the three candidate pre-swirl ESDs on the resistance of the ship.

	Hull Res. [kN]	**Duct Res. [kN]**	**Ship Res. [kN]**	**Difference [%]**
Reference	-	-	995.97	-
Circular	939.71	55.03	994.74	-0.12%
Duct with fins	1037.67	-37.01	1000.66	0.47%
Duct with half-rings	1005.27	-22.15	983.12	-1.29%

Post-swirl ESDs

The last ESD examined here is a post-swirl device designed to reduce the vortex induced drag created by the rotation of propeller cap. As indicated by the results presented in Table 25 and repeated here in Table 27 only for studied case, similar results are obtained with and without the ESD.

Table 27: Comparison of results between the reference case and the case with the Vortex Cap Fins.

	Ship Res. [kN]	Prop. Torque [kNm]	Prop. RPM	Prop. Power (mean) [kW]	ESD Gain/Loss [%]
Reference	995.97	842.03	83.9	7397.17	-
Hub Vortex Fins	992.22	836.74	84.3	7390.78	0.10%

The hydrodynamic coefficients of the propeller for the two cases are present in Table 28, for draught T_{sc}=14.45m and V_s=13.5kt.

Table 28: Propeller hydrodynamic coefficient for the reference case without ESD and for the case with Vortex Cap Fins.

	w	J	K_t	K_q	η
Reference	0.274	0.519	0.213	0.0259	0.678
Hub Vortex Fins	0.274	0.516	0.210	0.0255	0.677

The wake fraction w is computed as 0.274 based on towing resistance simulations for the corresponding draft and speed (see Figure 61). The rest of the hydrodynamic coefficients are calculated as follows:

Propeller advancing ratio:

$$J = \frac{(1-w)V_s}{nD_p} \tag{4.25}$$

Propeller thrust coefficient:

$$K_t = \frac{T}{\rho n^2 D_p^4} \tag{4.26}$$

Propeller torque coefficient:

$$K_q = \frac{Q}{\rho n^2 D_p^5} \tag{4.27}$$

Propeller efficiency:

$$\eta = \frac{JK_t}{2\pi K_q} \tag{4.28}$$

The thrust and torque coefficients are slightly reduced, leading to a corresponding increase in propeller efficiency.

Figure 65 and Figure 66 present flow visualizations for the reference case and the case with the Vortex Cap Fins. In the first figure, the axial velocity component of the flow is shown. The ESD efficiently decelerates the flow behind the cap. The highly accelerated flow is spread to larger region behind the hull. This is further pronounced in Figure 66, where the axial component of vorticity is plotted in a disk behind propeller. The strength of the vortex on the cap is significantly reduced. However, additional vortices are generated by the tips of the ESD.

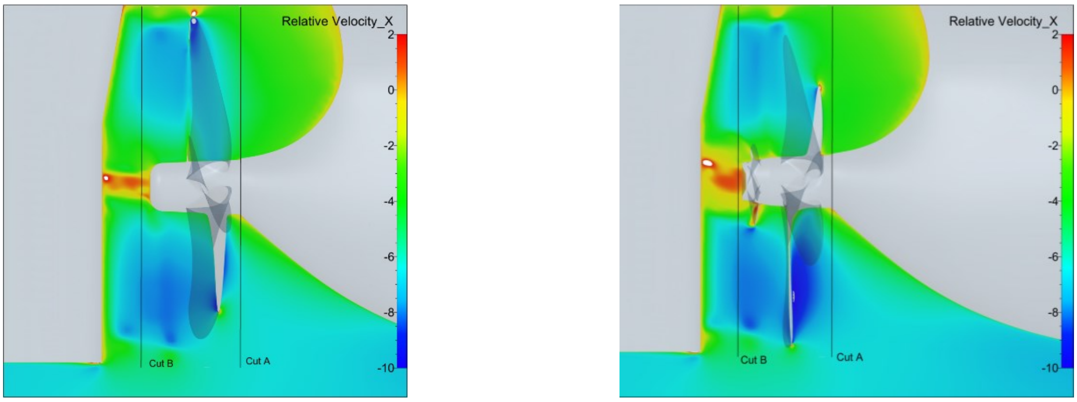

(a) Reference case without ESDs. (b) Propeller equipped with Hub Vortex Fins.

Figure 65: X-velocity contour for configurations (a) and (b).

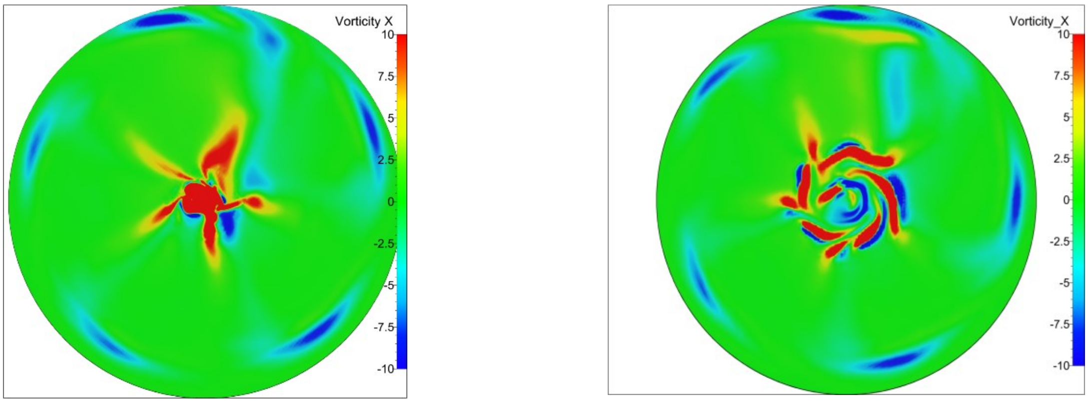

(a) Reference case without ESDs. (b) Propeller equipped with Hub Vortex Fins.

Figure 66: Vorticity contour at Cut B for configurations (a) and (b).

4.4.3 Conclusions

The present study examined the working principles of four different ESD devices, three pre-swirl and one post-swirl. Although, the examined vessel has a high block coefficient vessel ($c_b = 0.84$), preliminary evaluations that no separation bubbles were present at the stern of the ship and a relative high wake fraction was obtained at the propeller plane. The gains from the pre-swirl devices were approximately 2% in all cases, while no benefits were observed from installing the Hub Vortex Fins at the shaft of the propeller. Due to limited resources and the large number of candidate ESDs, Medium grid resolution was used for the simulations. In order to a have conclusive results regarding the efficiency of ESDs, further evaluations are needed with finer grid resolution.

Flow visualizations revealed that, although similar gains were predicted by all pre-swirl devices, their working principles differed. The circular duct accelerates the flow towards the propeller plane, but its effect on the upper side of the propeller plane is minimal. Additionally, the velocity deficit due to the thick aerofoil section negatively impacts propeller efficiency. The duct equipped with pre-swirl stators efficiently redirects the flow towards the propeller, and the small size of the duct does not affect the efficiency of the propeller. Lastly, the duct with half-rings successfully accelerates the flow at the upper part of the propeller without affecting the flow at the lower side.

The post-swirl device selected for this study did not provide any benefits to the propeller efficiency. Although the strength of the hub vortex was significantly reduced by the fins, the overall efficiency of the propeller is slightly decreased. This is most likely due to resistance caused by the fins in the rotation of the propeller.

The study revealed that, although ESD retrofitting of full-block vessels has been shown to significantly increase the efficiency of such vessels, its application to the specific case study yielded minimal benefits. The particular vessel is a modern one, built in 2019, and the viscous effects on the stern of the hull are especially constrained. For this reason, the gains obtained from ESD retrofitting depend primarily on the stern flow, with the type of ESD installed having a secondary effect. Finally, it is important to note that full-scale simulations using CFD are the most appropriate way to examine the viscous effects on the stern of the hull and to avoid any scaling uncertainties that may arise from experimental modelling.

5 Hydrodynamic design optimization of *RoRo* vessel

5.1 Introduction

The growing urgency to reduce greenhouse gas (GHG) emissions in the maritime industry has led to a significant focus on retrofitting existing vessels with optimized components to improve fuel efficiency. Maritime transport remains one of the key contributors to global carbon emissions, making efficiency improvements crucial to achieving environmental sustainability. By targeting vessel resistance reduction through hydrodynamic optimization, this study aims to make meaningful contributions toward global decarbonisation goals.

This report presents a case study under the Horizon Europe Programme (Grant No. 101096068), focusing on bow optimization for the RoRo cargo ship EUROCARGO ROMA (Hyundai Class). The objective of this study is to minimize total resistance in calm water conditions at a cruising speed of 18 knots. By leveraging advanced numerical methods, shape parameterization, and data-driven optimization frameworks, the study seeks to enhance the ship's performance while maintaining operational constraints.

Through a combination of hydrodynamic solvers, parameterized bow modifications, and machine learning-based optimization, we aim to improve vessel efficiency and contribute to the 55% GHG reduction target by 2030. The methodology presented in this report not only serves as a foundation for bow retrofitting in similar vessels but also establishes a structured approach to leveraging high-performance computing for naval architecture advancements [16].

5.2 Optimization Problem Formulation

5.2.1 Objective Function

The primary objective of this study is to minimize the total resistance of the vessel at a cruise speed of 18 knots in calm waters. This involves reducing wave-making and frictional resistance and optimizing the hull form while adhering to geometrical constraints. The optimization process was designed to ensure feasible modifications that would not compromise the vessel's stability or structural integrity.

Resistance minimization in this context directly translates to improvements in fuel efficiency, lowering fuel consumption and associated emissions. The optimization problem is constrained by several geometric and practical limitations, ensuring that the new design remains within the feasible range of shipyard modifications.

5.2.2 Bow Parameterization

The bow shape was modified using a Free-Form Deformation (FFD) [36] approach, where the geometry was adjusted via an 11×4×4 lattice of control points (Figure 67). Out of these, 8 control points were actively used to introduce shape variations, leading to a set of 20 design variables.

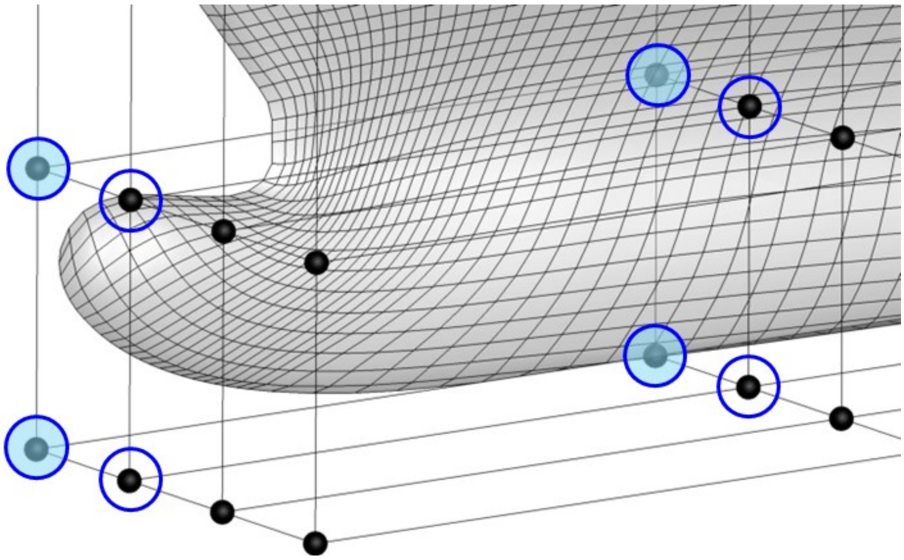

Figure 67: Bow parameterization via FFD.

A Parametric Model Embedding (PME) [37] technique was used to reduce the dimensionality of the design space by 75%, using a number of reduced design variables equal to 5, ensuring computational efficiency while preserving significant shape variations. Reducing the number of design variables helps accelerate the optimization process, reducing computational costs while maintaining accuracy. Figure 68 shows the convergence of the method varying the sample size and the sampling method. Figure 69 shows the convergence of the geometric variance resolved by PME representations, varying the number of reduced variables. The figure also shows the distribution of geometry reconstruction error with a number of reduced variables equal to 5. Finally, Figure 70 shows the basis embedding the original design parameterization, allowing to understand what of the original design variables participate most to the geometric variance.

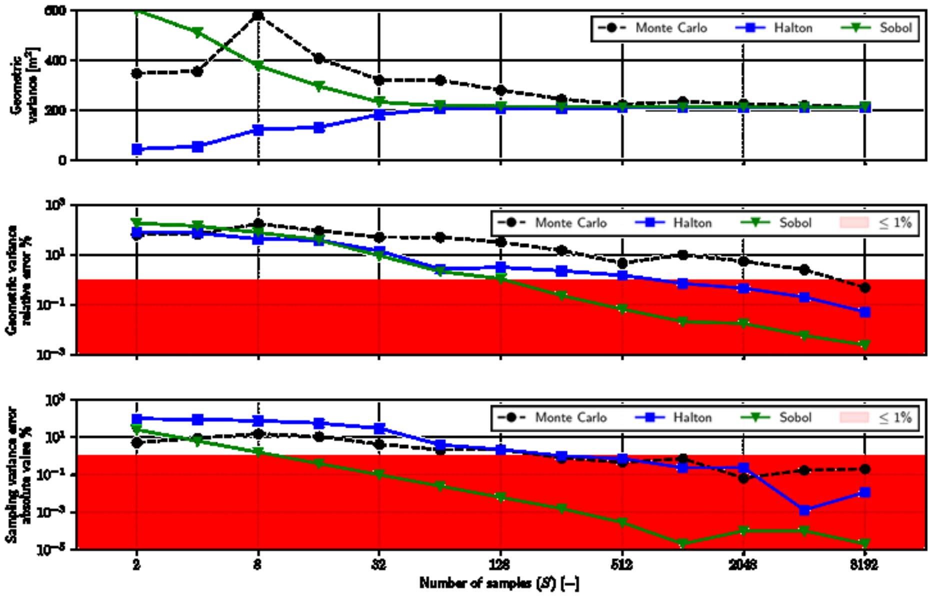

Figure 68: PME convergence varying the sample size and the sampling method.

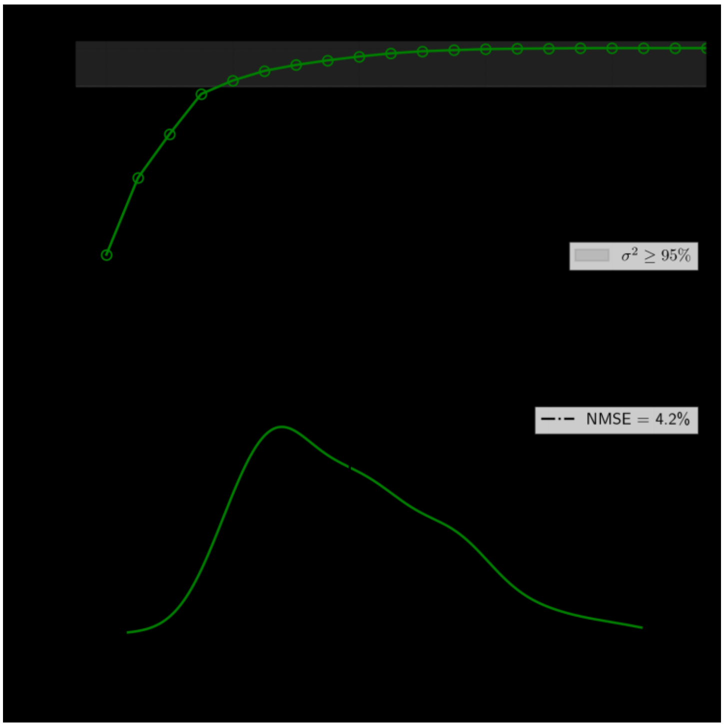

Figure 69: Convergence of the geometric variance resolved by PME representations, varying the number of reduced variables (top) and distribution of geometry reconstruction error with N=5 (bottom).

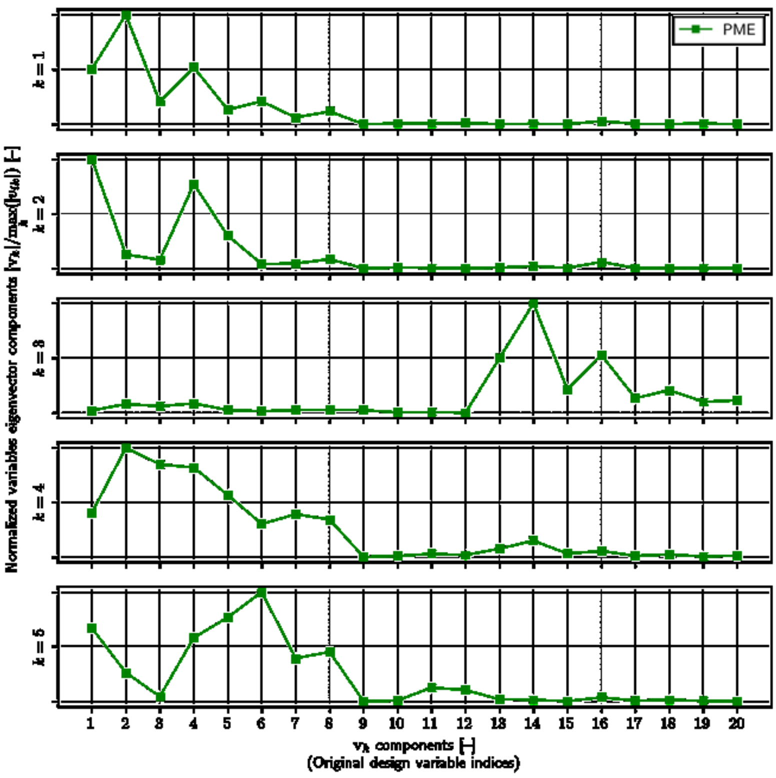

Figure 70: Embedding of original design variables (modes) provided by PME

5.2.3 Optimization Methodology

A multi-fidelity surrogate-based [38] optimization method was employed, leveraging stochastic radial basis functions. This method combined high-fidelity (2-DoF simulations) and low-fidelity (even keel simulations) models to optimize the bow shape iteratively. Active learning [39] techniques with dynamic lower confidence bounding [40] were integrated to accelerate convergence, and deterministic particle swarm optimization [41] was utilized to refine the final design.

The surrogate modelling approach enabled efficient design space exploration, balancing accuracy and computational efficiency by dynamically allocating computational resources to the most promising design candidates.

5.3 Hydrodynamic Solvers and Computational Setup

To evaluate ship performance, two hydrodynamic solvers were employed. The first was a linear potential flow analysis using the Wave Resistance Program (WARP) [42], developed at CNR-INM, which provides an efficient estimation of wave resistance. The second was a Reynolds-Averaged Navier-Stokes (RANS) solver implemented in OpenFOAM v2206, used for detailed simulations of the vessel's hydrodynamic behavior in full-scale conditions [43]. Potential flow solvers provide rapid estimations of wave resistance, making them suitable for early-stage design evaluations. However, RANS solvers offer a more detailed representation of viscous effects and turbulence, making them essential for high-fidelity validation.

Potential flow simulations using the WARP solver employed Dawson linearization and pressure integration methods to estimate wave resistance. The computational grid for these simulations consisted of 200×40 nodes for the hull surface and 112×45 nodes for the free surface, totalling approximately 13,000 nodes, see Figure 71. Validation of the solver against extreme draft displacement data showed a minor error of -0.5%, confirming its accuracy. Here, two fidelity levels are used to speed up the optimization process. The lowest fidelity level uses even keel (0 DoF) computations, whereas the highest fidelity level uses dynamic computations with 2 DoF (sinkage and trim are dynamically identified). The computational cost ratio of 0 DoF over 2 DoF is about 1/10.

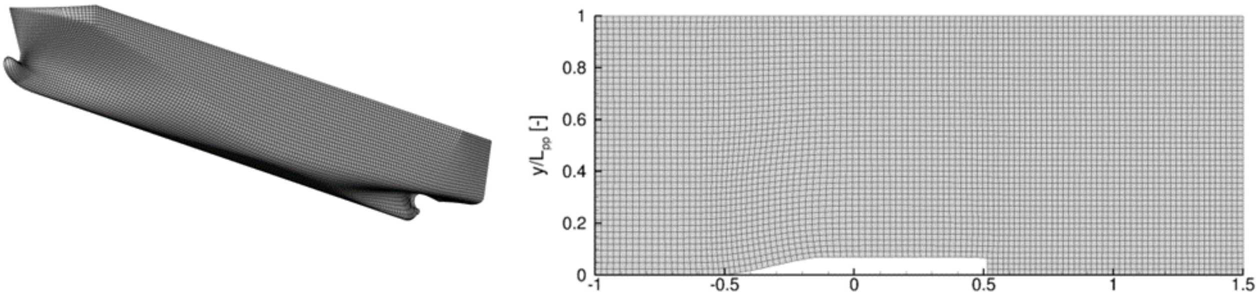

Figure 71: Panel grid used by WARP.

RANS simulations were conducted using the open-source finite-volume CFD library OpenFOAM, a software widely used in the literature [44],[45]. The simulations were conducted taking into account the presence of the free surface, which is a critical aspect of the study. As the objective of the optimization is the bulbous bow, it is essential to accurately capture its interaction with the free surface and the effects this has on wave generation and overall hydrodynamic performance. The inclusion of the free surface ensures a realistic representation of the flow dynamics and validation of the optimisation results under real operating conditions. The incompressible multiphase solver based on *interFoam* pressure was used, which numerically solves the Navier-Stokes equation of the fluid, which is considered here as incompressible and laminar, using the finite volume technique.

Furthermore, the applied solver adopts the fluid volume interface (VOF) capture method to define the evolution of the completely nonlinear free surface. Moving on to turbulence modeling, the k-ω SST turbulence model is adopted, as it is widely recognized and extensively validated for such applications. Temporal discretization is handled using the Crank-Nicolson method, with an adaptive timestep chosen to maintain a maximum Courant number of 1. The RANS simulations were conducted under nominal draft conditions. Given that trim and sinkage movements are limited, as identified through the potential model, the hull was assumed to operate at even keel throughout. The grid was constructed using a combination of the *blockMesh*, *refineMesh*, and *snappyHexMesh* utilities available in the OpenFOAM library. The *blockMesh* utility generates the background grid, which extends 1.5L in front of the bow and 3L behind the transom along the x-axis; 3L along the y-axis; and 5L in the z-direction, extending downward from the slope and about 0.7L upward, where L corresponds to the length between perpendiculars (Lpp = 190m). A refinement is applied along the z-axis to more accurately capture the free surface. Subsequently, the grid is further refined in the x-y plane through six iterative *topoSet* and *refineMesh* loops, creating additional refinement blocks near the hull. The hull-background intersection is resolved using the *snappyHexMesh* utility, which removes the cells containing the body and reconfigures the grid around it. The final grid consists of 1.5 million cells and is displayed in Figure 72.

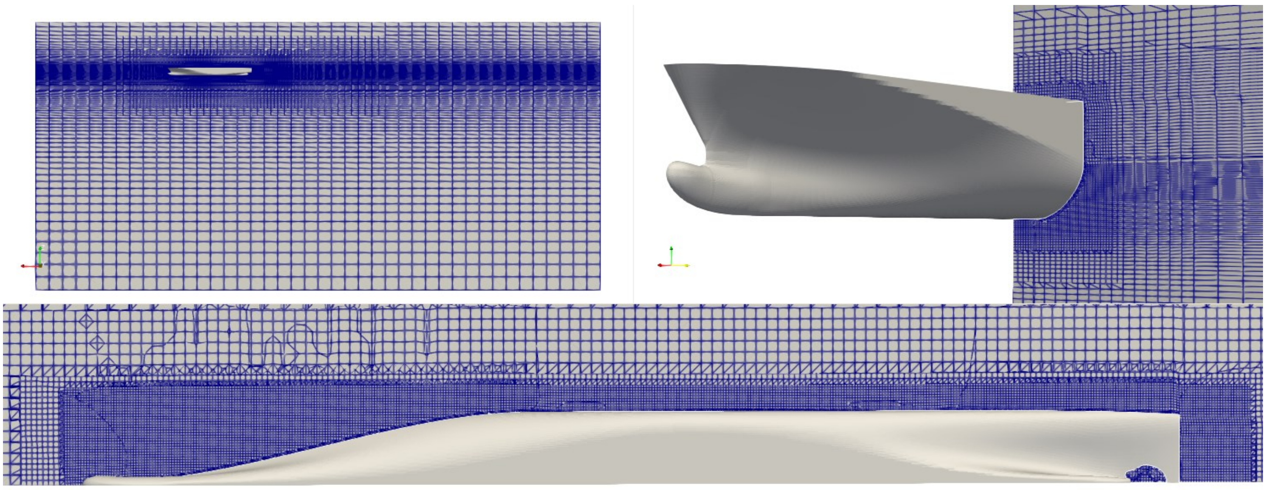

Figure 72: RANS computational grid

5.4 Optimization Results

The optimization process successfully converged after 95 function evaluations, with 30 high-fidelity and 413 low-fidelity samples. The optimized bow design achieved a 1.7% reduction in total resistance compared to the baseline hull. The optimization process convergence is depicted in Figure 73, whereas Figure 74 presents the final solution achieved, showing a comparison with the original geometry. Figure 75 shows a performance comparison of optimized versus original bow designs over a speed range.

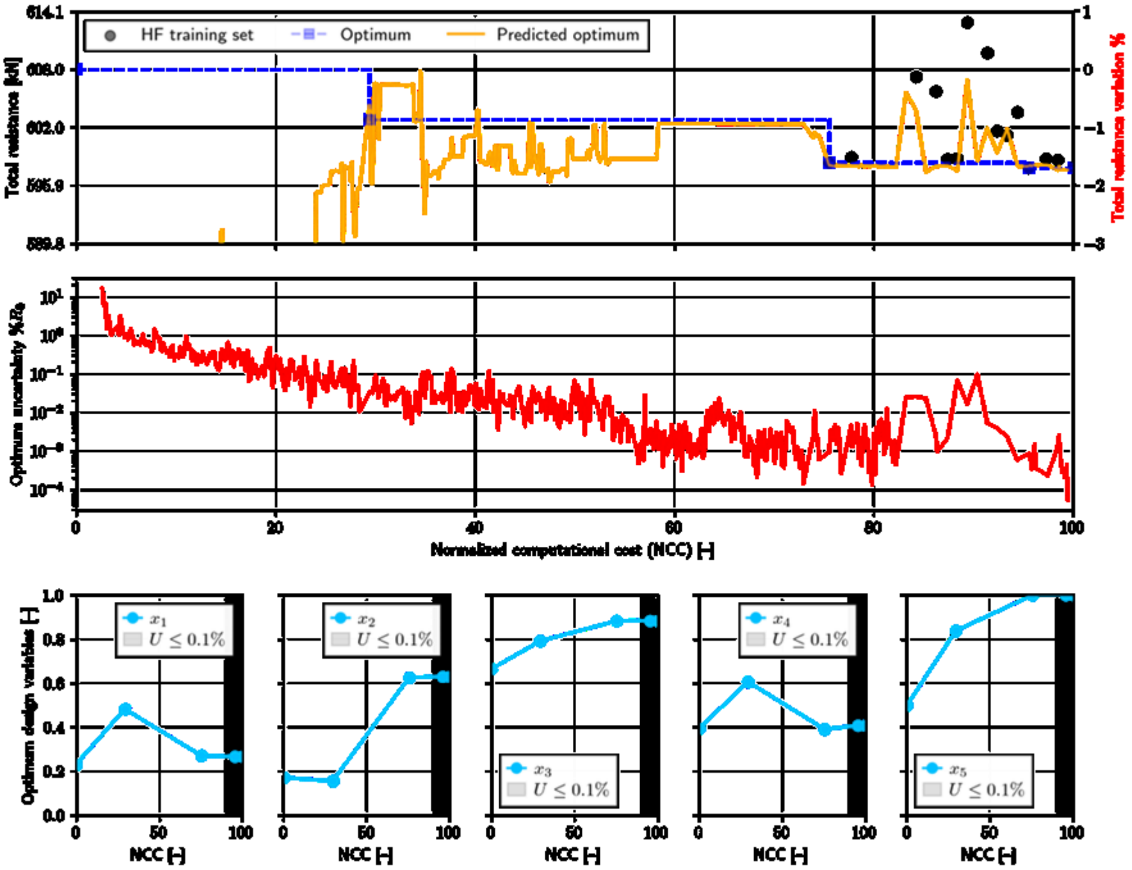

Figure 73: Optimization process convergence.

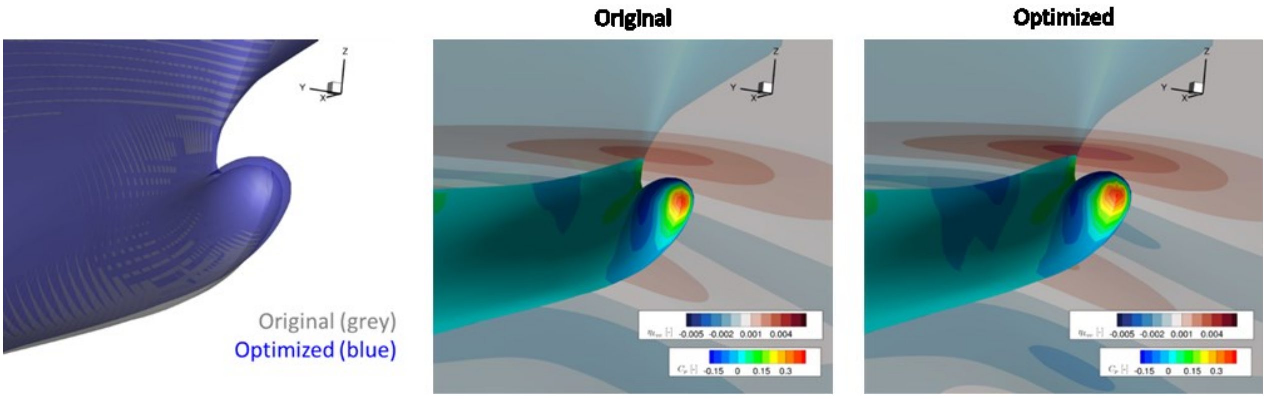

Figure 74: Optimization solution (comparison with the original design: geometry, pressure and wave elevation).

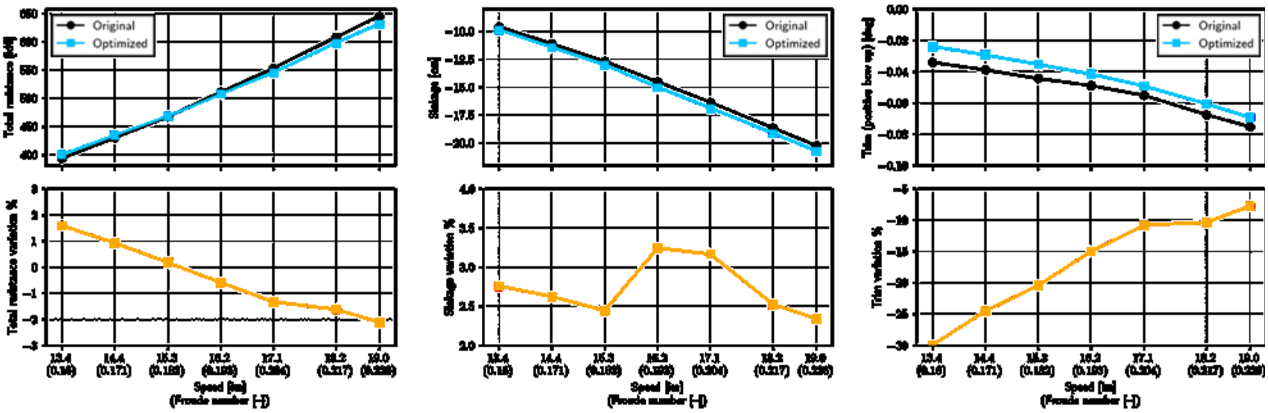

Figure 75: Performance comparison of optimized versus original bow designs (resistance, sinkage, and trim) over a speed range.

5.5 RANS Verification of Optimal Solution

The optimization process was verified through RANS simulations to confirm the reliability of the proposed design improvements. These simulations were performed at full scale, which presents considerable challenges due to the inherent complexity and high computational requirements. However, full-scale modelling is crucial to ensure that the results accurately reflect real performance, overcoming the limitations of scaled or simplified approaches that may miss critical flow characteristics. The use of full-scale RANS simulations not only provides a more detailed and realistic representation of the flow field but also serves as a robust validation of the optimization carried out using the potential model. This two-step approach combines the efficiency of potential-flow optimization with the high-fidelity accuracy of RANS simulations, delivering both computational efficiency and reliable performance verification.

First, the case of the original hull at the nominal speed of 18.2 kn was analyzed. The simulation was carried out for a duration of 500 seconds, during which an acceptable convergence of the key variables was achieved. This period was sufficient to capture the steady-state behavior of the flow and wave patterns around the hull. The computational cost for this analysis amounted to approximately 850 CPUh, reflecting the complexity of the model and the extensive computational resources required for the simulation. During the simulation, the free surface elevation was monitored closely to ensure that the interaction between the hull and the waves was accurately represented. Figure 76 depicts the pressure distribution along the longitudinal plane of the hull and the resulting free surface height, providing insight into the wave patterns generated by the hull at the analyzed speed. Additionally, Figure 77 offers a detailed view of the pressure distribution over the bulb area, which represents the primary focus of the optimization study.

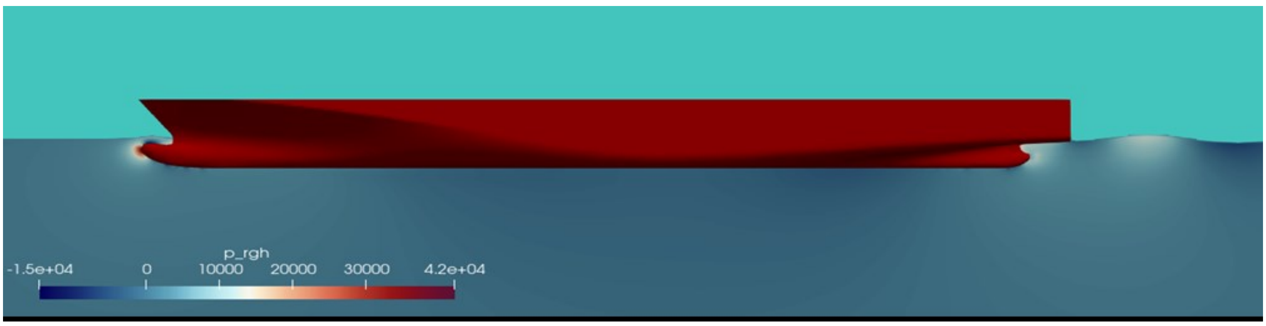

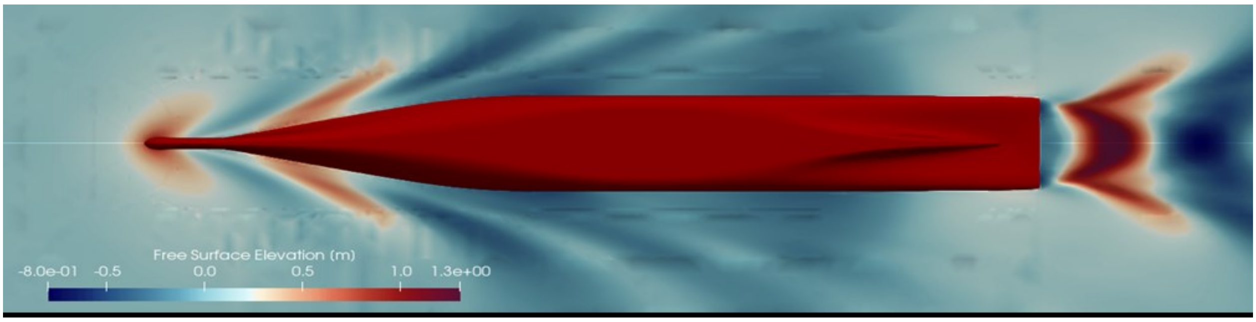

Figure 76: Pressure distribution and free surface elevation of original hull at nominal speed

Under the tested conditions, the total resistance experienced by the hull is 571kN, showing a discrepancy of about 6.5% compared to the predictions made with the potential model. This difference was expected and can be attributed to the more complex physical effects captured in the RANS simulations, which are not accounted for in the potential model.

RANS simulation at the nominal speed was also performed on the optimized hull, and the results were compared to those of the original hull. As illustrated in Figure 78, the region of positive pressure on the bulb is larger for the optimized hull, and the modifications to the bulb geometry result in slightly higher waves around it. Notably, these differences align closely with those observed in the potential flow simulations. Furthermore, in terms of total resistance, the optimized hull demonstrates a reduction of approximately 1.75%, which is in perfect agreement with the results from the potential flow model. Therefore, the RANS verification effectively confirms the findings of the potential flow optimization at nominal speed.

Finally, a resistance curve was derived at different speeds, as shown in Figure 79. The trend obtained is comparable to that derived from the potential model, although there is a more pronounced increase in the total resistance of the optimized hull at low speeds, and a less noticeable improvement at speeds higher than the nominal.

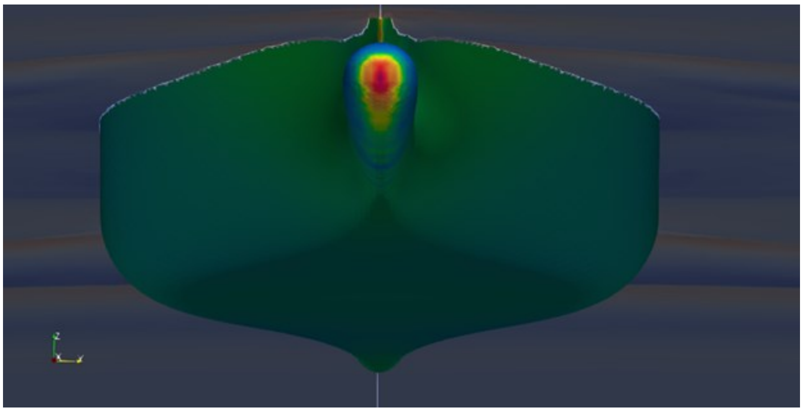

Figure 77: detail of pressure distribution on original hull at nominal speed.

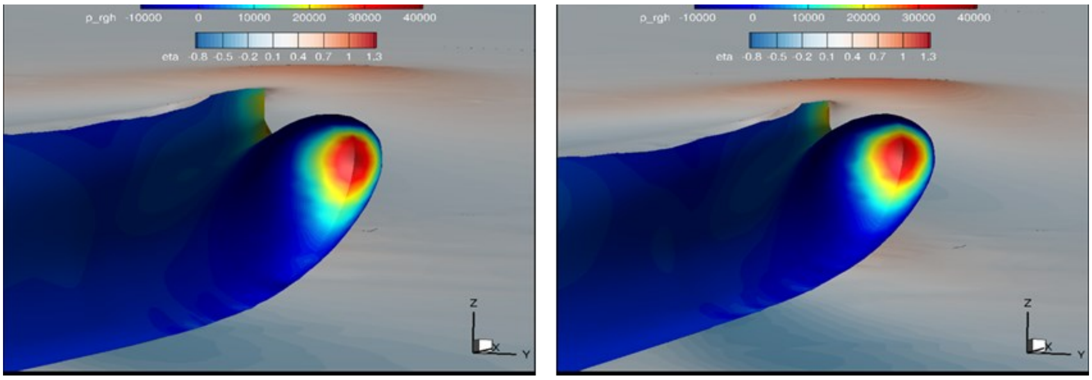

Figure 78: pressure distribution and free surface elevation on original and optimized hull at nominal speed.

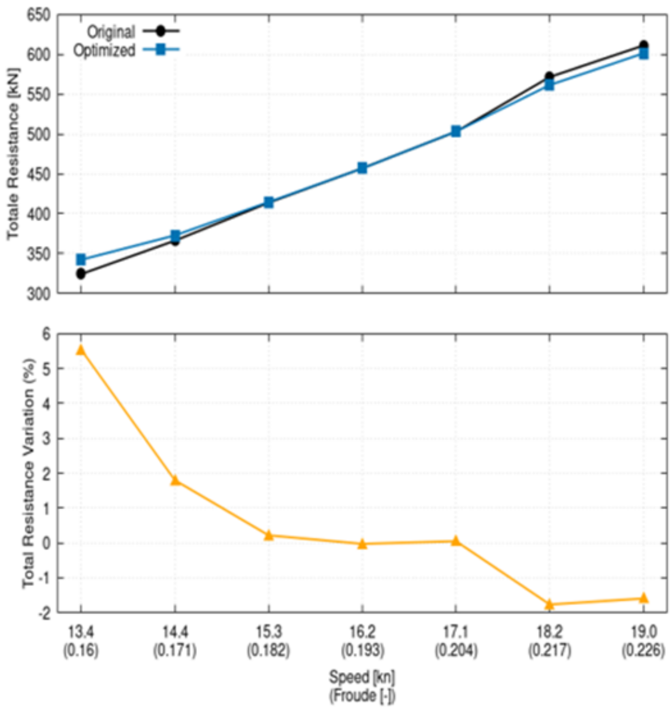

Figure 79: Total resistance curves and total resistance variation.

5.6 Conclusions

This study demonstrated the effectiveness of bow retrofitting for resistance reduction in RoRo cargo ships. The optimized bow design achieved an approximately 2% reduction in total resistance, with RANS validation confirming the performance gains. The multi-fidelity optimization framework significantly reduced computational costs, enabling rapid design iterations without relying solely on high-fidelity simulations.

These findings will be presented at the IMAM 2025 Congress in Crete, Greece. Future work includes further refinement of machine learning-based optimization techniques and experimental validation through towing tank tests to confirm real-world performance improvements.

6 Conclusions

The present study explores different retrofitting solutions to improve a ship's hydrodynamic design. To this end, two different types of vessels have been selected to apply the different retrofitting solutions. A bulk carrier and Ro-Ro vessel have been examined, as they represent two major categories with distinct characteristics - low speed cargo ships with high block coefficient and slender, faster vessels respectively. All studies have been performed considering the operational profiles of the vessels, such as speed range and loading conditions, to ensure realistic approximation.

Starting with the bulk carrier vessel, three retrofitting solutions along with one operational optimization have been considered to improve its hydrodynamic performance. Firstly, the design of the propeller has been taken into consideration by examining different pitch and camber distributions as well as a modified rake at the propeller tip. A multi-fidelity framework has been exploited for the evaluation of alternative designs. This combines a high-fidelity finite volume CFD solver and a Vortex Lattice Method (VLM) enabling fast evaluation without compromising the accuracy of the results. The shape optimization process of the propeller revealed a small increase in propeller efficiency of approximately 1%. Additionally, the effect of roughness was investigated with respect to the cavitation properties of the propeller. Although, in some cases the roughened surface of the propeller promotes cavitation, in a specific combination of operating conditions and fouling level, cavitation does not appear to be critical for propeller performance.

The next solution examines improving the hydrodynamic design of the vessel by modifying the bulbous bow of the bulk carrier vessel. The freeform deformation technique has been utilized to modify the geometry of the pre-existing bulb. More specifically, the bow was modified by changing the length, height and the width of the bulb. The optimization study considered 200 variant geometries. The FlowTech software has been used to evaluate the designs. The results showed that a modification from the current design would not lead to any improvement in the hydrodynamic performance of the vessel. This may be attributed to the fact that the operating conditions considered are close to the design conditions and thus the potential for performance improvement through shape optimization is limited.

Energy Saving Devices (ESDs) are one of the most prominent solutions to improve ship's hydrodynamic performance. In the present report, parametric models of pre- and post-swirl devices have been created that allow for the evaluation of different ESD designs. Particularly, four different ESD devices have been selected and evaluated. CFD self-propulsion studies have been carried out using accurate propeller description. The results indicate that improvement of hydrodynamic performance of the vessel is feasible. More than one design showed a gain in performance of 2%. Greater improvements are possible by conducting dedicated optimization studies for each design separately.

Furthermore, apart from retrofitting solutions, a trim optimization study has been conducted by taking into account the operational profile of the bulk carrier vessel. The goal of this study is to explore the most suitable loading profiles of the vessel that will not have an adverse effect on the hydrodynamic performance of the vessel. The study revealed significant fluctuations in the resistance depending on the loading conditions of the vessel.

The report concludes with a shape optimization study of the Ro-Ro vessel. As in the case of the bulk carrier vessel, a shape optimization of the bow has been carried out. The free form deformation technique has been utilized to modify the geometry of the bow. In order to speed up the calculations, dimensionality reduction has been performed and furthermore a multi-fidelity framework has been employed to evaluate the different scenarios. The results showed that a 2% reduction of resistance can be achieved by adopting a different bow geometry.

All in all, the report summarizes the efforts to improve the hydrodynamic design of the two selected case study vessels. A range of retrofitting options has been explored, however small to minimal gains were predicted in all cases. It is evident that in order to achieve a significant reduction of GHG emissions a combination of technologies is necessary. The results reported in the present study such as power and resistance curves, possible gains from the various solutions, will be exported to WP1 and integrated into the DSS.

References

[1] Kang, J.W.; Kim, C.M., Kim,H.U. and Shin, I.R. Study on the propulsion performance of varying rake distribution at the propeller tip. *J. Mar. Sci. Eng.* 2019, *7*, 386.

[2] Carlton, J. *Marine Propellers and Propulsion*; Butterworth-Heinemann: Oxford, UK; Elsevier: Oxford, UK, 2007.

[3] Belibassakis, K. and Filippas, E. Ship propulsion in waves by actively controlled flapping foils. Appl. Ocean. Res. Vol. 15 2015

[4] Ntouras, D.; Papadakis, G. A coupled artificial compressibility method for free surface flows. J. Mar. Sci. Eng. 2020, 8, 590.

[5] Chorin, A.J. A numerical method for solving incompressible viscous flow problems.*Journal of computational physics* vol. 35(2), 1997, pp. 118-125.

[6] Temam, R. "Une méthode d'approximation de la solution des équations de Navier-Stokes. Bulletin de la Société Mathématique de France, 1968. pp. 115-152

[7] Roe, Philip L. Approximate Riemann solvers, parameter vectors, and difference schemes. Journal of computational physics 43.2.1981.pp. 357-372.

[8] Menter, F.R. Two-equation eddy-viscosity turbulence models for engineering applications. *AIAA J.* 1994, pp. 1598–1605.

[9] Boswell, R. Design, cavitation performance, and open-water performance of a series of research skewed propellers. *NSRDC Report 3339.*

[10] Kinnas, S.A.; Cha, K.; Kim, S. Comprehensive design method for open or ducted propellers for underwater vehicles. In Proceedings of the SNAME Maritime Convention, Providence, RI, USA, 27–29 October 2021.

[11] Kunz, R. F., Boger, D. A., Stinebring, D. R., Chyczewski, T. S., Lindau, J. W., Gibeling, H. J. and Govindan, T. A preconditioned Navier–Stokes method for two-phase flows with application to cavitation prediction. Computers & Fluids, vol. 29(8), 2000, 849-875.

[12] Esch, T. and Menter, F. . Elements of industrial heat transfer predictions. In 16th Brazilian Congress of Mechanical Engineering (COBEM) Uberlandia, Canada, 2001

[13] Schultz, M. P. and Flack, K. A. The rough-wall turbulent boundary layer from the hydraulically smooth to the fully rough regime. Journal of fluid mechanics,2007, vol. 580, 381-405.

[14] Kellett, P., Mizzi, K., Demirel, Y. K., and Turan, O. Investigating the roughness effect of biofouling on propeller performance. In International Conference on Shipping in Changing Climates, November 2015

[15] Renzsch, H., Meyer, J. and Graf, K., Investigation of modern sailing yachts using a new free-surface RANS-code. Proceedings International Conference on Innovation in High Performance Sailing Yachts, 4th Edition, Lorient, FR, 2017.

[16] Serani, A., Scholcz, T. P. and Vanzi, V, A scoping review on simulation-based design optimization in marine engineering: trends, best practices, and gaps. Archives of Computational Methods in Engineering, p. 1-29, 2024

[17] International Towing Tank Conference, Committee for Performance and Propulsion, 1978 ITTC Performance Prediction Method, ITTC Recommended Procedures 7.5-02 03-01.4, 1999.

[18] Carlton, J.S., Marine propellers and propulsion, 2nd Edition, Butterworth-Heinemann, 2009

[19] Spinelli, F., Mancini, S., Vitiello, L., Bilandi, R.N., and De Carlini, M., Shipping Decarbonization: An Overview of the Different Stern Hydrodynamic Energy Saving Devices. Journal of Marine Science and Engineering, vol 10(5), 574, 2022

[20] Thies, F., Renzsch, H., Hull Form Variations for Improved Sailing Balance of Wind-Assisted Propelled Ships, 16th Symposium on High-Performance Marine Vehicles – Technologies for the Ship of the Future" (HIPER), June 2024

[21] Visonneau, M., Deng, G., Queutey, P., and Guilmineau, E. High-Fidelity Computational Analysis of an Energy-Saving Device at Model Scale. Hull Performance & Insight Conference (HullPIC), Turin, Italy, April 2016

[22] Zondervan, G.J. and Holtrop, J. On the Design and Analysis of Pre-Swirl Stators for Single and Twin-Screw Ships, Second International Symposium on Marine Propulsors, Hamburg, Germany, June 2011

[23] Mewis, F. A Novel Power-Saving Device for Full-Form Vessels. First International Symposium on Marine Propulsors, Norway, June 2009

[24] Andersson, J., et. al., Ship-scale CFD benchmark study of a pre-swirl duct on KVLCC2. Applied Ocean Research, vol. 123, 2022

[25] Schneekluth, H., Wake equalizing duct. The Naval Architect 103, pp. 147–150, 1986

[26] Çelik, F., A numerical study for effectiveness of a wake equalizing duct. Ocean Engineering, vol. 34(16), 2007

[27] Kawamura, T., Ouchi, K., & Nojiri, T., Model and full scale CFD analysis of propeller boss cap fins (PBCF), Journal of marine science and technology, 17, 469-480, 2012.

[28] Yu, L., Greve, M., Druckenbrod, M., & Abdel-Maksoud, M., Numerical analysis of ducted propeller performance under open water test condition, Journal of marine science and technology, 18, 381-394, 2013.

[29] Menter, F. R., Kuntz, M., and Langtry, R., Ten Years of Industrial Experience with the SST Turbulence Model, Turbulence, Heat and Mass Transfer 4, 2003, pp. 625 - 632.

[30] Hirt, C.W., Nichols, B.D, Volume of fluid (VOF) method for the dynamics of free boundaries, Journal of Computational Physics, vol. 39(1), 1981, pp. 201-225.

[31] Basara, B., Bounded convection schemes for unstructured grids. 15th AIAA Computational Fluid Dynamics Conference, June 2001

[32] Wackers, J., et. al., Free-Surface Viscous Flow Solution Methods for Ship Hydrodynamics. Archives of Computational Methods in Engineering, vol. 18, pp. 1-41.

[33] ITTC, Practical Guidelines for Ship Self-Propulsion CFD, 2014

[34] Celik, I., Ghia, U., Roache, P.J., Freitas, C., Coloman, H and Raad, P., Procedure of Estimation and Reporting of Uncertainty Due to Discretization in CFD Applications. Journal of Fluids Engineering, vol.130(1), 2008

[35] IMO, MEPC.1/Circ.850/Rev.2, 2017

[36] Sederberg, T. W. and Parry, S. R, Free-form deformation of solid geometric models. In Proceedings of the 13th annual conference on Computer graphics and interactive techniques, pp. 151-160, 1986

[37] Serani, A. and Diez, M. Parametric model embedding, Computer Methods in Applied Mechanics and Engineering 404: 115776, 2024

[38] Pellegrini, R., Wackers, J., Broglia, R., Serani, A., Visonneau, M. and Diez, M., A multi-fidelity active learning method for global design optimization problems with noisy evaluations. Engineering with Computers, *39*(5), 3183-3206, 2023

[39] Wackers, J., Pellegrini, R., Serani, A., Visonneau, M. and Diez, M., Efficient initialization for multi-fidelity surrogate-based optimization. Journal of Ocean Engineering and Marine Energy, *9*(2), 291-307, 2023

[40] Serani, A., Pellegrini, R., Wackers, J., Jeanson, C. E., Queutey, P., Visonneau, M. and Diez, M., Adaptive multi-fidelity sampling for CFD-based optimisation via radial basis function metamodels. International Journal of Computational Fluid Dynamics, *33*(6-7), 237-255., 2019

[41] Serani, A., Leotardi, C., Iemma, U., Campana, E. F., Fasano, G. and Diez, M., Parameter selection in synchronous and asynchronous deterministic particle swarm optimization for ship hydrodynamics problems. Applied Soft Computing, *49*, 313-334, 2016

[42] Bassanini, P., Bulgarelli, U., Campana, E. F. and Lalli, F., The wave resistance problem in a boundary integral formualtion. Surv. Math. Ind., 4, 151-194., 1994

[43] Jasak, H . OpenFOAM: Open source CFD in research and industry. International journal of naval architecture and ocean engineering, 1(2), pp. 89-94., 2009

[44] Hurtado Bustos, D., Paredes and Alvarado, R. J., Numerical hull resistance calculation of a catamarán using OpenFOAM, Ship Science and Technology Vol. 11 No. 21. 2017

[45] Li, J., Bonfiglio, L. and Brizzolara, S. Verification and validation study of OpenFOAM on the generic prismatic planing hull form. In Proceedings of VIII International Conference on Computational Methods in Marine Engineering., 2019